Australian Government
Bureau of Meteorology

The Centre for Australian Weather and Climate Research
A partnership between CSIRO and the Bureau of Meteorology

CSIRO

CAWCR Research Letters

Issue 11, September 2014

P. A. Sandery, H. Richter, K. Tory, K. A. Day (editors)

www.cawcr.gov.au

ISSN: 1836-5949

Series: Research Letters (The Centre for Australian Weather and Climate Research); Issue 11.

This issue of CAWCR Research Letters is based on presentations from the *Science for Services* workshop titled “Fire Weather and Severe Convection” held at the Bureau of Meteorology at 700 Collins Street Docklands on the 15-16 August 2013. The organising committee consisted of Aurora Bell (chair), Jeff Kepert, Harald Richter, Beth Ebert and Stephen Lellyett

Copyright and Disclaimer

Contents

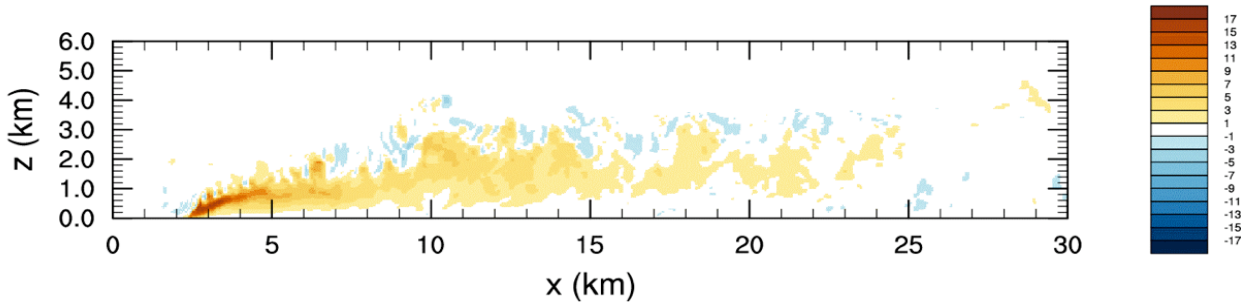

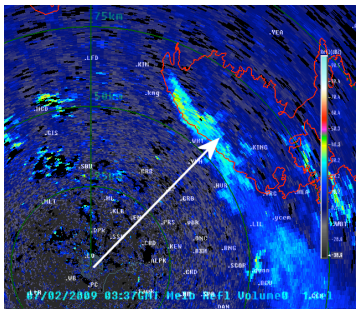

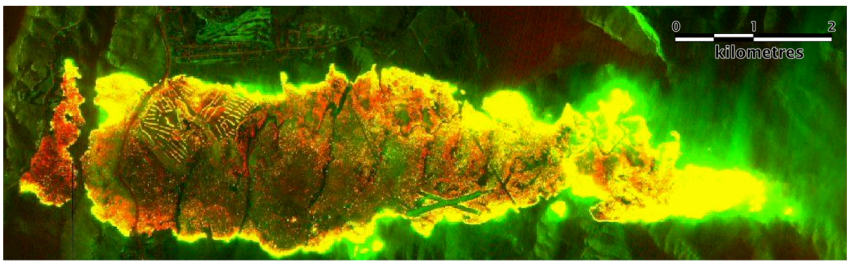

Editors: P.A. Sandery, H. Richter, K. Tory, K.A. Day
Enquiries: Dr Paul Sandery p.sandery@bom.gov.au
CAWCR Research Letters
The Centre for Australian Weather and Climate Research
Bureau of Meteorology
GPO Box 1298 Melbourne VICTORIA 3001

CAWCR Research Letters is an internal serial online publication aimed at communication of research carried out by CAWCR staff and their colleagues. It follows on from its predecessor *BMRC Research Letters.* Articles in *CAWCR Research Letters* are peer reviewed. For more information visit the *CAWCR* website.

Large-eddy simulations of bushfire plumes in the turbulent atmospheric boundary layer

William Thurston[A,B], Kevin J. Tory[A,B], Robert J. B. Fawcett[A,B], Jeffrey D. Kepert[A,B]
[A]The Centre for Australian Climate and Weather Research, Bureau of Meteorology, Melbourne, Victoria
[B]Bushfire Cooperative Research Centre, Melbourne, Victoria
W.Thurston@bom.gov.au

Introduction

Spot fires are a hazardous phenomenon which can lead to unpredictable fire behaviour and accelerated fire spread. Spot fires occur when firebrands are lofted into strong ambient winds and ignite new fires downwind. This increases the unpredictability and speed of fire spread because winds aloft are often in a different direction to and faster than the near-surface winds. There is evidence of long-range spotting in excess of 30 km during the Black Saturday bushfires, Cruz et al. (2012), highlighting the magnitude of the problem. A thorough knowledge of the potential for lofting from a fire is therefore desirable in order to accurately predict the rate of spread and coverage of bushfires.

The extent to which firebrands are lofted and transported away from a fire is largely determined by both the intensity of the fire convective column and the strength of the ambient winds. Previous work on the response of fire plumes to background winds has principally relied on theoretical or highly idealised numerical models. Here we use high resolution, three-dimensional numerical simulations, performed with the UK Met Office Large Eddy Model (LEM), to investigate the behaviour of bushfire plumes. We begin by simulating the dry, neutral atmospheric boundary layer for a range of wind speeds. Simulations are run to a quasi-steady state, ensuring that the flow displays realistic turbulent properties. Plumes are then produced by imposing a localised positive surface heat flux anomaly at the model surface. The sensitivity of the size, shape and intensity of the plume's updraft to the interaction between the plume and the turbulent atmospheric boundary layer is explored, with reference to the potential for spotting.

The Numerical Model

The simulations presented here are performed using Version 2.4 of the UK Met Office Large-Eddy Model (LEM), Gray et al., (2001). The LEM is a high-resolution non-hydrostatic atmospheric model, which solves a Boussinesq equation set on a three-dimensional Cartesian grid. The sub-grid stresses are parametrized using a stability-dependent version of the Smagorinsky scheme, described by Brown et al. (1994).

Previously the LEM has been used for more traditional high-resolution atmospheric applications, from dry boundary-layer turbulence to deep moist convection, although recently it has been used to study the behaviour of fire plumes. Devenish and Edwards (2009) used the LEM to perform simulations of the Buncefield oil depot fire in the UK, the largest fire in Europe since the Second World War. The model was able to successfully reproduce the observed height and multi-directional spread of the plume. Devenish et al. (2010) performed further validation by comparing the entrainment and radial spreading rates of buoyancy and vertical velocity in plumes simulated by the LEM to theoretical plume models.

Model Configuration

All simulations presented here are performed on a domain with horizontal dimensions of 768 by 384 grid points, with a uniform grid spacing of 50 m in both directions, resulting in a domain size of 38.4 km by 19.2 km. The domain has 256 grid points in the vertical, made from a stretched grid specified with a vertical grid spacing of 10 m near the surface, which increases smoothly to 50 m above a height of 3 km and leads to a model top at 10 km. The lateral boundary conditions of the model are doubly periodic and a no-slip condition is applied at the lower boundary, with a specified roughness length of 0.05 m. The domain size chosen is large enough for the periodic lateral boundary conditions not to affect the simulated plumes. At the model's upper boundary, a free-slip condition is applied in conjunction with a Newtonian damping layer in the top 2 km of the domain, to prevent the reflection of vertically propagating gravity waves. Our simulations are performed without any parameterizations for radiation, moisture or microphysics and the Coriolis force is also ignored.

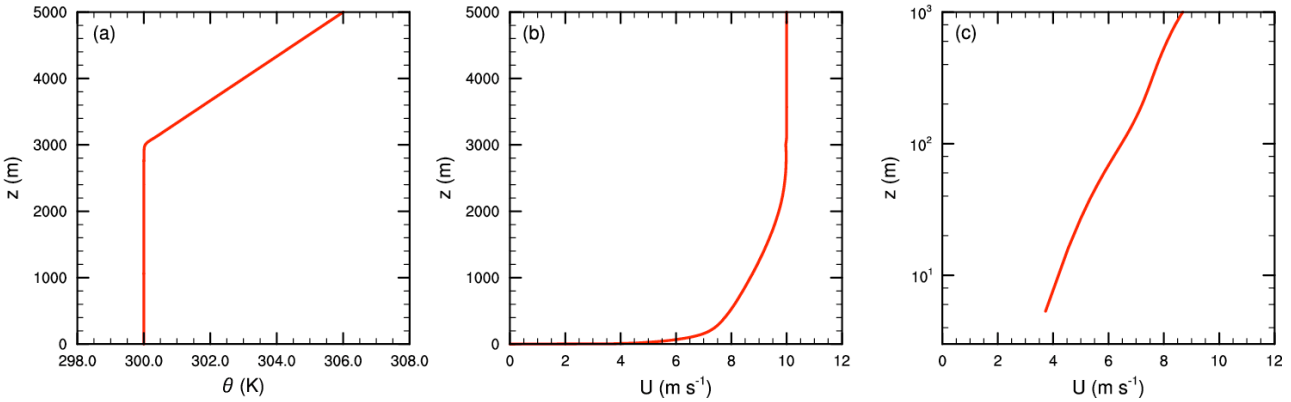

Figure 1 Domain-averaged profiles of the mean condition in the 10 m s^{-1} background-wind simulation at quasi-steady state. (a) Potential temperature θ (K); (b) velocity, m s^{-1}; and (c) velocity, m s^{-1}, plotted on a logarithmic height scale to emphasise the development of the log layer.

Boundary-layer Simulations

As described in the Introduction, before we attempt to model the behaviour of fire plumes we first establish a set of realistic "hot-start" conditions, in which bushfire plumes can be subsequently simulated. The model is initialised with horizontally homogeneous conditions. An initial potential temperature profile is specified, consisting of a constant 300-K mixed layer of 3 km depth, above which there is a constant lapse rate of 3 K km^{-1} up to the model top. This is designed to be representative of the vertical structure of the atmosphere on a typical Australian high fire risk day. The initial velocity is set to $u = u_{TOP}$ and $v =$ 0 m s^{-1} throughout the domain. Small perturbations with a maximum amplitude of ±0.1 K are added to the initial potential temperature field within the mixed layer, in order to initialise the development of turbulence, and then the model is integrated forward in time with a variable timestep, determined by the Courant–Friedrichs–Lewy condition. We perform six simulations in total, with six different values for the initial velocity, u_{TOP}, of 2.0, 5.0, 7.5, 10.0, 12.5 and 15.0 m s^{-1}. In each case the model is run until the boundary layer is fully spun up and has reached a steady state, determined by the domain-averaged turbulent kinetic energy (TKE).

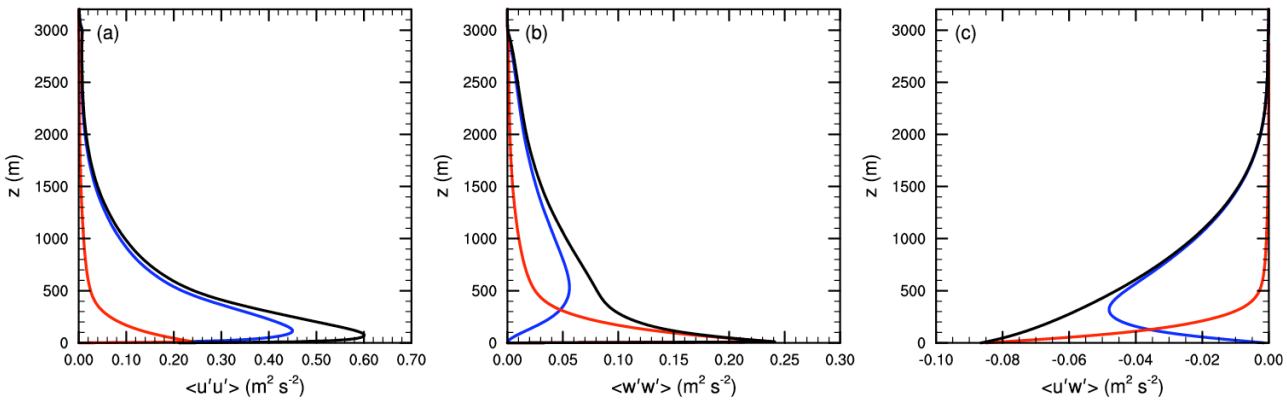

Figure 2. Domain-averaged profiles of the velocity variances and vertical momentum flux in the 10 m s^{-1} background-wind simulation at quasi-steady state. (a) $u'u'$, m^{-2} s^{-2}; (b) $w'w'$, m^{-2} s^{-2}; and (c) $u'w'$, m^{-2} s^{-2}. In each panel the resolved component is plotted in blue, the sub-grid component is plotted in red and the total is plotted in black.

The effect that spinning up the mixed-layer turbulence to a quasi-steady state has on the domain-averaged mean conditions is shown for the 10 m s^{-1} background wind case in Figure 1. The domain-average potential temperature profile (Figure 1a) has only been modified slightly from the specified initial conditions, with a small smoothing of the transition point at the top of the mixed layer where the constant potential temperature zone meets the constant potential-temperature gradient zone. The modification of the average velocity profile (Figure 1b) is much more marked. The velocity at the surface has reduced to zero and a log layer has developed above it, as highlighted by the profile replotted on a log-height y-axis (Figure 1c). In fact, the velocity at the surface reduces to zero

very early on in the simulation, but the log layer only develops once the resolved mixed-layer turbulence has spun up (not shown). The domain-averaged profiles of the velocity variances, $u'u'$ and $w'w'$, and the vertical flux of horizontal momentum, $u'w'$, are presented in Figure 2. The profiles of these quantities and their partitioning into resolved and sub-grid components are in good agreement with previous studies of the neutral, shear-driven boundary layer (e.g. Mason and Thomson, 1987; Andren et al., 1994) indicating that we have generated a realistic neutral, turbulent atmospheric boundary layer.

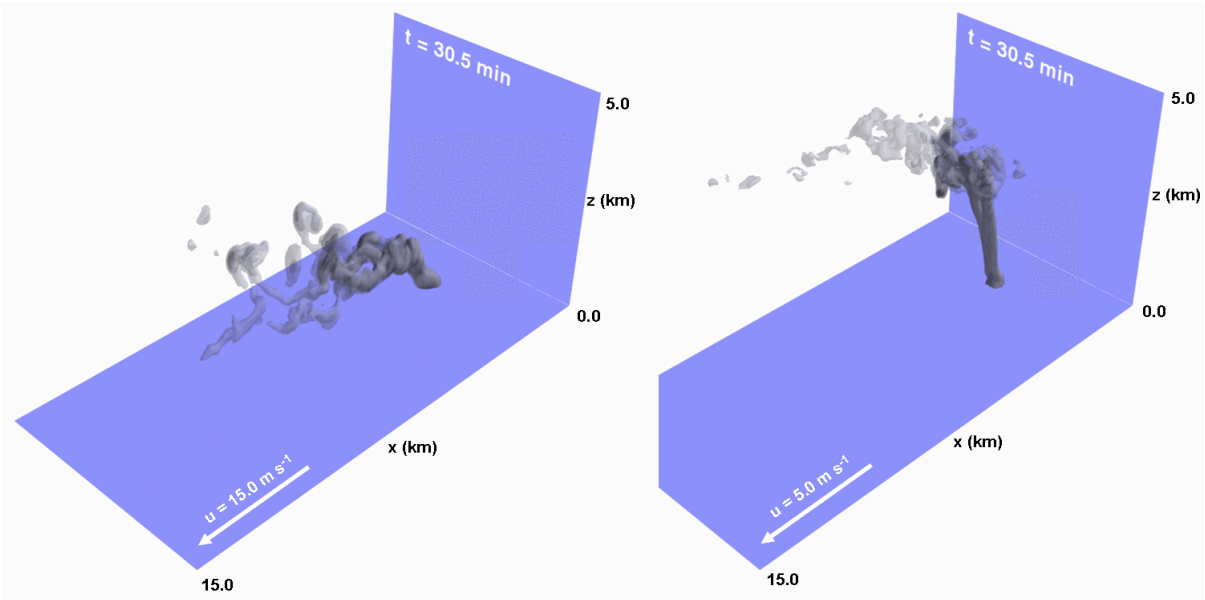

Figure 3 Snapshots of instantaneous concentration isosurfaces of a passive tracer released at a constant rate from surface over the area representing the fire. The left hand panel is the 15.0 m s^{-1} background-wind case and the right hand panel is the 5.0 m s^{-1} background-wind case.

Plume Simulations

We introduce an idealised bushfire plume into the simulations using a methodology similar to that of Devenish and Edwards (2009). A circular heat flux anomaly, of radius 250 m and intensity 1×10^5 W m^{-2}, is situated at the model's lower boundary, 2 km from the upwind boundary in the x-direction and equidistant from the lateral boundaries in the y-direction. It is to be noted that there is no direct feedback of the atmosphere back onto the fire in these simulations and therefore no capacity to investigate surface-driven fire spread. Therefore, in this configuration it is possible to isolate and study just the interaction between the plume and background conditions, without the confounding variable of the surface-fire behaviour.

The idealised surface "fire" is applied in all six background wind speed simulations and it is found that in each case, the resultant plume reaches a quasi-steady state after 30 minutes of integration time. The simulations are then integrated for a further 60 minutes to collect statistics of the "mean" plume behaviour, as well as instantaneous model output. A passive tracer is emitted from the surface over the area representing the fire, in order to aid plume visualisation. We first examine snapshots of the plume under a various background winds, to illustrate the plume behaviour under different regimes, before considering the "mean" plume behaviour for all wind conditions.

Snapshots of instantaneous tracer concentration isosurfaces, once the plumes under the 15.0 and 5.0 m s^{-1} background winds have reached a quasi-steady state, are shown in Figure 3. In the stronger background wind case the plume is very meandering and turbulent, all the way from the surface up to its maximum height. In the weaker background wind case, the plume's tracer isosurface is much smoother in the lower half, before becoming turbulent in its upper half. The lower half of the plume is seen to take the form of a pair of counter-rotating vortices.

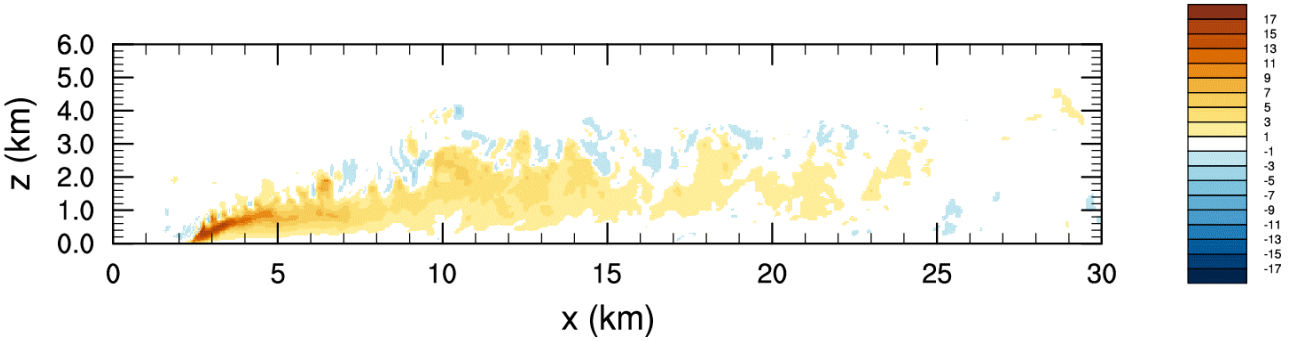

Figure 4. Snapshot of the instantaneous centreline vertical velocity (m s^{-1}) after 30 minutes of model time in the 15 m s^{-1} background-wind simulation.

The instantaneous vertical velocity snapshot of the plume with a 15 m s^{-1} background-wind (Figure 4) reveals substantially different behaviour of the plume under strong winds. In contrast to the 2 m s^{-1} background-wind case, the plume is very broad and bent over. It is much less intense, with a peak updraft of just over 16 m s^{-1}, and does not extend beyond the top of the mixed layer. Animation of the plume, not shown, reveals that the plume is very turbulent, exhibiting strong meandering and pulsing, despite the lack of direct feedback of the atmosphere onto the fire.

A snapshot of the instantaneous vertical velocity through the plume's centreline after 30 minutes of model time in the 2 m s^{-1} background-wind simulation is shown in Figure 5. The updraft is very narrow and also very intense, with peak vertical velocities in excess of 40 m s^{-1}. The plume is nearly vertically aligned and overshoots the top of the 3 km deep mixed layer by further 3 km. Animation of the plume, not shown, reveals that the location of the plume is very steady, except in the region above the mixed layer, where there is some weak meandering as the plume decelerates. This behaviour is consistent with the weak turbulence of the background wind in this case.

The properties of the "mean" plume for each background wind speed, calculated from 60 minutes of model integration in each case, are shown in Figure 6. The maximum updraft strength (Figure 6a) is found to vary smoothly from 41 m s^{-1} under a background wind speed of 2 m s^{-1} to 11 m s^{-1} under a background wind speed of 15 m s^{-1}. The maximum updraft alone is not necessarily a useful predictor for firebrand transport, so we also plot contours of the 6 m s^{-1} updraft for each background wind speed (Figure 6b). We chose this contour level as it is representative of a typical firebrand fall velocity (e.g. Ellis, 2010). Here we can see that although under weak-wind conditions the peak updrafts are of the order four times larger than under strong-wind conditions, the area of each individual plume that contains an updraft strong enough to suspend a typical firebrand is actually quite similar.

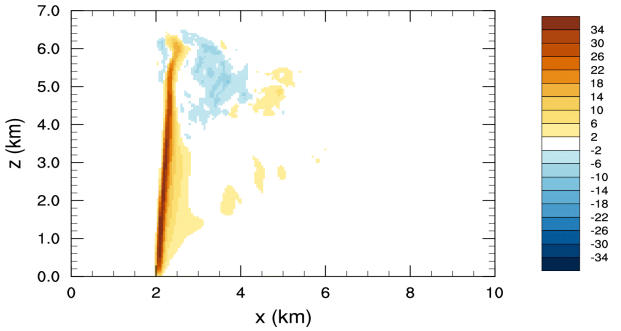

Figure 5. Snapshot of the instantaneous centreline vertical velocity (m s^{-1}) after 30 minutes of model time in the 2.0 m s^{-1} background-wind simulation.

Discussion and Conclusions

We have used the UK Met Office LEM to perform simulations that explore how idealised bushfire plumes vary in response to different background winds. We first took care to recreate realistic neutral, turbulent atmospheric boundary layers for a range of background wind speeds, under conditions designed to be representative of a typical high fire risk day. The plumes subsequently simulated across this range of wind speeds displayed a markedly different behaviour. Under weak background winds, plumes were intense, narrow, upright and smooth, whereas under strong background winds the plumes were comparatively weak, broad, bent over and turbulent.

Although the idealised fire prescribed here was relatively intense and simulated under a wide range of wind conditions, the plumes simulated here would unlikely be strong enough to give rise to long-range spotting in excess of 30 km. One potential reason for this is the lack of any moisture in either the fire or atmosphere, which is thought to play an important role in the dynamics of real-world fire plumes, particularly through the formation of pyrocumulonimbus [e.g. Cunningham and Reeder, 2009]. However, all plumes simulated contained substantial areas of updrafts that would be sufficiently strong to suspend a typical firebrand.

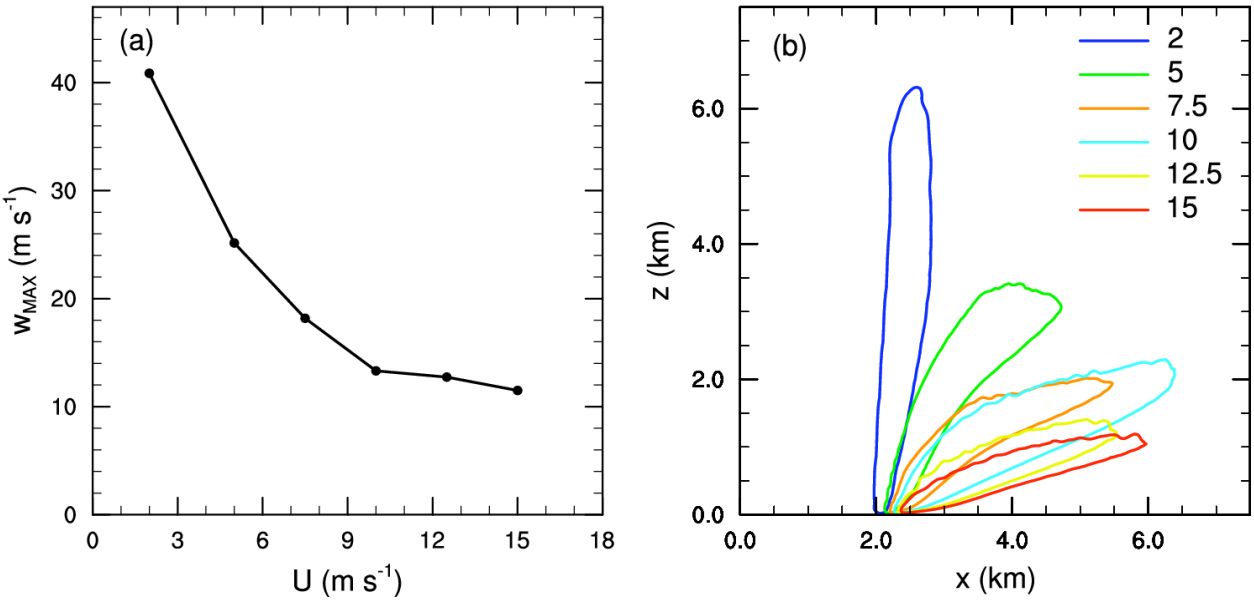

Figure 6 Properties of the plumes time averaged over one hour at quasi-steady state. (a) Maximum updraft speed (m s^{-1}) as a function of background windspeed (m s^{-1}) and (b) location of the 6 m s^{-1} updraft contour for each of the six background windspeed simulations.

The work presented here is currently being extended, primarily in two ways. Firstly, simulations are being repeated for a range of different heat fluxes, so that plume behaviour over a broad fire intensity—wind speed parameter space can be explored. Secondly, Lagrangian particle transport calculations will be performed using the velocity fields from the simulations. These will allow us to get some quantitative measure of the extent of spotting that these plumes could produce. Crucially, these calculations will also inform as to the longitudinal and lateral spread of the firebrand transport, which is lacking in simple spotting models currently used.

Acknowledgements

This research was partly supported by the Bushfire Cooperative Research Centre. We acknowledge the assistance of Adrian Hill and Ben Devenish (UK Met Office) in setting up the simulations. Thanks are also due to Andrew Sullivan (CSIRO) for useful discussions.

References

Andren, A., A. R. Brown, P. J. Mason, J. Graf, U. Schumann, C.-H. Moeng, and F. T. M. Nieuwstadt, 1994: Large-eddy simulation of a neutrally stratified boundary layer: A comparison of four computer codes. Q. J. Roy. Meteor. Soc. 120, 1457–1484.

Brown, A. R., S. H. Derbyshire, and P. J.Mason, 1994: Large-eddy simulation of stable atmospheric boundary layers with a revised stochastic subgrid model. Q. J. Roy. Meteor. Soc. 120, 1485–1512.

Cruz, M. G., A. L. Sullivan, J. S. Gould, N. C. Sims, A. J. Bannister, J. J. Hollis, and R. J. Hurley, 2012: Anatomy of a catastrophic wildfire: The Black Saturday Kilmore East fire in Victoria, Australia. Forest Ecol. Manag. 284, 269–285.

Cunningham, P. and M. J. Reeder, 2009: Severe convective storms initiated by intense wildfires: Numerical simulations of pyro-convection and pyro-tornadogenesis. Geophys. Res. Lett. 36, L12812, doi:10.1029/2009GL039262.

Devenish, B. J. and J. M. Edwards, 2009: Large-eddy simulation of the plume generated by the fire at the Buncefield oil depot in December 2005. Proc. R. Soc. A 465, 397–419.

Devenish, B. J., G. G. Rooney, and D. J. Thomson, 2010: Large-eddy simulation of a buoyant plume in uniform and stably stratified environments. J. Fluid Mech. 652, 75–103.

Ellis, P. F. M., 2010: The effect of the aerodynamic behaviour of flakes of jarrah and karri bark on their potential as firebrands. J. Roy. Soc. West. Aust. 93, 21–27.

Gray, M. E. B., J. Petch, S. H. Derbyshire, A. R. Brown, A. P. Lock, H. A. Swann, and P. R. A. Brown, 2001: Version 2.3 of the Met Office large eddy model: Part II. Scientific documentation. Turbulence and Diffusion Note 276, UK Met Office, Exeter, United Kingdom.

Mason, P. J. and D. J. Thomson, 1987: Large-eddy simulations of the neutral-static-stability planetary boundary layer. Q. J. Roy. Meteor. Soc. 113, 413–443.

Black Saturday 2009: A radar view of the Kilmore East fire

Tony Bannister
Bureau of Meteorology, Victoria Regional Office
1010 Latrobe Street, Docklands, Victoria
t.bannister@bom.gov.au

Introduction

The worst bushfire event in Australian recorded history occurred on Saturday 7 February 2009 in Victoria, Australia. Colloquially it has now become known as Black Saturday. One hundred and seventy three people lost their lives on this day with one hundred and twenty of these deaths occurring in the one fire, known as the Kilmore East fire. The Melbourne weather watch radar had an unparalleled view of the genesis and development of the Kilmore East fire. This paper presents some signature moments during the fire's development, connecting what is seen on radar with known locations of the fire front on the ground, as well as inferred connections based on the change in radar output at forest locations, known sources of enhanced fuel for the fire. The same technique is then successfully demonstrated on the Aberfeldy fire, which occurred in Victoria in January 2013.

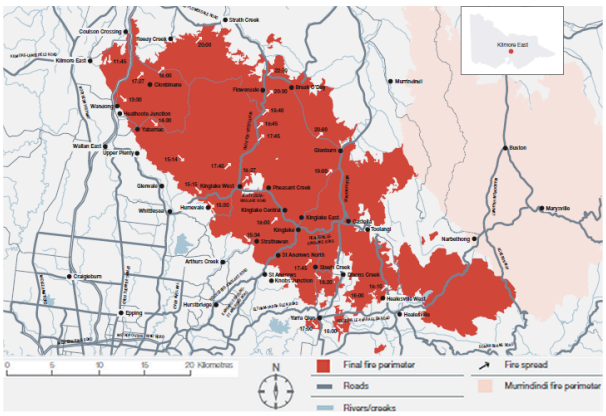

Figure 1 Final extent of the Kilmore East fire. (Victorian Bushfires Royal Commission 2009. Note times in reference are in Eastern Daylight Savings Time).

Observations by the Melbourne radar of the Kilmore East fire

From as far back as 1950 it has been known that precipitation radars are sensitive enough to detect plumes from fires (Jones 1950; Birch 1968; Reid and Vines 1972; Rogers and Brown 1997; Hufford et al., 1998). Jones et al. (2009), and Rogers and Brown (1997) indicate that precipitation radars are not sensitive to smoke particles (diameter typically less than 10 μm) but to the larger ash and burnt debris that is also lifted into the atmosphere. The Melbourne precipitation radar is an S-Band (10 cm) wavelength radar situated 19 km to the west southwest of the centre of Melbourne and was located about 55 km to the southwest of the Kilmore East fire (Figure 2). The radar completes a 14 elevation volume every six minutes with the lowest elevation scan (0.5 degrees) on the order of 200 to 400 metres above ground level over the Kilmore East fire-site.

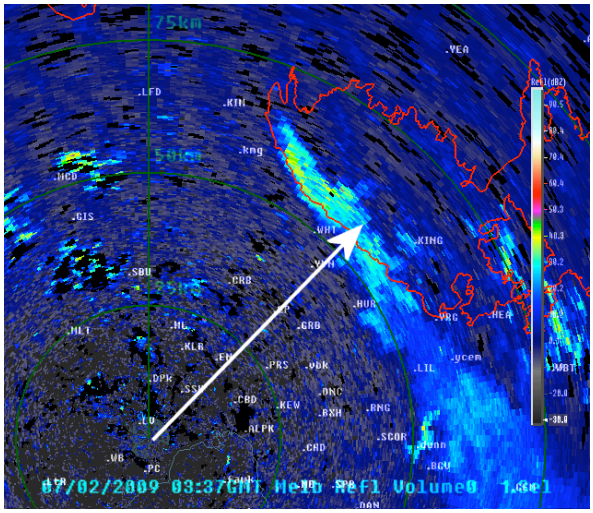

Figure 2 Radar reflectivity image of the fire taken from the Melbourne radar at 03:37 UTC. The red outline is the approximate final extent of the Kilmore East and Murrindindi fires. The arrow shows an indicative distance of 55 km from the radar to the fire.

The fire started at about 00:47 UTC near Kilmore East (Victorian Bushfires Royal Commission 2009). The first indication of the fire on radar is at 01:06 UTC. Figure 3 shows this radar scan, the immediate scan prior and the location in the landscape of the enhanced reflectivity echo associated with the fire. The 01:06 UTC reflectivity centre location is about 1 km from the leading edge of the 01:00 UTC fire perimeter (Figure 3c). Figure 4 shows a radar scan and the reconstructed fire perimeter 12 minutes later at 01:18 UTC. At this time there is no sign of the fire plume on the radar reflectivity image (Figure 4a). A possible explanation for this is reduced fuel load leading to reduced burn rate and smoke plume height.

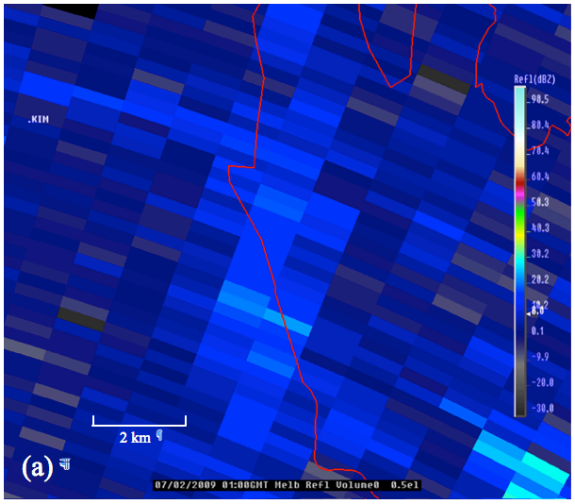

Figure 3a 01:00 UTC 0.5 degree elevation radar reflectivity image over fire area. Red outline is the approximate final reconstructed fire perimeter.

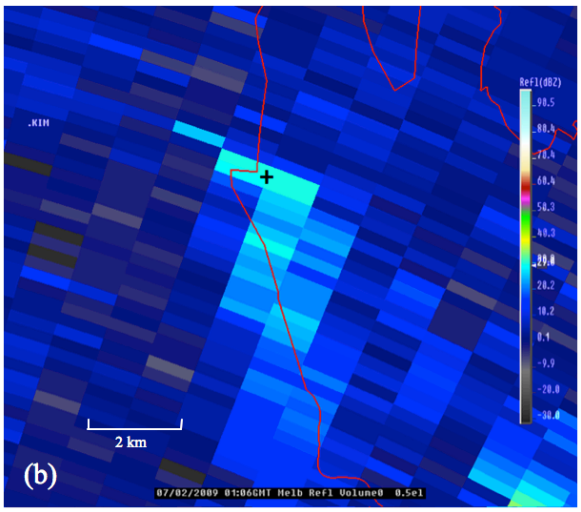

Figure 3b 01:06 UTC 0.5 degree elevation radar reflectivity image over fire area with the centre of maximum reflectivity marked by a '+' symbol on the first radar scan that showed evidence of the fire.

A comparison of Figure 3c and Figure 5b indicates that the fire moved southwards through grassy, sparsely treed terrain, which would have less available fuel than the fire location at around 01:00 UTC, which shows patches of denser treed areas. After another twelve minutes the Melbourne radar began to identify the fire plume again, as indicated by the 01:30 UTC radar reflectivity image (Figure 6a) and by 01:48 UTC radar reflectivity values have reached 37.5 dBZ (Figure 6b). In Figure 6c when the radar position of the maximum reflectivity is compared with the reconstructed fire perimeter at the same time, it is less than 1 km away. The leading edge of the fire has also moved into a more forested area, providing more available fuel to burn, this matches well with the increase in radar reflectivity levels in the area at the time.

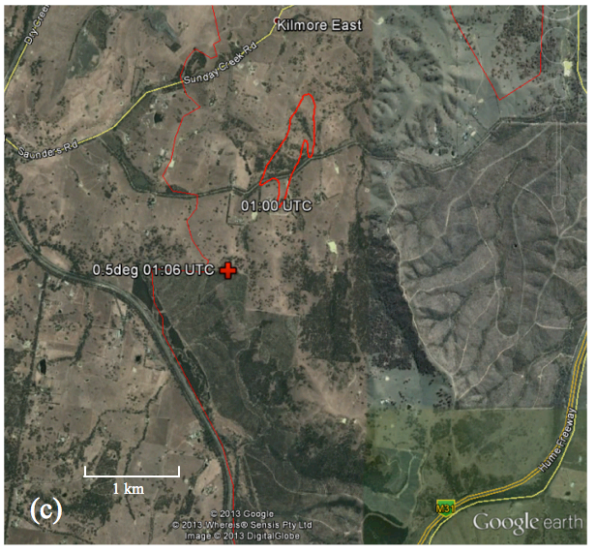

Figure 3c Location of the 01:06 UTC maximum reflectivity centre (red cross) compared with the reconstructed 01:00 UTC fire perimeter (thick red line) within the approximate final reconstructed fire perimeter (thin red line).

The Victorian Bushfire Royal Commission (2009) noted at this time 'from Saunders Road the fire travelled through about 200 hectares of plantation logging slash (the debris left by logging). With this fuel, the rate of the fire's spread towards the Hume Highway was estimated to be 2.5 km an hour.' The Victorian Bushfire Royal Commission (2009) also reported 'at 13:19 [AEDT, 02:19 UTC] the fire was recorded as highly likely to be spotting over the Hume Highway.

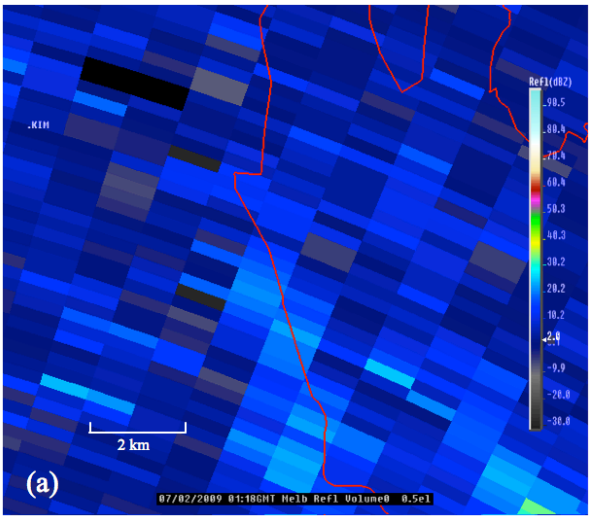

Figure 4a As Figure 3a for but at 01:18 UTC.

The combination of a high-intensity fire in the plantation logging slash and the presence of pockets of native vegetation beside the Hume Highway and on the median strip provided the quantity and arrangement of fine fuel to carry the fire across the highway'. This matches well with the 02:18 UTC Melbourne radar reflectivity image, the location of the maximum reflectivity value of 37.5 dBZ and the

darker green area of plantation forest just to the northwest of the Hume Freeway, as indicated in Figure 6(b).

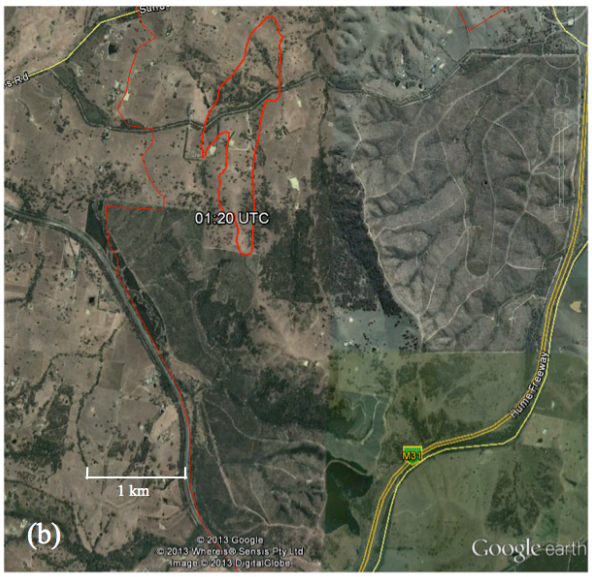

Figure 4b Reconstructed fire perimeter at 01:20 UTC within the approximate final reconstructed fire perimeter.

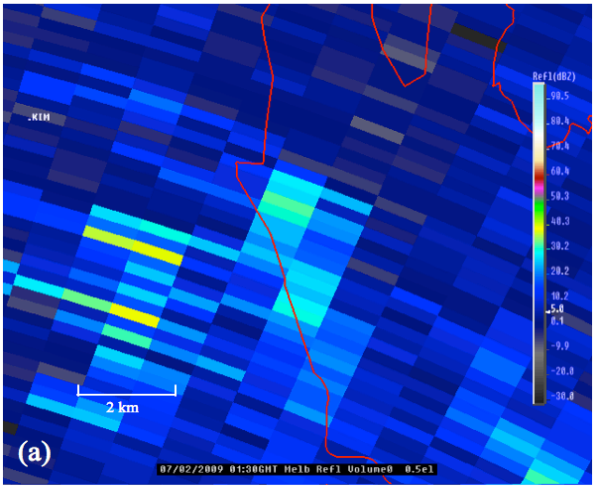

Figure 5a 01:30 UTC 0.5 degree elevation radar reflectivity image over fire area. Red outline is the approximate final reconstructed fire perimeter.

Comparison with radar observations of the Aberfeldy fire January 2013

At approximately 00:30 UTC 17 January 2013 a fire started near Aberfeldy in west Gippsland, Victoria (Country Fire Authority 2013). The fire burnt towards the southeast and the plume was visible from the Bairnsdale 5 cm C-band precipation radar, about 100 km to the east-southeast of the fire source. The radar's lowest 0.5 degree elevation scan is in the order of 700 to 1000 metres above terrain in the fire area. In Figure 7 locations of reflectivity maxima at four different times are shown. The first definitive radar indication of the fire plume was at 02:50 UTC, (white pin symbol), some two and a half hours after the estimated start of the fire.

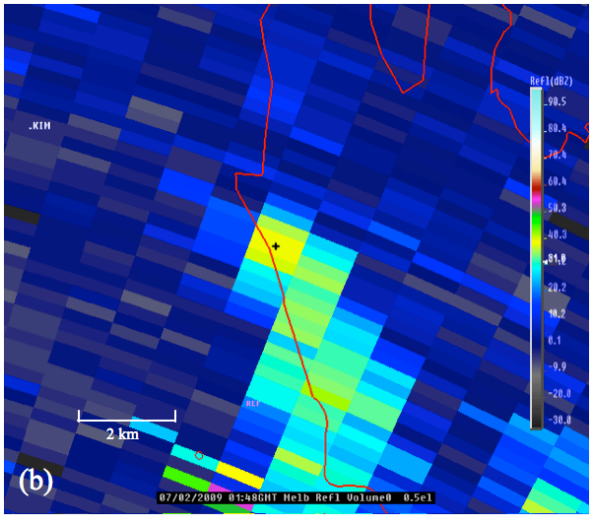

Figure 5b 01:48 UTC 0.5 degree elevation radar reflectivity image over fire area with the centre of maximum reflectivity marked by a '+' symbol on the first radar scan that showed evidence of the fire.

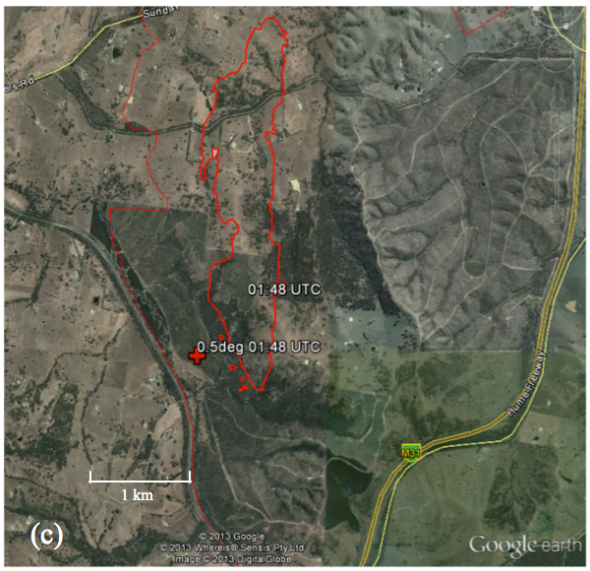

Figure 5c Location of the 01:48 UTC maximum reflectivity centre (red cross) compared with the reconstructed 01:00 UTC fire perimeter (thick red line) within the approximate final reconstructed fire perimeter (thin red line).

An 04:30 UTC maximum reflectivity radar location (red '+' symbol) is compared with the 04:30 UTC fire perimeter derived from an infrared linescan of the fire (red line). Finally 16:50 UTC and 17:00 UTC maximum reflectivity radar locations (green bulls eye symbols) are shown compared with the 17:00 UTC fire perimeter (green line). Again there is good agreement between radar maximum reflectivity locations and known fire front locations, even though Bairnsdale radar was further away and its lowest elevation scan was higher above the terrain when compared with the Melbourne radar view of

the Kilmore East fire.

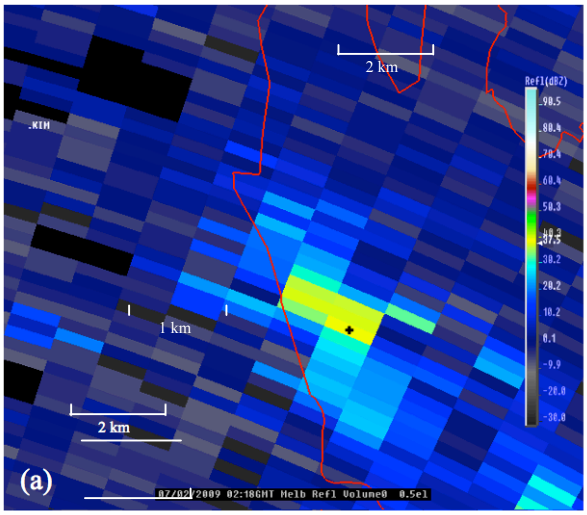

Figure 6a As for Figure 4a but at 02:18 UTC.

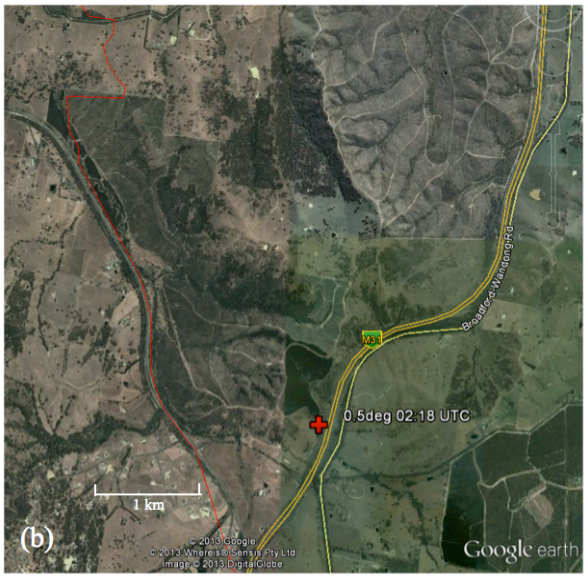

Figure 6b Location of 02:18 UTC maximum reflectivity (red-cross) within the approximate final reconstructed fire perimeter. The Hume Freeway is labeled as M31.

Conclusions

This paper suggests that careful interpretation of radar reflectivity data when a fire plume is visible within about 100 km of a radar can provide real time position information on the fire front, especially if the fire is burning through forested areas. This information could prove to be a valuable source of intelligence to fire agencies as to the current location of the fire front. Meteorologists, especially those working at State Control or Fire Centres should consider careful analysis of radar data when any fire plume is visible on radar.

Although not covered in this paper, research on plume intensity and height as measured by volumetric radar could also provide more real time intelligence on fire development for the fire agencies.

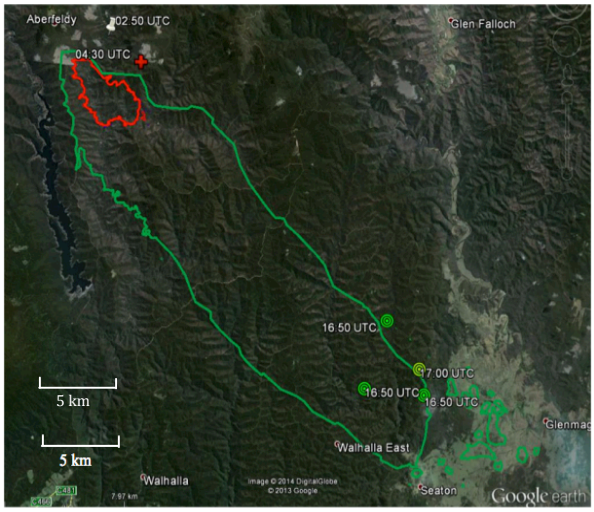

Figure 7 Perimeters of the Aberfeldy fire at 04:30 UTC (red) and 17:00 UTC (green). Locations of the 02:50 UTC, 04:30 UTC, 16:50 UTC and 17:00 UTC radar 0.5 degree elevation maximum reflectivities are shown.

Acknowledgements

The reconstructed Kilmore East fire perimeter data and Aberfeldy fire perimeter information derived from infrared linescans courtesy of Victorian Department of Environment and Primary Industries and the Country Fire Authority.

References

Birch, R. L., 1968: Radar observations of smoke. Australian Meteorological and Oceanographic Journal, 30.

Country Fire Authority, 2013: Witness appeal for Aberfeldy fire, viewed 29 August 2013, http://news.cfa.vic.gov.au/news-in-brief/item/484-.html

Hufford, G. L., H. L. Kelley, W. Sparkman, and R. K. Moore, 1998: Use of real-time multisatellite and radar data to support forest fire management. *Wea. Forecasting*, **13**, 592-605.

Jones, R. F., 1950: Radar Echoes from Smoke. Meteorological Magazine, London, **79**, 89.

Jones, T. A., S. A. Christopher, and W. Petersen, 2009: Dual-polarization radar characteristics of an apartment fire. *J. Atmos. Oceanic Technol.*, **26**, 2257-2269.

Reid, D. G. and Vines, R. G., 1972. A radar study of the smoke plume from a forest fire (No. 2). Commonwealth Scientific and Industrial Research Organization.

Rogers, R. R., and Brown, W. O. J., 1997: Radar observations of a major industrial fire. *Bull. Amer. Meteor. Soc.*, **78**, 803-814.

Victorian Bushfires Royal Commission, 2009: Victorian Bushfires Royal Commission Final Report , Vol 1. Melbourne: Government Printer for the State of Victoria.

Forecasting conditions conducive to blow-up fire events

R.H.D. McRae[A] and J.J Sharples[B]
[A]ACT Emergency Services Agency, PO Box 158, Canberra, ACT 2605, Australia
[B]Applied and Industrial Mathematics Research Group
School of Physical, Environmental and Mathematical Sciences
University of New South Wales, Canberra, ACT 2601.
rick.mcrae@act.gov.au

Introduction

All fires start small but may then escalate to larger size classes (McRae and Sharples, 2011). Large fire incidents are managed by Incident Management Teams (AFAC, 2011), who have the decision-making responsibilities for effective suppression and damage minimisation. They work in, typically, twelve hour shifts, with each shift guided by an Incident Action Plan (IAP). The IAP sets incident objectives, strategies and tactics – a hierarchical set of rules for that shift. These rules are set on the basis of expectations for how the incident will evolve during that shift.

From time to time fires will escalate into extreme fires (as defined by McRae & Sharples, 2011), and cause catastrophic damage levels. Over the last decade a wide range of scientific findings have greatly expanded our understanding of the processes driving such escalations (Fromm et al., 2006; Fromm et al., 2010; Fromm et al., 2012; Mills & McCaw, 2010; Peace et al., 2012; Potter, 2012a,b; Sharples et al., 2012a; Viegas, 2005). A fundamental requirement in the development of an extreme fire is what can be termed a blow-up fire event (McRae & Sharples, 2013), which refers to a discrete event involving uniformly intense fire activity across the entire affected landscape, with a typical downwind extent of the order of 10 km. An extreme fire involves one or more blow-up fire events.

While extreme fires are still too difficult to forecast reliably, blow-up fire events appear to be amenable to attempts to forecast their onset. If successful, such forecasts would form a significant first step towards a more comprehensive forecasting system. The diversity and dynamics of the drivers of blow-up fire events require a formal structure to be able to assess their respective contribution to blow-up fire behaviour. In this paper such a formal structure is proposed in the form of a process model (Figure 1). While this model does not yet represent a definitive framework for forecasting blow up fire events, it does incorporate a number of novel findings regarding dynamic fire escalation and combines them with a number of processes known to significantly affect fire escalation. As such it offers both a conceptual basis for forecasting blow up fire events, and a preliminary model for evaluation and development. The model is structured in such a way that it can be easily refined as new information arises. Aspects of the model framework have been discussed by McRae and Sharples (2013).

.

Information Needs

The typical concept of a weather forecasting system involves a duty meteorologist at a workstation with all required information available at their fingertips. By contrast, what is proposed here is utilisation of information from four groups.

Firstly, there are the traditional meteorological datasets: primarily wind, temperature and relative humidity/dew point temperature. Also included are compound indices of fire danger, as required for local needs, and atmospheric stability. There are well-developed information management systems for these. Fire danger indices are based on surface weather and antecedent climate conditions only, while the increasingly important Continuous Haines Index (Mills & McCaw, 2010) reflects vertical atmospheric profile data.

Secondly, there is information concerning the location, current extent, current dynamics and resulting predicted future extent of the fire concerned. These are provided by the fire agency. The timeliness of these is critical, and a metadata system is essential. The needs here are more critical than the existing field observations needs for Special Fire Weather Forecasts. A mutual understanding is required if field observers are to take measurements at places of maximum usefulness for the duty weather forecaster.

Thirdly, there is shared information. We are still in an era where operational numerical weather prediction (NWP) output is at a scale that is too coarse to resolve critical elements of local weather on the fireground.

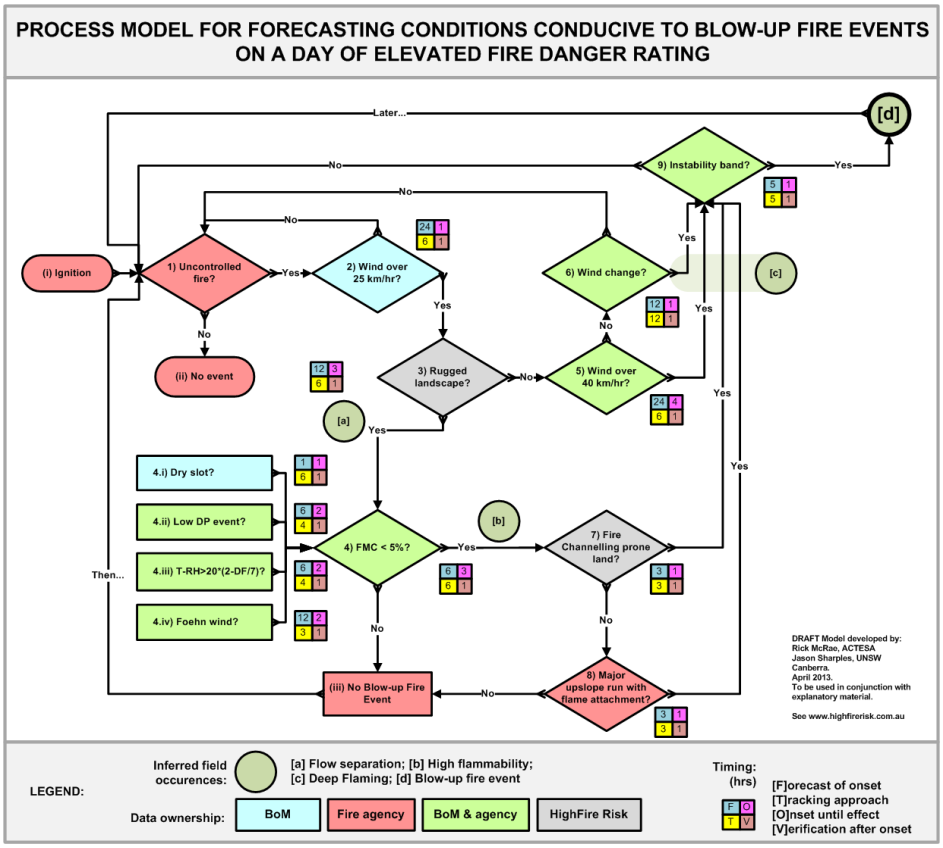

Figure 1 The process model.

As an example, at a fire on rugged terrain, the build-up of winds in the morning may cross a threshold beyond which lee-slope eddy winds begin to dominate. This change will alter fire dynamics. However, there will be a reliance on relevant field observations being passed on by the fire agency to the meteorological agency.

Finally there is external information. At present this refers to terrain analysis datasets that are in the public domain (e.g. HighFire Risk Project). These provide, among other things, the ruggedness class, wind regime and parts of the landscape that are prone to certain dynamic processes such as atypical lateral spread (Sharples et al., 2012a). These may be accessed by the weather forecaster or the fire agency.

These information classes overlap. The impact on the fire of a localised weather event (e.g. a foehn wind) may be inferred from the output of a NWP run, predicted by a specialist forecaster, or may only be observed in the field, depending on the event's scale and persistence (Sharples et al., 2010b). Inferring the occurrence of a foehn wind from a set of numbers reported from the field may be problematic. Increasingly, Situation Unit analysts are accessing non-standard weather products, such as water vapour imagery and aerological diagrams, which while commonly used by professional meteorologists have not in the past been typically disseminated to the general public. This may result in a more informed dialog or may result in faulty implicit assumptions, depending on the levels of training and familiarity. Also forecasters are increasingly working in the fire control centres ("outcasting") providing direct access to field information and facilitating the dialog.

Process Model

The process model (Figure 1) is a set of decision points that result in either (i) an expectation of a blow-up fire event occurring or (ii) a loop-back to the beginning. At this initial stage of the model development, decision points are treated as strictly binary [true]/[false] branches. For ease of use these have been tagged as [yes]/[no]. There is an exit point when a fire is determined to be controlled by the fire agency. The model applies to a fire ground, not a weather forecasting district or area.

The model has a set of parameters that set the repeat timing for the loops. As fire weather is typically handled on an hourly basis, the default repeat timing should be one hour, adjusted to the need of the incident. If a blow-up fire event occurs, the handling of its impacts becomes a priority, with looping resumed only when this urgency abates.

The model also contains points that permit the inference of physical events occurring on the fire ground. These form the outputs of the model.

Each "yes" branch from a decision point has a set of timing attributes. These are:

- Forecasting of onset. This is the typical number of hours of lead-time between determining that an event will occur and its actual occurrence. As an example, there may be a confident expectation of winds exceeding 25 km hr^{-1} at 10:00 local time, and this would arise in detailed forecasting at least 24 hours ahead.

- Tracking of approach. This is the typical time, in hours, over which it is feasible to track the approach of an event. To continue the previous example, wind trend observations over the preceding six hours or more would allow confirmation of the wind forecast.

- Onset to effect. This is the typical time, in hours, between the onset of the event and its full impact on the behaviour of the fire. In the above example, the effects of the winds picking up would be felt within one hour of its onset.

- Verification after onset. This is the typical time, in hours, that it would take for field observers to verify the onset of the event. Typically this is one hour. This verification would then be passed on to the duty weather forecaster.

Another aspect of the model is that it does not use compound fire danger and continuous Haines indices. Fire danger index can be considered as wind speed divided by fuel moisture content (FMC) (Sharples et al., 2009; Matthews, 2009), while the continuous Haines index involves lapse rate and dew-point temperature (DP) depression. An elevated fire danger index may arise from dry fuel, strong winds or some combination of the two. However, for blow-up fire event forecasting these are not equivalent; for example, the formation of ember storms is more likely under very low fuel moisture contents. In the model the separate components are used as needed.

Meteorology

A prior condition is a day of elevated fire danger rating. The determination of this is well handled by existing systems. Additional considerations in the process model include the following:

- Wind over 25 km hr^{-1}? [Data ownership: BoM.] The prior condition of elevated fire danger rating may come about due to strong winds, very low fuel moisture levels or a combination of both. These two possible inputs are explored in separate questions.

- Rugged landscape? [Data ownership: public domain, e.g. HighFire Risk Project.] Landscape ruggedness has been formally defined (www.highfirerisk.com.au/maps) as being areas where the range of elevation (i.e. local relief) within 1.5 km of any point exceeds 300 m. If a fire is burning on or near rugged terrain there will be a specific set of wind – terrain interactions that affect fire behaviour and evolution.

- Inferred Event [a]: Flow separation. With prevailing winds over 25 km hr^{-1} and in rugged terrain, it is nearly certain that flow separation eddies will occur in the lee of ridgetops perpendicular to the prevailing wind (Sharples et al., 2010a). While chaotic on short time-scales, these eddy winds average-out to a uniform process on the time-scales used for fire weather forecasting. The significance of this is that on the lee-facing slopes a spotfire will be burning upslope with the wind, and may be of equivalent intensity to a fire on the windward face, and equally able to create new spotfires downwind. Flow separation is also a key pre-requisite for fire channelling occurrence (Sharples et al. 2012a; Simpson et al. 2013).

- FMC < 5%? [Data ownership: Fire agency and BoM.] If one or more of the group of four following events occurs then there is a low fuel moisture event underway. This indicates conditions under which fires may spread easily and where spotfires may take quickly and efficiently.

    - Dry slot? [Data ownership: BoM.] Mills (2005) showed that the passage of what has been termed a dry slot over an active fire may cause sudden catastrophic fire escalation. Dry slots may be detected in water vapour band satellite imagery. Using hourly-repeat-time imagery it is possible to track one and forecast its arrival time at the fire ground.

    - Low DP event? [Data ownership: Fire agency and BoM.] There are processes that may cause dry air to impact high ground. There, the surface experiences a significant drop in dew point temperature and resultant changes to fire behaviour. These processes include, but are not limited to subsidence inversions and low-level jets (Sharples, 2009; Sharples et al., 2012b).

    - (T – RH) > (40 – 20 DF / 7)? [Data ownership: Fire agency and BoM.] If true, this formula (Sharples et al., 2009) indicates a situation where the diurnal variation in temperature (T) and relative humidity (RH) produce low fuel moisture levels. Note that this requires the current drought factor (DF), which on a local scale may be topographically heterogeneous.

    - Foehn wind? [Data ownership: Fire agency and BoM.] Case studies of catastrophic fires (e.g. Fromm et al., 2012) in Australia and the US have shown that a common element in many blow-up fire events is a precedent foehn wind event (Sharples et al., 2010b), often during the preceding night or morning. This has the effect of preventing moistening of fine fuel prior to the arrival of elevated fire danger. This facilitates fire escalation, often earlier than might be forecast or expected.

- Wind over 40 km hr^{-1}? [Data ownership: Fire agency and BoM.] With an uncontrolled fire present on a day of elevated fire danger, strong winds will create

deep flaming, due to very high headfire spread rates. The time for ignited fuel to burn-out may be considered a constant, so the elevated spread rates will carry the flames further during the burn-out time.

- Wind change? [Data ownership: Fire agency and BoM.] As has been seen many times, notably on the flat plains of Victoria, when a wind change hits a fast moving fire, the flank may suddenly become a new, much wider headfire. While the post-change air is usually moister (raising fuel moisture levels) there will be a time lag of around an hour before conditions ameliorate. Some wind changes are preceded by DP drop-out events (Mills, 2007). Also, duty forecasters are skilled at assessing the impact of pre-frontal dynamics on fire weather (Claire Yeo, pers. comm.).

- Fire-channelling-prone land? [Data ownership: HighFire Risk.] On certain sufficiently steep and lee-facing slopes a fire channelling event may initiate (Sharples et al., 2012a). The combined effect of fire spread downwind, through dense spotting, and lateral spread along the zone of flow separation results in deep flaming; i.e. a transition from frontal to areal fire involvement.

- Major upslope run with flame attachment? [Data ownership: Fire agency.] Certain upslope landform geometries will cause flames to attach to the surface and affect a fire's spread rate (Viegas, 2005). The headfire spread rate may continue to increase without limit until the top of the terrain feature is reached. This has been responsible for a number of burn-over events (Viegas et al., 2005).

- Inferred Event [c]: Deep Flaming. Information gathered during major fires (such as the example in Figure 2) has shown that a deep flaming zone is a necessary (but not sufficient) prerequisite for the development of: blow-up fire events; violent pyro-convection; and pyroCbs.

- Instability band? [Data ownership: Fire agency and BoM.] A blow-up fire event may be produced by the combination of (i) the presence or development of a local environmental profile characterised by atmospheric instability (Mills, 2005; Fromm et al. 2012) and (ii) deep flaming. Dry slots, trough lines or fronts would be used for this purpose.

- Inferred Event [d]: Blow-up fire event. This is the ultimate goal of this process model. Having reached this point there is a strong likelihood that one or more places within the fire area will develop a blow-up fire event in the near future. Warnings and safety messages for the community and fire crews are essential. There is also a strong possibility of violent pyro-convection occurring, leading to an extreme fire. There may even be a pyroCb produced.

It will be seen that this set of meteorological events covers: the surface weather behind fire danger, the profile weather behind the continuous Haines Index, and localised weather on the fire ground.

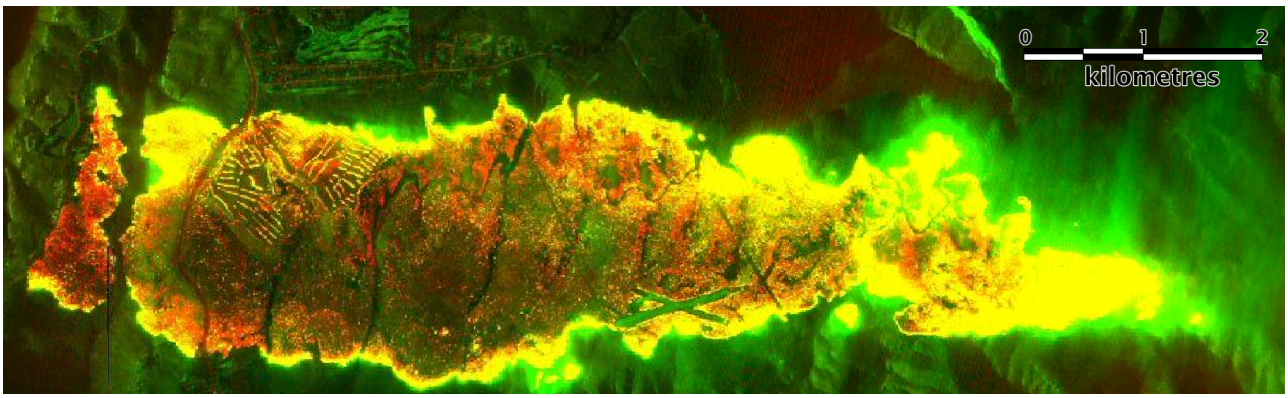

Figure 2 Deep flaming (yellow), Blackheath, NSW, 5 December 2002. Linescan: NSW Rural Fire Service.

Implementation Case Study

Ti-Tree Creek Fire of December 17, 2009 (near Michelago, NSW): The key to successful implementation of this model is a collaboration between the duty weather forecaster and the Situation Unit analysts in the IMT. An hourly dialog during which the key questions are addressed will allow the model to cycle through. The day had been forecast as a day of elevated fire danger rating, so the model was valid. The FDR peaked in the early afternoon, and this peak occurred on a deepening trough-line. When a fire started in the early afternoon (at around 13:00 local time) in fully cured grasslands, the elevated FDR allowed it to defy initial attempts to bring it under control, so Q1 (as in Figure 1) was true. Winds were over 25 km hr^{-1}, so Q2 was true. Initially it was on undulating lands, so Q3 was false. The winds in the region were marginally over 40 km hr^{-1}, but the ignition was in a

sheltered area. Q5 required direct observations from the fire ground, but in their absence it may have been assumed to be false. No wind change was due until later, so Q6 was initially false. So, initially the model would loop back.

Fire behaviour analysis indicated that, if uncontrolled, the fire would arrive on rugged landscapes in the order of one hour. Therefore at 14:00 local time Q3 was expected to become true. Using Cooma Airport AWS observations for the time of ignition, the temperature of 33°C and the relative humidity of 11%, along with a drought factor of 9, gave an FMI of just under 5 (corresponding to an FMC of roughly 2% or 3%). Thus deteriorating conditions indicated true for Q4 at 14:00 local time. The terrain at this location was modelled as fire channelling prone for the prevailing winds (NW), setting Q7 to true.

The synoptic situation had a trough approaching from the southwest. This provided the instability environment required to suggest Q9 was true or would become true in the near future. This line of reasoning would suggest, soon after ignition, that a blow-up fire event would be likely if the fire reached the rugged terrain after one hour. The preparation and issuing of specific public warnings in this setting is always a challenge, and needs to be initiated as soon as the threat is realised.

When an inference of a blow-up fire event is made, a stylised impact footprint should be applied. This is roughly 15 km long downwind of the initiation point and 12 km wide. Anything within that footprint is considered to be under threat. Uncertainty in the initiation point can be added to this. Just over an hour after ignition the fires entered rugged terrain on the Tinderry Mountains. As expected at the time, a blow-up fire event did occur. A stylized threat footprint was used operationally.

Discussion & Conclusions

A forecast of elevated fire danger rating is a broad-brush tool for forecasting threats to the community. With large populations affected, it is problematic to know how to ensure maximised safety. On days of elevated fire danger rating some fires will escalate and others will not, creating issues with false alarms and warning desensitisation. There is a wide recognition of a need for better tools. The process model proposed above relegates elevated fire danger rating to a precursor.

The process model offers a prospect of forecasts of a key component of the catastrophic wildfires that have affected Australia many times in the last decade. It requires different approaches to those currently used, but the potential benefits are significant. A key feature is the collaboration needed to follow this process model, turning the generation of a forecast into a true dialog. Better community warnings and improved fire crew safety are likely.

As mentioned already, the proposed model does not yet constitute a definitive forecast tool. At this stage the model incorporates processes that have been shown to significantly affect fire behaviour, but it is likely that there remain other processes that could lead to a blow up fire event that have yet to be identified. Moreover, many of the decisions required to implement the model need to be made more quantitative to facilitate operational implementation.

Given the inherent uncertainties in observations of fire behaviour and meteorological forecasting, further development of the model framework may also benefit from a more probabilistic approach in place of the binary methodology discussed above. Bayesian decision networks offer a natural framework for extension of the model in this respect.

At present the authors would advocate a trial evaluation of the proposed forecasting technique, perhaps in combination with a number of detailed case studies. Given the Australian origins, the most likely validations will come from wildfires in south-eastern or south-western Australia during the next austral Summer and Autumn, and perhaps the ones after. Additional validation may come from the US during the boreal fire season. It is then likely that the results could be applied in other areas with similar fire weather patterns with little additional validation.

This validation would require prior identification of areas of raised fire danger rating with established fires and incident objectives of suppression of the fire (large fires in inland Australia are often not suppressed). A trial dialog between a non-duty weather forecaster and the fire agency's Incident Management Team would be established with the goal of producing a forecast product and comparing it to the eventual outcome in the field. After enough trials, the efficacy of the proposed model would be established and an implementation decision may be made from that.

Acknowledgements

The authors acknowledge the efforts of Aurora Bell (BoM) in organising the Science for Services workshop, and Claire Yeo (BoM/CAWCR) for providing useful advice on the topic of this paper. We also thank the anonymous reviewers, who provided helpful contributions to improving this

paper.

References

AFAC. 2011. *The Australasian Inter-service Incident Management System, Revised Edition, 2011*. Australasian Fire and Emergency Services Council, Melbourne.

Fromm, M., D.T. Lindsey, R. Servranckx, G. Yue, T. Trickl, R. Sica, P. Doucet, and S. Godin-Beekmann. 2010. The Untold Story of Pyrocumulonimbus. *Bulletin of the American Meteorological Society*. September 2010: 1193-1209.

Fromm, M. R. McRae, J. Sharples, and G. Kablick. 2012. Pyrocumulonimbus Pair in Wollemi and Blue Mountains National Parks, 22 November 2006. *Australian Meteorological & Oceanographic Journal*, **62:** 117-126.

Fromm. M, A. Tupper, D. Rosenfeld, R. Servrancx, and R. McRae. 2006. Violent pyro-convective storm devastates Australia's capital and pollutes the stratosphere. *Geophysical Research Letters,* **33**, L05815.

Matthews, S. 2009. A comparison of fire danger rating systems for use in forests. *Australian Meteorological and Oceanographic Journal*, **58:** 41-48.

McRae, R., and J. Sharples. 2011. A conceptual model for assessing the risk posed by extreme bushfires. *Australian Journal of Emergency Management* **26:** 47-53.

McRae, R.H.D., and J.J. Sharples. 2013. A process model for forecasting conditions conducive to blow-up fire events. *Proceedings, 2013 MODSIM Conference*, *Adelaide, SA*.

Mills, G.A. 2005. On the sub-synoptic scale meteorology of two extreme fire weather days during the Eastern Australian fires of January 2003. *Australian Meteorological Magazine*, **54:** 265-290.

— 2007. On easterly changes over elevated terrain in Australia's southeast. *Australian Meteorological Magazine,* **56:** 177-190.

Mills, G.A., and L. McCaw. 2010. *Atmospheric Stability Environments and Fire Weather in Australia – extending the Haines Index*. CAWCR Technical Report No. **20**.

Peace, M., L. McCaw, and G. Mills. 2012. Meteorological dynamics in a fire environment; a case study of the Layman prescribed burn in Western Australia. *Australian Meteorological & Oceanographic Journal*, **62:** 127-142.

Potter, B.E. 2012a. Atmospheric interactions with wildland fire behaviour - I. Basic surface interactions, vertical profiles and synoptic structures. *International Journal of Wildland Fire*, **21:** 779-801.

— 2012b. Atmospheric interactions with wildland fire behaviour - II. Plume and vortex dynamics. *International Journal of Wildland Fire*, **21:** 802-817.

Sharples, J.J. 2009. An overview of mountain meteorological effects relevant to fire behaviour and bushfire risk. *International Journal of Wildland Fire*, **18:** 737-754.

Sharples, J.J., R.H.D. McRae, R.O. Weber, and A.M. Gill. 2009. A simple index for assessing fire danger rating. *Environmental Modelling and Software*, **24**: 764-774.

Sharples, J.J., R.H.D. McRae, and R.O. Weber. 2010a. Wind characteristics over complex terrain with implications for bushfire risk management. *Environmental Modelling and Software*, **25:** 1099-1120.

Sharples, J.J., G.A. Mills, R.H.D. McRae, and R.O. Weber. 2010b. Foehn-like Winds and Elevated Fire Danger Conditions in Southeastern Australia. *Journal of Applied Meteorology and Climatology*, **49:** 1067-1095.

Sharples, J.J., R.H.D. McRae, and S.R. Wilkes. 2012a. Wind–terrain effects on the propagation of wildfires in rugged terrain: fire channelling. *International Journal of Wildland Fire*, **21**: 282-296.

Sharples, J.J., G.A. Mills, and R.H.D. McRae. 2012b. Extreme drying events in the Australian high-country and their implications for bushfire risk management. *Australian Meteorological and Oceanographic Journal*, **62:** 157-170.

Simpson, C.C., J.J. Sharples, J.P. Evans, and M.F. McCabe. 2013. Large eddy simulation of atypical wildland fire spread on leeward slopes. *International Journal of Wildland Fire*, **22:** 599-614.

Viegas, D.X. 2005. A mathematical model for forest fires blowup. *Combustion Science and Technology*, **177:** 25-51.
Viegas, D.X., L.P. Pita, L. Ribeiro, and P. Palheiro. 2005. Eruptive Fire Behaviour in Past Fatal Fire Accidents. *Proceeding, Eighth International Wildland Fire Safety Summit, Missoula, MT*.

The Australian National Thunderstorm Forecast Guidance System: New calibrated ensemble-based total thunderstorm probabilities

Harald Richter
The Centre for Australian Weather and Climate Research
Bureau of Meteorology, Docklands, Victoria
h.richter@bom.gov.au

Introduction

The production of thunderstorm forecasts for days one to seven is common practice in Australian weather forecast offices. Such forecasts form part of the office's "forecast policy" (which guides all other products issued by the office), an explicit graphical day 1 or day 2 thunderstorm forecast issued for specialized clients, or as an input into public or aviation forecasts, just to name a few.

At present, an ingredients-based algorithm, the National Thunderstorm Forecast Guidance System (NTFGS; Hanstrum 2004), provides a qualitative diagnosis of four types of deep convective storms or storm systems (surface-based thunderstorm, midlevel thunderstorm, tropical squall line and supercell) and four types of severe convective hazards (straight-line winds, hail, heavy rain and tornadoes). The NTFGS algorithm ingests a single 12.5 km deterministic non-hydrostatic operational model - the "Australian Community Climate and Earth System Simulator - Australian domain" ACCESS-R12 model (Puri et al. 2012), to diagnose the eight outputs just described in a categorical manner – either as dichotomous not favourable/favourable or trichotomous not favourable/favourable/very-favourable decisions. While based on sensible ingredients (Johns and Doswell 1992) and thresholds, the system is not calibrated against observations, and clearly exhibits tendencies to overpredict some of the diagnostics, such as thunderstorms over the tropical oceans (Richter 2012).

Bright et al. (2005) described a physically based system that predicts the calibrated probabilities for the combination of the NTFGS's surface-based and midlevel thunderstorm diagnostics (hereafter "calibrated thunder"). When coupled to a customized version of the National Centers for Environmental Prediction (NCEP) Environmental Modeling Center's (EMC) Short Range Ensemble Forecast (SREF) system (Du et al. 2004; Bright et al. 2004), the calibrated thunder diagnostic performed very well, in particular in terms of its reliability (Bright et al. 2005). It was these credentials that swayed the author to port the calibrated thunder algorithm across to Australia and couple it to AGREPS-R, the regional ACCESS ensemble prediction system. AGREPS-R is the Bureau of Meteorology's ensemble system that is most similar to SREF.

Description of the un-calibrated thunder algorithm

The calibrated thunder algorithm employs two predictors sourced from output of the 24-member AGREPS-R ensemble. The total 3-hourly precipitation must exceed 0.25 mm, and the Cloud Physics Thunder Parameter (CPTP) must exceed 1.

The CPTP attempts to capture three basic ingredients of cumulonimbus electrification. A sufficiently warm temperature T_{LCL} >= -10°C at the Lifted Condensation Level (LCL) is necessary to supply the updraft with supercooled liquid water. The presence of convective available potential energy (CAPE) in excess of 100 J kg^{-1} in the mixed phase region where graupel and supercooled liquid water coexist (the 0°C to -20°C layer; correspondingly $CAPE_{-20}$ >= 100 J kg^{-1}) is seen as a proxy for adequate vertical motion in the updraft to lift graupel above the charge-reversal temperature zone around -15°C to -20°C, and to replenish the updraft with supercooled liquid water. Finally, a cold equilibrium level temperature (T_{EL} <= -20°C) ensures that the updraft extends beyond the charge reversal temperature zone. Accordingly, the CPTP is formulated as

$$CPTP = \begin{cases} \frac{(-19^{\circ}C - T_{EL})(CAPE_{-20} - K)}{K}, & \text{if } T_{LCL} > -10^{\circ}C; \\ 0, & \text{otherwise.} \end{cases}$$

Here, K = 100 J kg^{-1} is a constant that scales the CPTP in such a way that CPTP > 1 can be considered indicative of the presence of a storm environment that is favourable for cloud electrification, given the occurrence of deep moist convection. The value of 100 J kg^{-1} for K, according to Bright et al. (2005), is based on operational experience in the United States and will be subject to sensitivity testing against verification results in future work. To allow for the formation of surface-based and elevated

thunderstorms, the CPTP computation is based on the *most unstable parcel*, rather than a variant of surface parcel.

Table 1 P1 and P2 are the probabilities of CPTP > 1 and P_{tot} > 0.25 mm based on the ensemble member fractions, respectively. For example, a grid cell in Figure 1 where 15 (out of 24) ensemble members satisfy the condition CPTP > 1 (P1 = 0.625) and 9 members in Figure 2 satisfy P_{tot} > 0.25 mm (P2 = 0.375) is now assigned bin number 51.

P1/P2	0-5%	5-15%	15-25%	25-35%	35-45%	45-55%	55-65%	65-75%	75-85%	85-95%	95-100%
0-5%	Bin#1	Bin#2	Bin#3	Bin#4	Bin#5	Bin#6	Bin#7	Bin#8	Bin#9	Bin#10	Bin#11
5-15%	Bin#12	Bin#13	Bin#14	Bin#15	Bin#16	Bin#17	Bin#18	Bin#19	Bin#20	Bin#21	Bin#22
15-25%	Bin#23	Bin#24	Bin#25	Bin#26	Bin#27	Bin#28	Bin#29	Bin#30	Bin#31	Bin#32	Bin#33
25-35%	Bin#34	Bin#35	Bin#36	Bin#37	Bin#38	Bin#39	Bin#40	Bin#41	Bin#42	Bin#43	Bin#44
35-45%	Bin#45	Bin#46	Bin#47	Bin#48	Bin#49	Bin#50	Bin#51	Bin#52	Bin#53	Bin#54	Bin#55
45-55%	Bin#56	Bin#57	Bin#58	Bin#59	Bin#60	Bin#61	Bin#62	Bin#63	Bin#64	Bin#65	Bin#66
55-65%	Bin#67	Bin#68	Bin#69	Bin#70	Bin#71	Bin#72	Bin#73	Bin#74	Bin#75	Bin#76	Bin#77
65-75%	Bin#78	Bin#79	Bin#80	Bin#81	Bin#82	Bin#83	Bin#84	Bin#85	Bin#86	Bin#87	Bin#88
75-85%	Bin#89	Bin#90	Bin#91	Bin#92	Bin#93	Bin#94	Bin#95	Bin#96	Bin#97	Bin#98	Bin#99
85-95%	Bin#100	Bin#101	Bin#102	Bin#103	Bin#104	Bin#105	Bin#106	Bin#107	Bin#108	Bin#109	Bin#110
95-100%	Bin#111	Bin#112	Bin#113	Bin#114	Bin#115	Bin#116	Bin#117	Bin#118	Bin#119	Bin#120	Bin#121

The probability is derived from the percentage of ensemble members that satisfy the exceedance condition above. Note that all values that are more than 300 km offshore are masked out. With a greater prominence of warm rain processes in maritime areas (potentially requiring adjusted predictors) and the absence of high cloud-to-ground (CG) lightning detection efficiencies by the Global Position and Tracking System (GPATS; see below for the calibrative role of these data) far offshore it was seen as prudent not to extend the calibrated thunder algorithm to these areas.

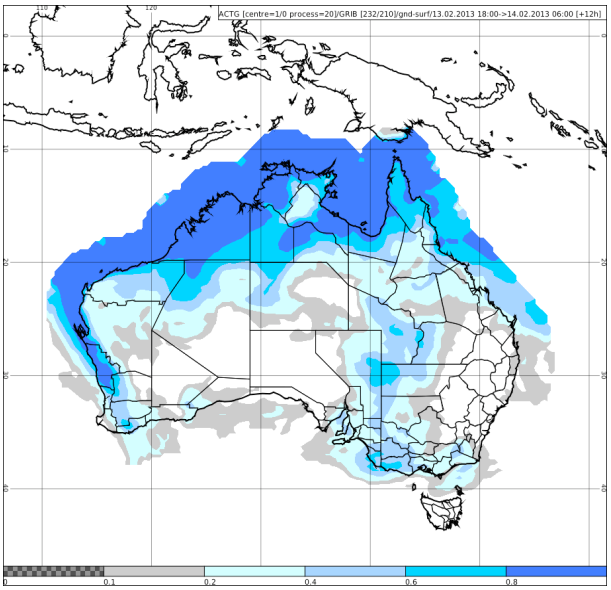

Figure 1 Probability of CPTP > 1 for a 12-hour AGREPS-R forecast valid at 0600 UTC on 14 February 2013. The colour fill intervals start at 10% (grey), 20%, 40%, 60% and 80% (dark blue). Values more than ~300 km offshore are masked out.

The presence of a thermodynamically favourable parcel for electrification relies on the existence of cumulonimbus clouds. The calibrated thunder algorithm utilizes the condition that deep convection is only possible if the total precipitation P_{tot} exceeds 0.25 mm in a model grid box during a 3-hour period (ending at the time when CPTP is calculated). This exceedance probability for the same forecast as before is shown in Figure 2.

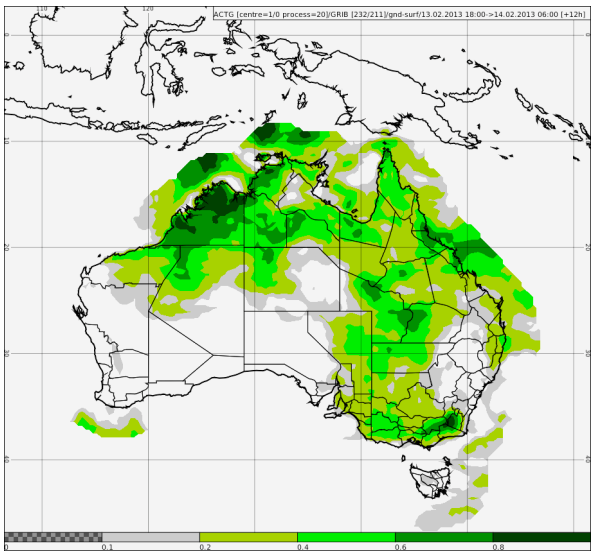

Figure 2 Probability of Ptot > 0.25 mm for a 12-hour AGREPS-R forecast valid at 0600 UTC on 14 February 2013. The colour fill intervals start at 10% (grey), 20%, 40%, 60% and 80% (dark green).

Total rather than convective precipitation is used based on some convective parameterization schemes not activating if elevated convection sources its inflow from layers that are hundreds of hPa above ground level (Bright et al. 2005). The probabilities of CPTP > 1 and P_{tot} > 0.25 mm are treated as independent. The joint probability should then form the unconditional and uncalibrated (unc) probability of CG lightning given by P_{unc} = P(CPTP > 1) x P(P_{tot} > 0.25 mm). Figure 3 shows the spatial distribution of the uncalibrated probability of total thunder for our case example. It is apparent that the large probabilities of CPTP > 1 over the warm oceans surrounding Australia are modulated by the total precipitation exceedance probability.

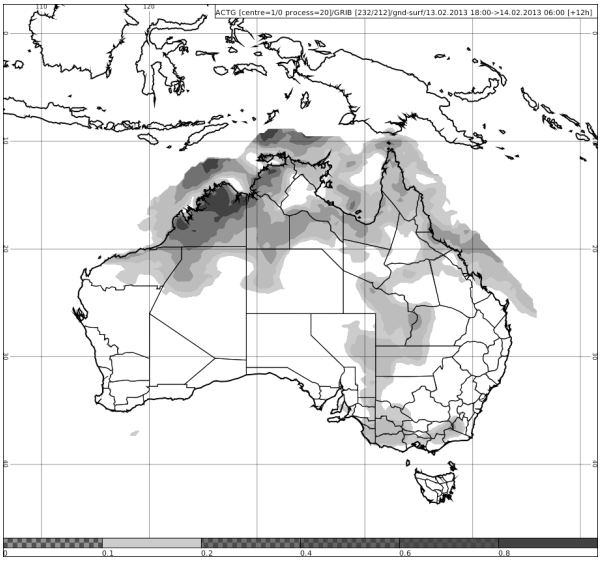

Figure 3 Uncalibrated probability of total thunder calculated as a product of the exceedance probabilities for the CPTP (Figure 1) and P_{tot} (Figure 2). The thresholds of the shaded probabilities are 10%, 20%, 40%, 60% and 80%.

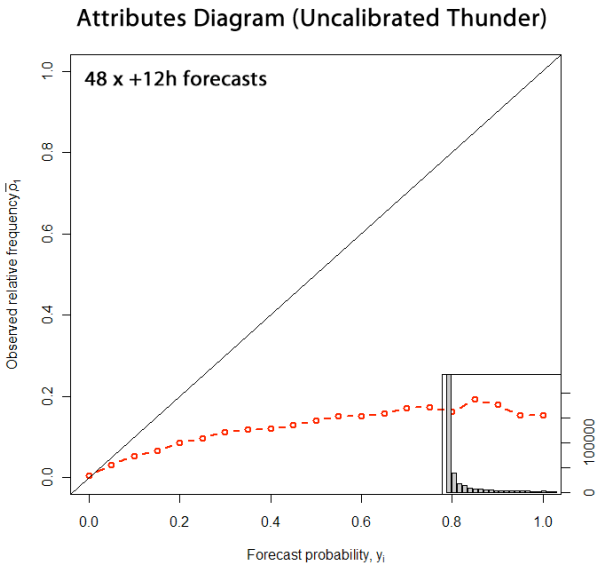

Figure 4 Reliability diagram for 48 separate 12-hour forecasts of uncalibrated thunderstorm probabilities each valid during the local afternoon (0600 UTC) during the validity period 16 January 2013 – 5 March 2013. The histogram in the lower right-hand corner shows how often each of the forecast probability bins occurred across all forecasts. The bin width is 0.05, which means, as an example, that the bin associated with a forecast probability value of 0.4 collects all grid points with probability values in the interval $0.375 < y_i \leq 0425$.

The ground-based CG lightning location system, GPATS, can be used to verify the uncalibrated thunder predictions. The uncalibrated ensemble-based discrete probability values (0, 1/24, 2/24, ..., 1) shown in Figure 3 are binned into the values y_i = 0, 0.05, 0.1, 0.15, ..., 0.95, 1. All pixels of a specific probability y_i are collected, and the fraction o_i of those pixels that experienced one or more CGs during the period 0300-0600 UTC is then plotted against y_i in Figure 4. All pairs i = 1,...,21 of forecast probability and observed frequency make up the reliability curve of the uncalibrated thunder forecast. In Figure 4 a perfectly reliable algorithm would produce a reliability curve along the diagonal $y_i=o_i$ (for all i). While the spatial pattern of the uncalibrated thunderstorm probabilities might be of good quality, they also overforecast the observed CG frequency dramatically. For example, a predicted 70% of thunder is matched by an observed frequency of thunder of less than 20%. This well-known overprediction tendency of ingredients-based predictors of rare events can be corrected through the calibration procedure described next.

Description of the calibration method

The two predictors (CPTP > 1 and P_{tot} > 0.25 mm) of the CG lightning prediction system at hand jointly identify CG-promoting environments more often than they actually occur. In a hope that this overprediction can be attributed to a bias rather than random error, Bright et al. (2005) proposed a simple calibration methodology to remove the bias apparent in Figure 4.

First, the exceedance probabilities for the two predictors are binned into eleven bins each (0-5%, 5-15%, 15-25%, ..., 95-100%) which leads to a matrix of 121 possible uncalibrated probability combinations (Table 1). Now, each forecast can be plotted as a grid of these bin numbers (not shown). For the 12-hour forecast valid at 0600 UTC on 14 February 2013 used in this example, all 12-hour forecasts valid at 0600 UTC over the last 30 days are considered for the calibration. Across all grid boxes during the 30 day calibration period that are classified as bin *i* (i=1...121), the fraction P_i of grid cells where one or more CGs were observed by GPATS during the 0300-0600 UTC period is determined and allocated to bin *i* as its *calibrated* probability of CG lightning. Now the ensemble-based forecast of the uncalibrated exceedance probabilities for CPTP and P_{tot} in our example (Figs. 1,2) can be converted into a forecast of calibrated probabilities for total thunder (Figure 5).

For the sample of 48 forecasts considered in this study, the calibrated probabilities are far more reliable than their uncalibrated counterparts (compare Figures 4 and 6). For calibrated forecast probabilities up to 15% the system is very reliable (Figure 6). Even during the summer period (monsoon season) considered here, only a few areas in Australia tend to have calibrated forecast probabilities exceeding 15% (Figure 5), so that the system can be considered reliable across the vast

majority of the Australian continent. At higher probabilities (20% and above), the system overpredicted the occurrence of CGs.

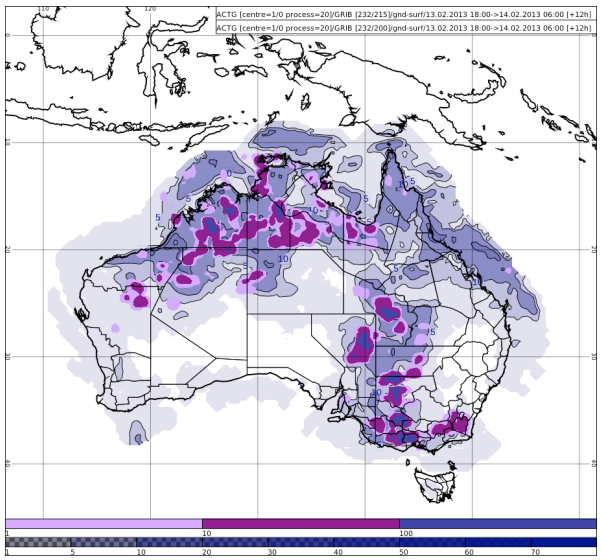

Figure 5 Calibrated total thunder probability for a 12-hour AGREPS-R forecast valid at 0600 UTC on 14 February 2013. The colour fill intervals are 1%, 5%, 10%, 15% and 20%. The overlaid colour-filled field is the cloud-to-ground (CG) lightning flash density over the 3-hour period 0300-0600 UTC and a ~37.5 km x 37.5 km area matching the model footprint.

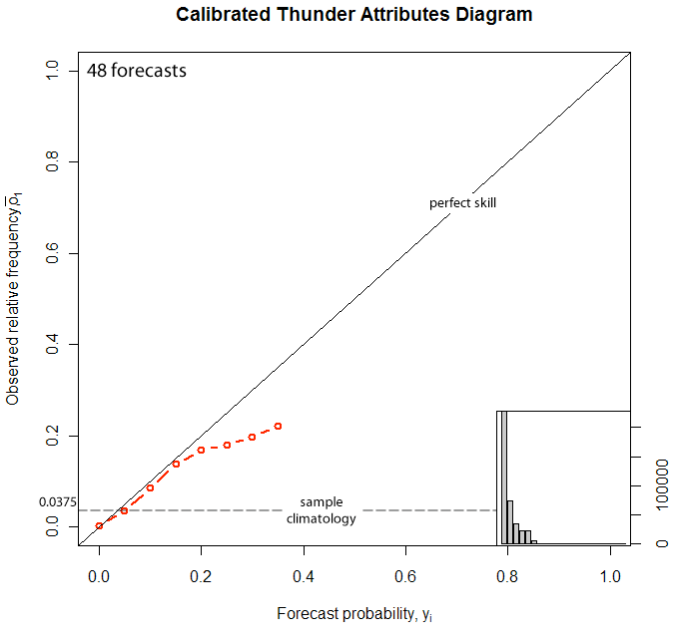

Figure 6 Same as Figure 4 but for the *calibrated* thunderstorm probability.

One reason for this overprediction is a small sample size for some bin numbers (across the 30-day calibration period), so that the associated fraction of bins experiencing one or more CGs is sensitive to the lightning observations. A second reason is a shift in lightning activity observed against particular bin numbers, from a more lightning active regime in late January and early February to a less active one from mid-February onwards.

Comparison of the NTFGS with calibrated thunder

Although the combined NTFGS forecasts for surface-based and midlevel storms is a categorical forecast, its performance can still be compared to the probabilistic calibrated total thunder forecast. A categorical (yes/no) total thunder forecast from the NTFGS can be evaluated by populating the standard 2 x 2 contingency table where a Hit (H) means that an event (in this case total thunder = yes) was predicted and observed, a False Alarm (FA) is an event that was predicted but not observed, a Miss (M) is an event that was not predicted but was observed, and a Correct Null (CN) is an event that was neither predicted nor observed. The spatial distribution of these verification metrics for the 12-hour forecast valid 0600 UTC 14 February 2013 is shown in Figure 7. The NTFGS total thunderstorm diagnosis shows that the false alarms outweigh the hits, particularly in the tropics. Surprisingly, given a commonly perceived overprediction bias of the NTFGS, a range of missed events occurred in western Queensland, western New South Wales, eastern South Australia and northern parts of Western Australia and the Northern Territory.

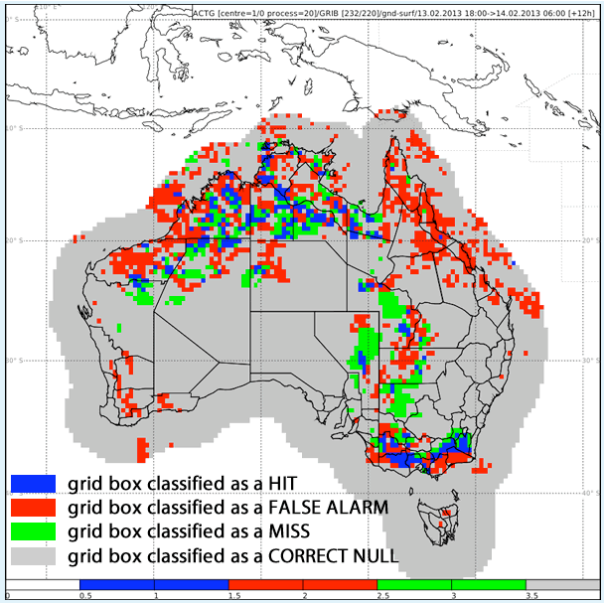

Figure 7 Spatial plot of the 2x2 categorical forecast verification results for the total thunderstorm forecast of the 12-hour NTFGS algorithm valid at 0600 UTC 14 February 2013.

The concept of categorical forecast verification can also be extended to probabilistic forecasts if the total thunder probability prediction is converted into a categorical prediction based on a specified probability threshold P*. For example, for P*=10%,

all predicted total thunder probabilities P < 10% are considered as "event not predicted", while all predictions P >= 10% are now considered as "event predicted." When categorizing the calibrated probabilistic forecast shown in Figure 5 against a range of thresholds P_1* ... P_n*, the attendant 2 x 2 contingency tables allow for the calculation of the False Alarm Rate F = FA / (FA + CN) and the hit rate POD = H/(H + M). The points (FA_1,H_1), ..., (FA_n,H_n) linked to each probability threshold can now be plotted in a Relative Operating Characteristics (ROC) curve (Figure 8).

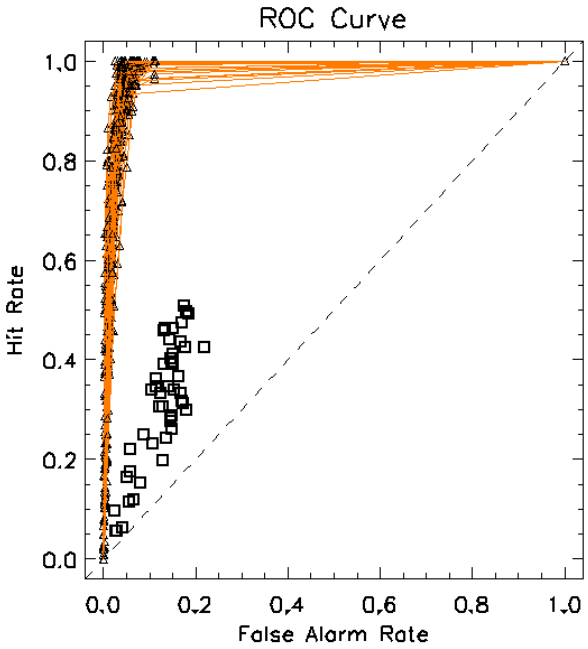

Figure 8 The Relative Operating Characteristics (ROC) for the operational NTFGS system (squares) and the ensemble-based calibrated thunder forecasts (orange curves) for the same 48 forecasts as in Figure 4.

For any probabilistic prediction system, one would expect that with decreasing threshold P* the number of hits (H) and the number of false alarms (FA) would increase while the number of misses (M) would decrease. These tendencies imply that F and POD trend towards 1 as P* approaches zero. In a well-performing prediction system the false alarm rate would increase more slowly than the hit rate, so that in Figure 8 the trace (0,0) – (0,1) – (1,1) would mark the perfect operating characteristic of a prediction system (Wilks 1995). With this interpretation tool in mind, Figure 8 clearly shows that calibrated thunder outperforms the NTFGS system with a spectacular margin.

Figure 8, as one example, sheds some light on why the NTFGS total thunder prediction showed inferior operating characteristics compared to the calibrated thunder algorithm in the 48-member sample of this study. The number of hits is approximately equal to the number of misses, which caps the hit rate around 0.5. At the same time, a significant number of false alarms (relative to the correct nulls) allowed the false alarm rate to move right in the ROC curve of Figure 8.

Conclusions

The present work details how an experimental probabilistic ensemble-based CG lightning (or "total thunderstorm") prediction system has been tested at the Bureau of Meteorology in Australia. This calibrated thunder approach, described in Bright et al. (2005), has been applied to the output of a 24-member Regional ACCESS ensemble prediction system (AGREPS-R) and 48 12-hour forecasts were produced, valid during the local afternoon (0600 UTC), and during the summer / wet season.

This study shows that for low probability events such as thunderstorms, environment-based predictors have a tendency to overpredict the actual likelihood of thunderstorm occurrence, which suggests that bias removal through calibration is an important component of a reliable thunderstorm prediction system. The AGREPS-R calibrated thunder system is very reliable for thunderstorm probabilities up to about 15%, and trends towards overprediction thereafter.

Within this sample of 48 warm season afternoon predictions, the AGREPS-R calibrated thunder system performs significantly better than the operational NTFGS system, as gauged by the respective relative operating characteristics.

Future work will examine the AGREPS-R calibrated thunder performance for longer forecast lead times and for predictions of non-afternoon storms, which are more likely to be elevated. Sensitivity tests are also planned that will study the influence of some of the calibration or predictor parameters (such as the calibration period of 30 days, or the CPTP scaling constant K) on the system performance.

Acknowledgements

Special thanks goes to Steve Weiss, Israel Jirak and Andy Dean from the Storm Prediction Center in Norman, Oklahoma, for the initial discussions of the calibrated thunder approach. I am also grateful to Tim Hume who produced the coastal mask for this study.

References

Bright, D.R., S.J. Weiss, J.J. Levit, M.S. Wandishin, J.S. Kain, and D.J. Stensrud, 2004: Evaluation of short-range ensemble forecasts during the 2003 SPC/NSSL Spring Program. Preprints, *22nd Conf. Severe Local Storms,* Hyannis, Massachusetts, Amer. Meteor. Soc., CDROM (P15.5).

Bright, D. R., M. S. Wandishin, R. E. Jewell, and S. J. Weiss,

2005: A physically based parameter for lightning prediction and its calibration in ensemble forecasts. Preprints, *Conf. on Meteor. App. of Lightning Data,* San Diego, CA.

Du, J., J. McQueen, G. DiMego, T. Black, H. Juang,E. Rogers, B. Ferrier, B. Zhou, Z. Toth and M. S. Tracton, 2004: The NOAA/NWS/NCEP short-range ensemble forecast (SREF) system: evaluation of an initial condition vs. multi-model physics ensemble approach. Preprints, *16th Conference on Numerical Weather Prediction,* Seattle, Washington, Amer. Meteor. Soc., CD-ROM (21.3)

Hanstrum, B. N., 2004: A National NWP based thunderstorm and severe thunderstorm forecasting guidance system. *Preprints, International Conference on Storms, AMOS 11th National Conference 5-9 July 2004*, Brisbane, Australia, 31-36.

Johns, R. H., and C. A. Doswell III, 1992: Severe local storms forecasting. *Wea. Forecasting*, **7**, 588–612.

Puri, K., G. Dietachmayer, P. Steinle, M. Dix, L. Rikus, L. Logan, M. Naughton, C. Tingwell, Y Xiao, V. Barras, I. Bermous, R. Bowen, L. Deschamps, C. Franklin, J. Fraser, T. Glowacki, B. Harris, J. Lee, T. Le, G. Roff, A. Sulaiman, H. Sims, X. Sun, Z. Sun, H. Zhu, M. Chattopadhyay, C. Engel, 2012: Implementation of the initial ACCESS Numerical Weather Prediction system, *Aust. Met. Oc. Journal,* submitted.

Richter, H., 2012: The Australian National Thunderstorm Forecast Guidance System: Current design, verification and future plans. Preprints, *26th Conf. on Severe Local Storms*, Nashville, TN.

Wilks, D. S., 1995: *Statistical Methods in the Atmospheric Sciences*. Academic Press, 476 pp.

Observational climatology and anomaly maps of the continuous Haines index

S.A. Louis
NSW Severe Weather Section
Bureau of Meteorology
Sydney, 2000, N.S.W., Australia.
S.Louis@bom.gov.au

Introduction

The continuous Haines (cHaines) index has recently been adopted by the Bureau as one of the main indices used to gauge the potential for instability driven fire behaviour. The main study defining and investigating the efficacy of the cHaines index (Mills and McCaw 2010) found that while the cHaines was correlated to some degree with the Forest Fire Danger Index (FFDI, McArthur 1967), there was also a component of independent information that could assist with discriminating likely days of unusual fire behaviour. The report also looked at a large number of case studies that demonstrated the utility of the cHaines index.

However, one major difficulty in working with cHaines, either as an aid to forecasting, or as a means of communicating the risk of atmospheric stability effects to fire agency personnel, is that we do not have a good grasp of what particular values of cHaines mean, either in a physical sense (i.e. implications for fire behaviour) or a climatological sense. One problem is that the correlation between cHaines and FFDI means that an unusually high value for cHaines on a day of low FFDI may be just average on a day of Severe FFDI. Even if an average cHaines value could be calculated, the idea of using a straight anomaly is complicated by the fact that the index is constrained at the upper and lower limit.

The main previous study into the cHaines index in Australia (Mills and McCaw 2010) used gridded reanalysis data and considered the 95th percentile value of cHaines at each grid point to be climatologically significant. The report separately considers the climatological significance of the FFDI, again using the 95th percentile. A number of climatological studies of the mid-level Haines index using observational data have been performed for different parts of Australia (Bally 1995; Long 2006; McCaw et al. 2007), but no climatological work has been done on cHaines using observations.

This work is intended to complement Mills and McCaw 2010 by producing an observational climatological data set for the cHaines index, and proposing a forecast tool for diagnosing areas where the forecast cHaines is climatologically unusual for the corresponding forecast FFDI. One important caveat is that the FFDI is designed to give an indication of the difficulty of suppressing a going fire in a forested area (McArthur 1967), and does not apply to areas with grassland and some other fuel types (e.g. coastal heath).

Data

Observational data at thirteen upper air stations in southeast Australia were used to build the climatology. These stations are detailed in Table 1. Four of the stations (Cobar, Moree, Wagga Wagga and Woomera) are in predominately grassland and semi-arid locations. The FFDI incorporates soil and deep duff fuel moisture via the Keetch-Byram Drought Index (KBDI), which assumes that evapotranspiration is a function of the density of vegetation cover, which is in turn a function of the mean annual rainfall (Keetch and Byram 1968). In this paper we assume that this proxy inclusion of vegetation density in the process of approximating the soil moisture will produce a sensible value of the FFDI in grassland and semi-arid areas. As discussed above however, any application of the FFDI in assessing likely fire behaviour will only be valid in forested areas.

Table 1 Weather observation sites used.

Station	Station Number	Latitude	Longitude	Elevation (m)	Number of data points
Adelaide	23034	-34.95	138.52	6	13588
Canberra	70014	-35.30	149.20	578	262
Cobar	48027	-31.48	145.83	260	12921
Coffs Harbour	59040	-30.31	153.12	5	207
Laverton	87031	-37.86	144.76	20	9535
Melbourne	86282	-37.67	144.83	113	4145
Moree	53048,53116	-29.49	149.85	212	5628
Mount Gambier	26021	-37.75	140.77	63	13629
Nowra	68076,68072	-34.95	150.54	109	8356
Sydney	66037	-33.95	151.17	6	11959
Wagga Wagga	72150	-35.16	147.46	212	13477
Williamtown	61708	-32.79	151.83	9	13689
Woomera	16001	-31.16	136.81	167	13149

To create a data set of paired cHaines and FFDI values, the 3pm (local time) FFDI data from a high quality observational fire danger index data set

(Lucas 2010) were matched to the cHaines data. The hour at which upper air observational data is available varies greatly; from station to station, at different periods in the climate record as observing policy has changed, and also from day to day as the result of faulty equipment and failed launches. To be as consistent as possible but still capture enough data points for a robust analysis, only upper air observations taken between 3am and midday were considered. In some cases, for a particular day there were multiple upper air observations within this window to ensure that each day only corresponded to one data point in these cases the earliest observation within the 3am to midday window was used.

Any days where either the cHaines or FFDI values were missing were removed from the data set to create an aggregate total of 120544 paired cHaines-FFDI data points. The data for all stations were combined to create a larger total set of data points for statistical analysis, under the assumption that as an upper air index the spatial variation in cHaines is likely to be less significant than the correlation with the surface conditions (i.e. FFDI). One limitation of the observational data set is that there is no way to consider the diurnal variation of the cHaines index, however a study of the daily correlation between the two indices is still valuable, as previous work has found that the diurnal variation in the cHaines index is relatively weak (Mills and McCaw 2010).

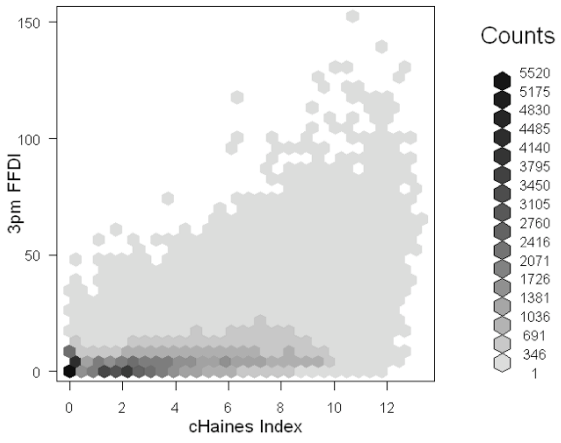

Figure 1. Density scatter plot showing the distribution of cHaines-FFDI data points.

Analysis

The distribution of the aggregated cHaines-FFDI data points (Figure 1), demonstrates that there is a moderate but clear correlation between the two indices, with a correlation coefficient of 0.47. At higher values of FFDI, the distribution of cHaines values shifts towards the upper end of the scale, while at lower values of FFDI the distribution of cHaines values covers the entire range of possible values. To assess how unusual a particular value of cHaines is, we should take this correlation into account. Note that for lower FFDI values there are two maxima in the distribution of cHaines index, with one of these corresponding to a cHaines value of zero. This is due to the fact that the formula defining cHaines would permit negative values, but a lower limit of zero is arbitrarily imposed. To allow for fit to normal distributions, for the remainder of the analysis the data points where cHaines=0 are ignored.

In order to assess how unusual a particular cHaines value is at any given point, ideally the bivariate distribution of cHaines and FFDI should be independent of the spatial location of the observation. Figure 2a shows simplified bag plots (which are a 2D form of a standard 1D box plot) for each of the stations, as well as for the aggregated data set. The curves in the bag plots correspond to an area containing 50\% or all data points, and the crosses show an approximate location of the bivariate median. To simplify Figure 2a, stations with similar distributions to each other have been plotted using the same colour.

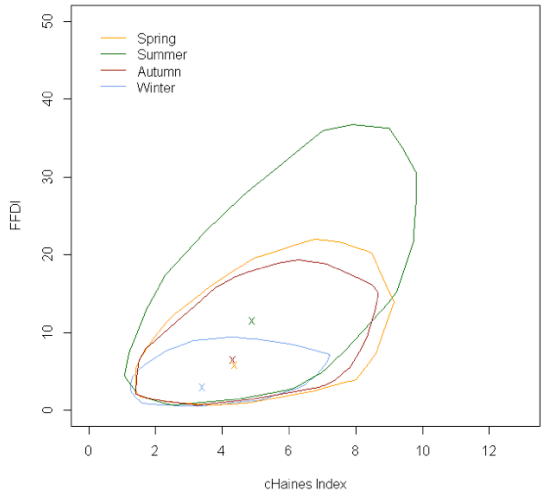

Figure 2a Simplified bag plots of the bivariate distributions of cHaines and FFDI for each of the station locations. Shown are Wagga (green); Cobar, Moree and Woomera (red); Composite dataset (black); and remaining stations along the coast and ranges (blue).

From a subjective assessment it is clear that the distributions are quite similar for all of the stations along the coastline or ranges, but that there is a different relationship between cHaines and FFDI for the stations in arid interior locations. The dry, inland stations show a significantly higher median for both cHaines and FFDI, and also a higher correlation between the two indices. The correlation coefficients range from a maximum of 0.585 at Woomera to a minimum of 0.37 at Coffs

Harbour. Wagga Wagga, on the inland slopes of the ranges, has a distribution that is intermediate between the two types. The composite from all station data produces an intermediate distribution quite similar to that from Wagga Wagga. The composite data set has a median of FFDI of 5.4 and cHaines index of 3.8, as well as a correlation coefficient of 0.49.

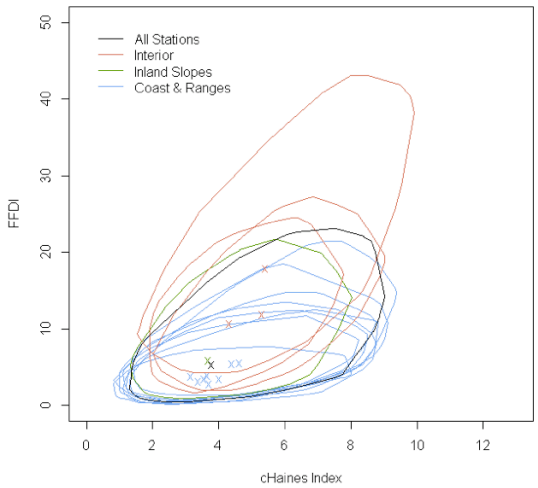

Figure 2b Simplified bag plots of the bivariate distribution of cHaines and FFDI at different times of year; summer (DJF,dark green), autumn (MAM,red), spring (SON,orange), winter (JJA,blue).

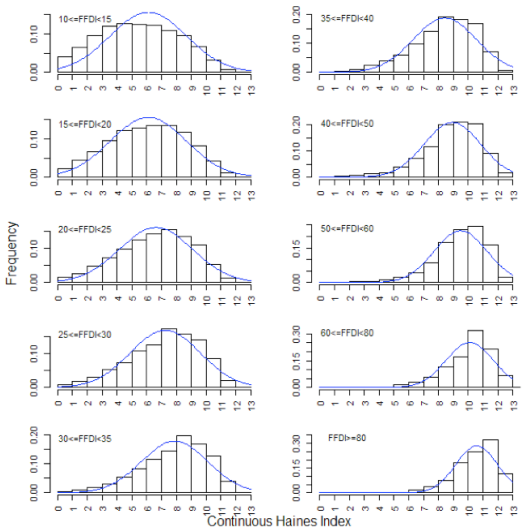

Figure 3 Histogram of cHaines values with fitted normal distribution for cHaines data broken down by FFDI value.

The relationship between the FFDI and the cHaines index also shows some seasonal variation (Figure 2b), with a correlation coefficient in winter of 0.33 compared to a correlation coefficient in summer of 0.522. The summer median conditions across all stations are a FFDI of 11.6 and a cHaines index value of 4.9, while the median winter conditions across all stations are a FFDI of 3.1 and a cHaines index value of 3.4. One likely factor in the location and seasonal variation in correlation between the two indices could be the fuel state input to the FFDI, the drought factor. Inland sites will generally have a higher drought factor than locations along the coast and ranges, and this proxy for fuel dryness responds on much longer time scales than the other weather elements that make up the cHaines index and FFDI.

To proceed we will assume that the composite data set is representative of the overall relationship between cHaines and FFDI, but it is important to keep in mind that there is some spatial and seasonal variation. One possible way to assess the climatological significance of a cHaines index value is to bin the data into subsets based on the FFDI value. The vast majority of FFDI values fall towards the lower end of the scale, so to minimise the difference in size of subset, uneven FFDI ranges were selected. We can consider each of these subsets to be a sample of cHaines values, and fit a normal distribution. Figure 3 shows histograms for each subset of cHaines value, again demonstrating quite clearly that the distribution shifts to the right for higher values of FFDI.

Table 2 Number of data points and sample mean and standard deviations for each of the subsets of cHaines data.

FFDI Range	Data Points	Sample Mean (μ)	Sample Standard Deviation (σ)
>80	161	10.572	1.397
60-80	543	10.103	1.594
50-60	743	9.489	1.780
40-50	1735	8.938	1.902
35-40	1529	8.427	2.125
30-35	2341	7.880	2.224
25-30	3306	7.252	2.353
20-25	4928	6.633	2.457
15-20	7246	6.113	2.556
10-15	11693	5.530	2.643
5-10	22223	4.976	2.745
0-5	53259	3.672	2.490

The sample mean and standard deviations for each of the subsets of cHaines data conditional on FFDI are shown in Table 2. From this table we can now easily calculate a standard deviation value for any given pair of FFDI (F) and cHaines (ch) values, using the formula

$$SD = \frac{ch - \mu(F)}{\sigma(F)}$$

where $\mu(F)$ and $\sigma(F)$ are determined by the FFDI range in Table 2. Using number of standard deviations as a measure of the significance of the cHaines value has the benefit of being more independent of the FFDI, by taking account of the fact that the spread of the distribution is also conditional on the FFDI value. This relationship could then be used to produce anomaly maps of cHaines in units of numbers of standard deviations, based on the Australian Digital Forecast Database

grids. An example forecast of cHaines anomaly from the 8 January 2013 is shown in Figure 4. In this case there is a very broad area of cHaines index greater than 11 across the south of the state, however for much of this area the value is less than 1.0 standard deviations (s.d.) from the mean, and thus is close to what you would expect for the forecast FFDI on the day. The exceptions to this are the far southeast corner and the mid north coast, where the forecast cHaines is between 1 and 2 s.d. from the mean. The Yarrabin fire, to the east of Cooma, took a major run during the 8th, becoming one of the largest going fires in the state. Figure 5 shows another forecast map, from the 13 January 2013, a day on which a major fire caused major property damage in the rural areas to the west of Coonabarabran.

The behaviour and rate of spread of this fire were increased by fire-atmosphere interactions, including the formation of pyro-cumulonimbus. The cHaines forecast on the day showed an area of cHaines index 12-13 in the northwest of the state, however the cHaines anomaly map further highlights this area as being 1 to 2 s.d. above what would be expected from the forecast FFDI values. These maps are produced here as a proof of concept. Further work could be carried out to look at detailed case studies of events in which significant fire-atmosphere interactions are observed.

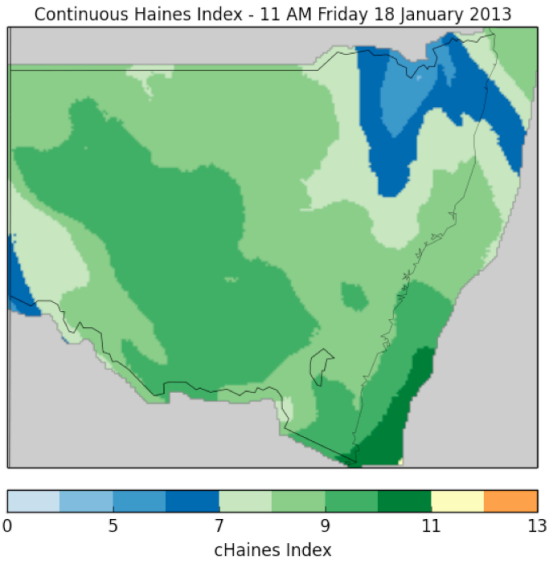

Figure 4a Forecast of cHaines index across NSW for 2pm (local time) on 8 January 2013.

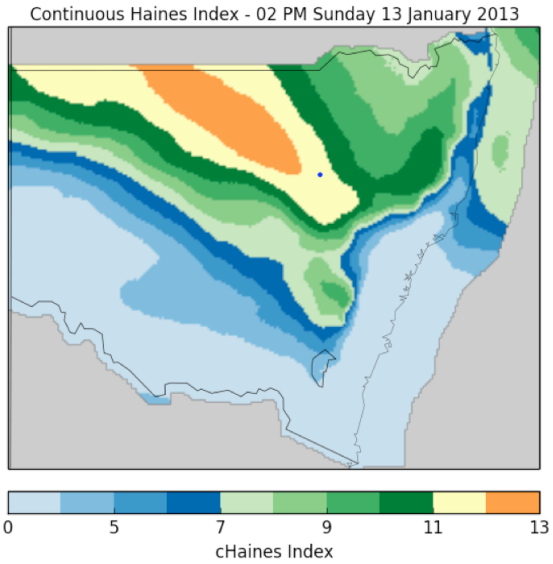

Figure 5a Forecast of cHaines index across NSW for 2pm (local time) on 13 January 2013.

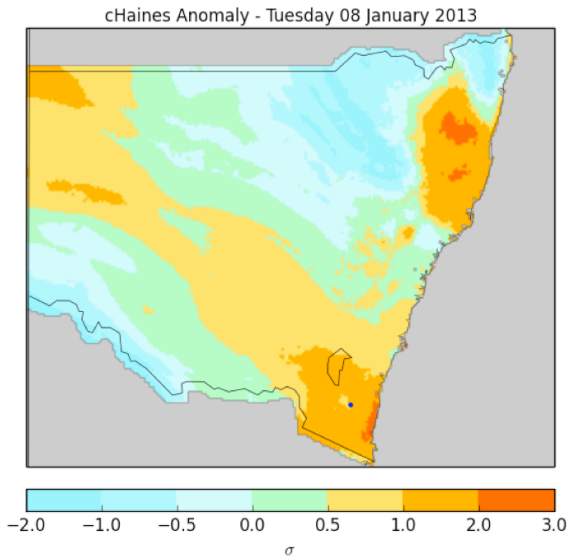

Figure 4b Forecast of 2pm (local time) cHaines index anomaly conditional on the 3pm (local time) FFDI forecast, for 8 January 2013. Fire location marked with blue dot.

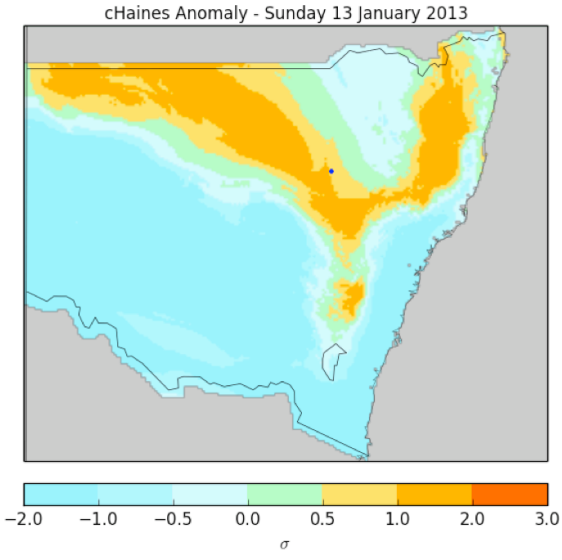

Figure 5b Forecast of 2pm (local time) cHaines index anomaly conditional on the 3pm (local time) FFDI forecast, for 13 January 2013. Fire location marked with blue dot.

Conclusions

An observational data set composed of high quality FFDI values coupled with cHaines index values was compiled to investigate the relationship between the two indices. It was found that there was a positive correlation between FFDI and cHaines, but that the amount of correlation varied seasonally and also from station to station. The distribution of the composite data set containing paired cHaines and FFDI values was taken as representative of the overall relationship between FFDI and the cHaines index.

Using this relationship, a method for producing maps of cHaines anomaly, conditional on the forecast FFDI value, was developed. These maps could be used to assist forecasters in recognising when the cHaines value for a given area is significantly higher than would be expected as 'normal' from the forecast of FFDI. This would not be a tool to assess overall risk of instability related fire behavior, as close to average cHaines on a high end FFDI day is still clearly a major risk. Rather, this tool could be used to try and identify areas where the instability driven fire behavior could be worse than would be expected from surface conditions, and hence could have the potential to catch fire managers by surprise. Also, as with any index, it should be used only as a prompt to perform a more detailed analysis of the atmospheric environment.

Future work could involve some more in depth case studies of significant blow-up fire events, as well as investigating whether any good quality data sets of fire behaviour are available to do a more systematic assessment of the usefulness of a cHaines anomaly. The data set of observed cHaines index values produced could also be used to investigate inter-annual variations in the index, such as those identified in Yu et al. 2013.

Acknowledgements

The author would like to thank the reviewers of this paper for their comments and suggestions.

References

Bally, J 1995, 'The Haines Index as a predictor of fire activity in Tasmania', *Proceedings of Bushfire '95, Australian Bushfire Conference,* Hobart, Tasmania.

Keetch, JJ & Byram, GM 1968, 'A drought index for forest fire control', *Research Paper SE-38*, Asheville, North Carolina: USDA Forest Service.

Long, M 2006, 'A climatology of extreme fire weather days in Victoria', *Aust. Meteorol. Mag.,* vol. 55, pp. 3-18.

Lucas, C 2010, 'On developing a historical fire weather data-set for Australia', *Aust. Meteorol. Mag.,* vol. 60, pp. 1-14.

McArthur, AG 1967, 'Fire behaviour in eucalypt forests', Leaflet 107. Commonwealth of Australia Forestry and Timber Bureau.

McCaw, L, Marchetti, P, Elliot, G & Reader, G 2007, 'Bushfire weather climatology of the Haines Index in south-west WA', *Aust. Meteorol. Mag.*, vol. 56, pp. 75-80.

Mills, GA & McCaw, L 2010, 'Atmospheric Stability Environments and Fire Weather in Australia - extending the Haines Index', Tech. Rep. 20. The Centre for Australian Weather and Climate Research.

Yu, L, Zhong, S, Bian, X, Heilman, WE & Charney, JJ 2013, 'The interannual variability of the Haines Index over North America', *J. Appl. Meteorol. Clim.,* vol. 52, no. 11, pp. 2396-2409.

Abrupt increases in fire danger: a synoptic climatology

Paul Fox-Hughes
Severe Weather Section, Bureau of Meteorology, Hobart, and
Antarctic Climate and Ecosystems Co-operative Research Centre
p.fox-hughes@bom.gov.au

Introduction

There is extensive documentation of stratospheric intrusions (SI) triggering development of severe weather. Browning and Golding (1995) discuss the development of a tornadic squall line resulting from the descent of a filament of high potential vorticity (PV) air over the warm conveyor belt associated with a cold front crossing the United Kingdom. Goering et al. (2001) document damaging winds occurring with an SI over the southwest of the United States, while Fox-Hughes (2009) documents the occurrence of pulses of heavy rainfall over Tasmania, accompanying the passage of successive 'dry slots' in water vapour (WV) imagery associated with SI. In particular, a number of researchers have documented cases where intrusions of stratospheric air have caused rapid escalation of the activity of wildfires: (Zimet et al. 2007; Kaplan et al. 2008; Mills 2008a; Fox-Hughes 2012). Mills (2008b) established a climatology of such events, suggesting criteria by which they might be identified, and identifying satellite water vapour features with the potential to alert weather forecasters to their presence.

In this paper, examples of abrupt increases in fire danger, "spikes", are obtained from a database of fire weather observations for a site in southeast Tasmania, an area subject to outbreaks of dangerous fire weather (Fox-Hughes 2012), and occasional devastating wildfires (Foley 1947; Bond et al. 1967), most recently on 4 January 2013. Examples are also identified of days subject to elevated fire danger, but not the abrupt spikes characteristic of the first collection of events. Composites of atmospheric parameters on both sets of days indicate differences in the meteorology associated with each type of event, and are suggestive that the two sets of events are broadly similar to the two types of event described in Fox-Hughes (2012). In that study, an event with a distinct spike was associated with a clear stratospheric intrusion, while another dangerous event, lacking a spike, showed no evidence of an SI reaching into the boundary layer. Finally, a set of non-fire weather days was identified, for comparison with the two fire-weather sets. Clear differences are evident between the synoptic types

associated with the spike and non-spike composite events. Identification of a synoptic type associated with stratospheric intrusions is of innate scientific interest, but is of interest particularly to operational meteorologists and to fire managers.

Methods

Half-hourly weather observations at Hobart Airport were used to derive McArthur Forest Fire Danger Index (FFDI) values (McArthur 1967) during the period 1990-2010. More details of the derivation of FFDI values are contained in Fox-Hughes (2011). North to northwesterly airstreams are associated with the most significant fire weather events in Tasmania, and Hobart Airport is well-placed to experience a well-mixed boundary layer in these events. A combination of thermal mixing, due to the site's position on the warmer leeside of the Tasmanian landmass, and mechanical turbulence, due to the presence of substantial orography upwind of Hobart, ensures that the boundary layer extends to at least 2,000 m on such days.

Days with maximum FFDI values exceeding 24 ("Very High" fire danger) were selected, resulting in some 230 cases. Within that subset, the mean and standard deviation of the FFDI were calculated for those values exceeding 24, and the number of standard deviations (SD) of the maximum FFDI from the mean was calculated. Days on which the maximum FFDI was more than 2 SD from the mean were classed as fire weather "spike" days. This process identified days on which fire weather conditions were already quite dangerous but conditions abruptly became substantially worse for a period. Some 37 days were classed as "spike" days. Notably, peak FFDI on approximately half of the "spike" days occurred at a non-routine time, suggesting that the wind averaging period used to calculate the mean wind underlying the FFDI was less than ten minutes. Thus, the FFDI may be higher in these cases than that calculated from a standard ten minute-averaged wind. It remains the case, however, that the wind was elevated above the "background" value during these periods and the fire danger also abruptly increased. Other events were selected where the maximum FFDI exceeded the mean of "Very High" observations by less than 1.5 SD. In this case, however, the maximum FFDI

was required to be at least 38. Some 25 days satisfied these criteria. Finally, "non-events" – days on which neither set of criteria were met – were also selected. The non-events were selected from the 15th day of October through March for each year between 1990 and 2009. This set was much larger than required, so every fifth day was chosen, resulting in a subset of 24 days. Composites of atmospheric parameters were plotted for each type of event from NCEP/NCAR reanalysis data (Kalnay et al. 1996), using the facilities of the Physical Sciences Division of NOAA's Earth System Research Laboratory (PSD/ESRL).

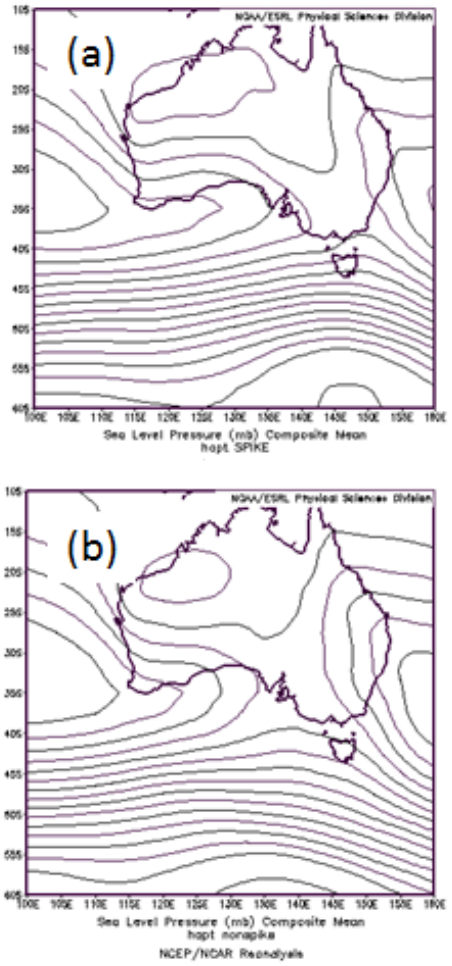

Figure 1 Composite MSLP plots of (a) spike and (b) non-spike fire weather events from daily NCEP/NCAR reanalyses.

Results and Discussion

Daily composite MSLP images of spike and non-spike events are presented in Figure 1. In both composites, troughs are located close to Tasmania, with low pressure centres well south of the island. The troughs extend from south of Australia through to heat lows over the northwest of the continent. High pressure centres are located in the Tasman Sea and in the Indian Ocean to the west of the Australian continent. Both plots correspond well to the observations noted above relating days of elevated fire danger to approaching frontal systems. The most pronounced difference between the two plots is that the trough axis is more advanced in the spike composite than in the non-spike case, with the eastern high centre located correspondingly further east. A similar, though more pronounced, difference in the position of the respective composite troughs is evident in a comparison of 250 hPa vector wind plots, shown in Figure 2. Troughs are evident to the south of the Australian continent in both composite plots, and a wind maximum lies on the eastern flank of the trough, to the south of Tasmania.

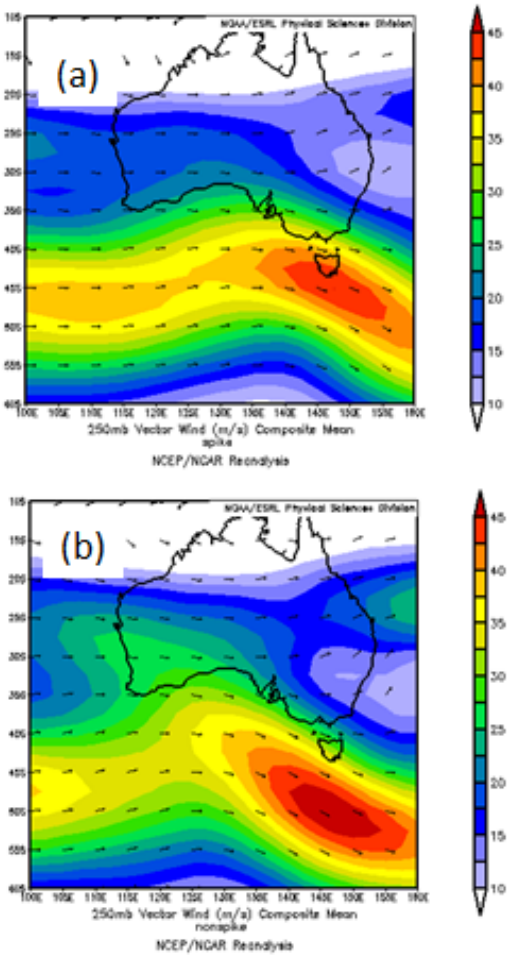

Figure 2 Composite plots of 250 hPa vector wind for (a) spike and (b) non-spike fire weather events from daily NCEP/NCAR reanalyses.

However, the spike composite trough is located between 135-140°E at 40°S while the non-spike trough is well west, between 125-130°E at the same latitude. While the non-spike wind maximum is stronger than that of the spike plot, with winds in the core in excess of 45 ms^{-1}, the core axis lies near 50°S. The spike wind maximum is weaker, but its axis runs over the south coast of Tasmania. Further, the composite jet at 250 hPa is cyclonically curved for the spike events but anticyclonically curved in

the non-spike case. The entrance region of the cyclonically curved jet near Tasmania is a favourable location for convergence, and hence descent, while the more distant entrance region of the anticyclonically curved jet is characterised by (weaker) upward air movement (Moore and Van Knowe 1992).

It is worth investigating the evolution of the spike-event trough in a little more depth. A sequence of six-hour composite reanalysis plots at 1800, 0000 and 0600 UTC (corresponding to early morning, late morning and mid to late afternoon local time) on the days of spike events is displayed in Figure 3. They show a progressive degree of cyclonicity in the jet as it advances eastward towards Tasmania. This results in an increase in asymmetry of the trough at higher latitudes (shown by the thick dashed lines), to assume a "negative" tilt (i.e. longitude increases with proximity to the equator), suggesting rapid system development and potential for severe weather due to increasing vertical circulation (Bluestein 1993, p.118). Atallah et al. (2007) note a similar structure in the extratropical transition of tropical cyclones, while Speer and Leslie (2000) have documented a number of negatively tilted troughs associated with heavy rainfall events. Macdonald (1976) and Glickman et al. (1977) describe such troughs in relation to the development of convective outbreaks. One such trough was observed, in particular, during the "spike" event documented in Fox-Hughes (2012).

Composite vertical cross-sections of relative humidity along 43°S between 100 and 160°E are displayed in Figure 4, for (a) spike, (b) non-spike and (c) non-event days from daily NCEP/NCAR reanalyses. Both spike and non-spike fire weather days suggest a well-mixed boundary layer in the vicinity of Tasmania, as expected during such events and in contrast to the non-event composite, where the boundary layer over Tasmania is indistinguishable from that over waters to the east or west. The non-spike composite has a well-defined area of relative humidity below 40% extending to below 500 hPa to the west of Tasmania, indicating the position of the upper level trough and lower tropopause. In addition, immediately east of Tasmanian longitudes, centred near 155°E at about 850 hPa is a region of drier air between 40 and 45% relative humidity. Layers of dry air immediately above a pre-existing inversion typify the atmospheric profiles of days of dangerous fire weather in southeastern Australia. In these daily reanalysis composites, it is interesting that dry air associated with the upper trough in the spike composite (Figure 4 (a)) does not extend as strongly into the troposphere as occurs in the non-spike case. However, the trough (represented by the dry air) is centred closer to Tasmania, and there is a distinct (although weak) axis of lower relative humidity extending from the upper dry air reservoir to the well-mixed boundary layer. In the corresponding non-spike composite, while there is similar, indeed better defined, axis extending to the top of the boundary layer to the west of Tasmanian longitudes, it is disconnected from the region of the well mixed boundary layer by a region of more moist air. These differences correspond remarkably well with the patterns of moist and dry air noted in the fire weather events examined in Fox-Hughes (2012), in which one event was identified as a spike and the other as a non-spike front.

Conclusions

The differences noted above between spike and non-spike events suggest that vertical circulations associated with jet streams are more able to play a role in the evolution of spike events than in non-spike events. In spike events, the proximity of the trough axis to Tasmania, and consequent location of the entrance region of a cyclonic jet core over southern Tasmania, is a favourable position for it to affect atmospheric conditions over the island. The more distant non-spike jet core could, potentially, influence Tasmanian weather, but the likelihood of it so doing is smaller. On the basis of the above synoptic analysis then, spike events are more likely in general to be capable of transporting air from the upper troposphere to the surface, via the ageostrophic circulations associated with jet stream cores coupled with turbulent mixing in a deep convective boundary layer (as described in e.g. Kaplan et al. (2008)). Further, the negative tilt of the upper level trough in spike events tends to more tightly focus vertical motions immediately downstream of the trough (i.e. over Tasmania) than is the case in positively or neutrally tilted troughs associated with non-spike events, at a time of the day (mid to late afternoon) when the mixed layer is likely to be deepest and most able to couple to overlaying layers of the troposphere.

The differences evident between the synoptic patterns associated with fire weather events characterised by abrupt "spikes" in fire danger at Hobart Airport and those events lacking such features can potentially be used by meteorologists to assist in the forecasting of fire danger "spikes" well in advance of the commencement of the events. It will be necessary to ensure that these results can be generalised to other locations, of course. If that is possible, the technique is likely to be a useful tool to highlight situations conducive to the occurrence of a dangerous phenomenon.

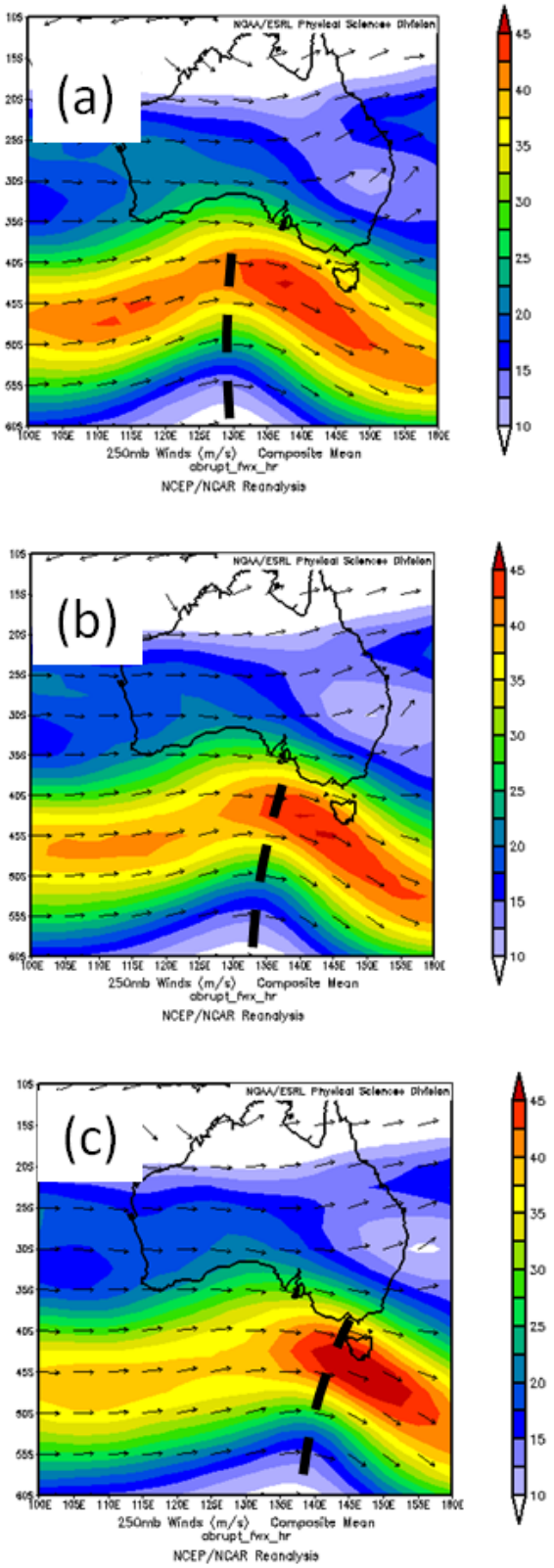

Figure 3 Composite plots at successive six hour intervals of NCEP/NCAR reanalysis 250 hPa vector wind (a) 1800, (b) 0000 and (c) 0600 UTC.

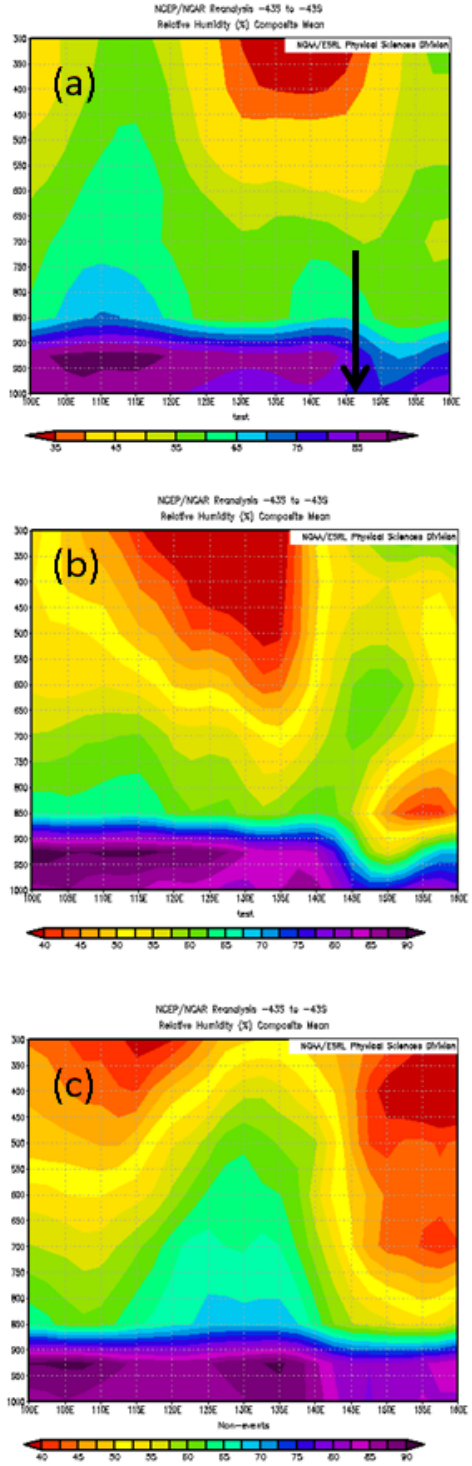

Figure 4 Composite cross-sections of NCEP/NCAR relative humidity through 43°S, from 100 to 160°E for (a) spike, (b) non-spike and (c) non event days. Arrow in (a) indicates location of Hobart Airport.

Comments from the reviewers and associate editor helped improve the clarity and focus of this paper.

Acknowledgements

Reanalysis plots provided by the NOAA/ESRL Physical Sciences Division, Boulder Colorado from their Web site at http://www.esrl.noaa.gov/psd/.

References

Atallah, E, Bosart, LF and Aiyyer, AR (2007) Precipitation Distribution Associated with Landfalling Tropical Cyclones over the Eastern United States. *Monthly Weather*

Review **135**(6), 2185-2206.

Bluestein, HB (1993) Synoptic-Dynamic Meteorology in Midlatitudes Vol. II, Observations and Theory of Weather Systems. Oxford University Press, New York.

Bond, HG, MacKinnon, K and Noar, PF (1967) Report on the meteorological aspects of the catastrophic bushfires in southeastern Tasmania on 7 February 1967, Bureau of Meteorology. (Australia)

Browning, KA and Golding, BW (1995) Mesoscale Aspects of a Dry Intrusion within a Vigorous Cyclone. *Quarterly Journal of the Royal Meteorological Society* **121**(523), 463-493.

Foley, JC (1947) A study of meteorological conditions associated with bush and grass fires and fire protection strategy in Australia. 38, Bureau of Meteorology.
Fox-Hughes, P (2009) A heavy rainfall event in northern Tasmania during 27 to 30 January 2004. *Australian Meteorological and Oceanographic Journal* **58**(3), 151.

Fox-Hughes, P (2011) Impact of More Frequent Observations on the Understanding of Tasmanian Fire Danger. *Journal of Applied Meteorology and Climatology* **50**(8), 1617-1626.

Fox-Hughes, P (2012) Springtime Fire Weather in Tasmania, Australia: Two Case Studies. *Weather and Forecasting* **27**(2), 379-395.

Glickman, T, Sanders, F and MacDonald, N (1977) New findings on the apparent relationship between convective activity and the shape of 500 mb troughs. *Monthly Weather Review* **105**, 1060.

Goering, MA, Gallus, WA, Olsen, MA and Stanford, JL (2001) Role of stratospheric air in a severe weather event: Analysis of potential vorticity and total ozone. *Journal of Geophysical Research-Atmospheres* **106**(D11), 11813-11823.

Kalnay, E et al. (1996) The NCEP/NCAR 40-year reanalysis project. *Bulletin of the American Meteorological Society* **77**(3), 437-471.

Kaplan, ML, Huang, C, Lin, YL and Charney, JJ (2008) The development of extremely dry surface air due to vertical exchanges under the exit region of a jet streak. *Meteorology and Atmospheric Physics* **102**(1-2), 63-85.

Macdonald, NJ (1976) On the apparent relationship between convective activity and the shape of 500 mb troughs. *Monthly Weather Review* **104**, 1618-1622.

McArthur, AG (1967) Fire Behaviour in Eucalypt forests, Forestry and Timber Bureau. (Canberra, Australia)

Mills, GA (2008a) Abrupt surface drying and fire weather Part 1: overview and case study of the South Australian fires of 11 January 2005. *Australian Meteorological Magazine* **57**, 299-309.

Mills, GA (2008b) Abrupt surface drying and fire weather Part 2: a preliminary synoptic climatology in the forested areas of southern Australia. *Australian Meteorological Magazine* **57**, 311-328.

Moore, JT and VanKnowe, GE (1992) The Effect of Jet-Streak Curvature on Kinematic Fields. *Monthly Weather Review* **120**, 2429-2441.

Speer, MS and Leslie, LM (2000) A comparison of five flood rain events over the New South Wales north coast and a case study. *International Journal of Climatology* **20**(5), 543-563.

Zimet, T, Martin, JE and Potter, BE (2007) The influence of an upper-level frontal zone on the Mack Lake Wildfire environment. *Meteorological Applications* **14**(2), 131-147.

Modelling the fire weather of the Dunalley, Tasmania fire of January 2013: an ACCESS case study

R. J. B. Fawcett[A,B], M. Webb[C] , W. Thurston[A,B], J. D. Kepert[A,B] and K. J. Tory[A,B]
[A]The Centre for Australian Weather and Climate Research, Docklands, Victoria
[B]Bushfire Cooperative Research Centre, Melbourne, Victoria
[C]Tasmania/Antarctica Regional Office,
Bureau of Meteorology, Hobart, Tasmania
r.fawcett@bom.gov.au

Introduction

On 4 January 2013, a day of significant fire activity in southeast Tasmania, a familiar set of Australian summer meteorological ingredients, (i) an approaching cold front west of Tasmania, and (ii) an anticyclone in the Tasman Sea between New South Wales and New Zealand (Figure 1), brought strong hot northerly to northwesterly winds over southeast Australia and Tasmania in particular. These conditions occurred during a significant national heatwave that contributed to January 2013 being the hottest month on record for Australia (BoM 2013a).

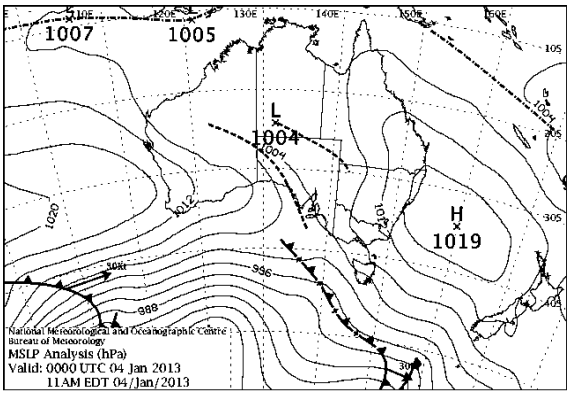

Figure 1 Mean sea-level pressure analysis for 0000 UTC (1100 EDT) on 4 January. Pressures are in hPa. Image courtesy of the National Meteorological and Oceanographic Centre.

On the previous day (3 January), Forest Fire Danger Ratings (FFDRs) reached the "very high" range over much of the eastern half of Tasmania and the "severe" range in the southeast, as temperatures reached the mid 30s (°C) and gusty westerly to northwesterly winds developed. These weather conditions were coincident with the spreading of two fires, the Lake Repulse fire and the Forcett fire, both of which started that day (BoM 2013b). The 4th of January saw numerous high temperature records set in southern Tasmania (Figure 2), most notably its capital city Hobart, whose maximum of 41.8 °C was the highest in 120 years of records there, the highest on record anywhere in southern Tasmania, and the second-highest for the State as a whole (BoM 2013a). On that day, thousands of people, including summer holiday makers, were stranded on the Tasman Peninsula (TP) as bushfires cut off road access, with many evacuated by water back to Hobart. The fires destroyed many properties in Tasmania, news media reporting at least one hundred, with Dunalley particularly badly hit.

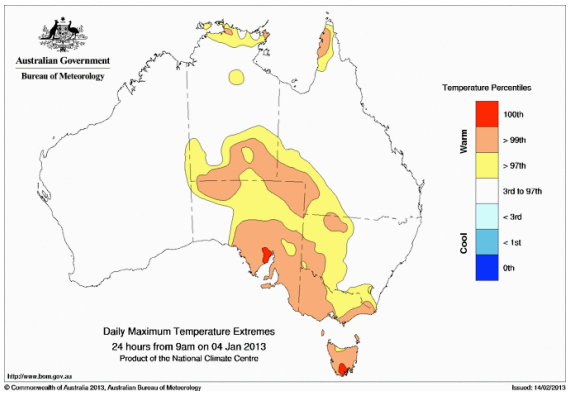

Figure 2 Percentiles of daily maximum temperature for 4 January 2013. The figure is calculated using all the January daily maximum temperature analyses of Jones et al. (2009) between 1 January 1911 and 4 January 2013. Highest-on-record January daily maximum temperatures were seen in the analyses in southeast Tasmania and at the top of Spencer Gulf in South Australia.

Two weather stations in southeast Tasmania (Hobart and Campania) measured "catastrophic" FFDRs at routine observation times on the hour. Over periods ranging from one minute to one hour, five weather stations registered "catastrophic" FFDRs, these being Hobart, Campania, Hobart Airport, Bushy Park and Dunalley (all near to, but not on, the TP). [In Tasmania, the FFDR is associated with a Forest Fire Danger Index (FFDI) being in a particular range of values (BoM 2013b), it being the FFDI which is actually forecast and observed.] At Dunalley, as fire swept through the township, radiant heat from the fire corrupted the air temperature readings at the Bureau of Meteorology's (hereafter, the Bureau) automatic weather station. In fact, the fire came close enough to the Stevenson Screen housing the thermometer to blister the white paint on the Screen (BoM

2013b). We present the results of high-resolution (0.012°-grid-spacing) and very-high-resolution (0.004°-grid-spacing) simulations of the fire weather over southeast Tasmania around the time of the start of the Dunalley fire. The simulations were performed using the Australian Community Climate and Earth-System Simulator (ACCESS), and involve a cascade of nested model runs starting from a global model run initialised with an initial condition prepared by the Bureau's National Meteorological and Oceanographic Centre. Our analysis will focus on how well the simulations capture the meteorological factors that promote extreme fire behaviour. The ACCESS model is used at the Bureau for operational numerical weather prediction, but is used here in research mode at much finer resolutions than current operational ones.

The 0.004°-grid-spacing simulations show notional instantaneous FFDI (a Drought Factor of 10 is assumed) values peaking in the FFDR "catastrophic" range (> 100) across the TP, comparable to the observed "catastrophic" values at the non-TP sites mentioned above, but the 0.012°-grid-spacing simulations show less intense values, mostly peaking within the "severe" range (50-74) with a few grid cells peaking in the "extreme" (75-99) range. [Operational FFDR forecasts for 4 January 2013 for the various Tasmanian forecast districts ranged from "very high" to "extreme", without reaching the highest "catastrophic" category (BoM 2013b), although it should be noted that a particular *district forecast* FFDR does not preclude individual grid points within the district from having a higher forecast FFDR.] Afternoon maximum temperatures and wind directions are generally well modelled, although some of the fine-scale local wind changes were not captured in the simulations. The passage of the primary wind change (from northerly to southerly) in the simulations shows a complicated interaction with the topography and coastline of southeast Tasmania. Wind changes such as this one can have a significant (and dangerous) impact on the behaviour of bushfires in southeast Australia, and their prediction forms an important component of fire weather prediction.

This work arose through a project funded by the Bushfire Cooperative Research Centre, to produce very-high-resolution meteorological simulations for significant recent fire events. The intent is for a better understanding of the meteorology of those events and the use of the simulation results in fire spread and fire impact modelling.

Modelling

The high-resolution and very-high-resolution numerical weather prediction (NWP) modelling described in this paper was performed using ACCESS, and in particular the United Kingdom Meteorological Office's (UK Met Office) atmospheric model which comprises the atmospheric component of ACCESS. In order to simulate the weather conditions on the 4th of January, a sequenced of nested model runs was employed, starting with a global model run and progressively nesting down to a region of approximately 3°×3° (330 km × 240 km) for the finest-resolution simulation. In these simulations, meteorological information flows from the coarser-resolution simulation to the finer-resolution simulation, but not in the other direction. Further, the fires are not represented in the simulations.

In total, there were five levels to the nesting process. The second-level domain (0.11° grid spacing, i.e., ≈ 12 km) extends well to the west of Australia, while maintaining a 20° buffer to the south, 35° to the east and 35° to the north. The third level (0.036° grid spacing, i.e. ≈ 4 km) covers all of Tasmania and surrounding waters, while the fourth level (0.012° grid spacing, i.e. ≈ 1.3 km) covers the main island of Tasmania and the fifth level (0.004° grid spacing, i.e., ≈ 440 m) southeast Tasmania. Domain boundaries have been placed, where possible, to avoid regions of significant topography (Figure 3).

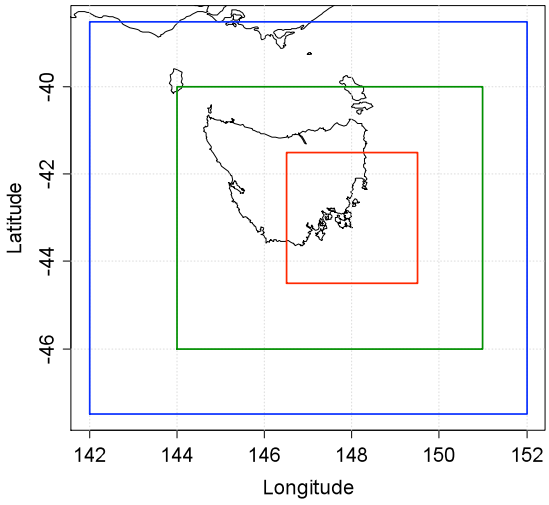

Figure 3 Model domains for the 0.036°-grid-spacing (blue box), 0.012° grid spacing (green box) and 0.004° grid-spacing (red box) simulations of the meteorology on 4 January 2013.

All five levels of nesting use 50 vertical levels in the atmospheric model, with the lowest model level being approximately 10 m above the surface for some meteorological variables (e.g., the u and v components of the horizontal wind) and approximately 20 m above the surface for other variables (e.g., potential temperature and the vertical component of the velocity). The highest

model level is around 60 km above mean sea level.

The simulations use global initial conditions obtained from the Bureau of Meteorology. Three initialisation times were explored; 0300 UTC, 0900 UTC and 1500 UTC on 3 January 2013. All simulations ran for 50 hours of model time, so (for example) those initialised at 0300 UTC cover the period from 0300 UTC on 3 January to 0500 UTC on 5 January. Results presented in this paper pertain to the 0300 UTC initialisation simulations, unless otherwise stated. All five levels of nesting were initialised from the same base time: accordingly little attention was paid in the finer-resolution simulations to the first 12 hours of the model integration. This is because at the start of the integration, each nesting level is essentially presenting just the detail which is present in the global analysis: it takes some time for the model atmosphere to interact with the high-resolution model topography to develop the fine-scale local details. Instantaneous outputs for the model surface fields (e.g., those used in Figures 4, 5 and 6) were archived at five-minute intervals, while those for the model levels describing the atmosphere above the surface were archived at 15-minute intervals.

Model validation

For simulations of recent events such as this one, the model results can be validated against a range of meteorological data obtained from sources such as automatic weather stations (AWSs), radiosondes (balloon flights), weather watch radars and meteorological satellites. In validating the simulations against AWS data, the nearest model grid point to the AWS location was generally chosen. The exceptions to this rule were in the southeast of Tasmania, particularly around the TP where the coastline is quite complicated and consequently the nearest model grid point is often a *marine* grid point. For these sites, a representative *land* grid point in the model near to the AWS was chosen. The chosen point usually depends on the grid spacing.

Figure 4 shows a comparison between observational data from Hobart Airport AWS and a nearby model land point in the 0.004°-grid-spacing simulation initialised at 0300 UTC on 3 January 2013. The afternoon maximum temperature on 4 January 2013 is well simulated, although the overnight cooling is underestimated with the morning minimum temperature on the 4th being somewhat in error. The minimum temperature on the 5th is rather better hindcast. The change in the wind direction from northerly to southerly just after midnight EDT (Eastern Daylight Time = UTC + 11 hours) on the 5th is around 75 minutes early in this simulation (although around 30 minutes early in the parallel simulation initialised at 0900 UTC on 3 January 2013).

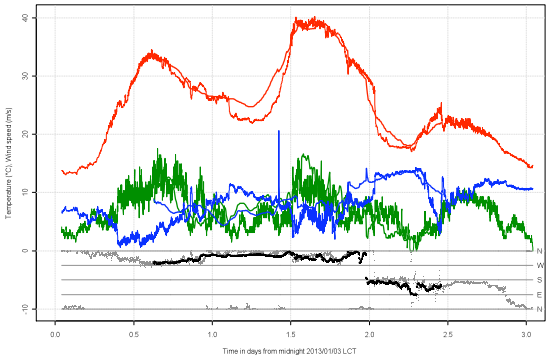

Figure 4 Comparison between the 0.004°-grid-spacing simulation initialised at 0300 UTC on 3 January 2013 (thick lines, black dots, five-minute-interval data) and AWS observations (thin lines, grey dots, one-minute-interval data) for Hobart Airport (094008). Air temperature (in °C, red lines), dewpoint temperature (in °C, blue lines), 10 metre wind speed (in m s^{-1}, green lines) and direction (dots). The horizontal axis shows time in days from midnight EDT on 3 January 2013.

Wind directions are well simulated, although wind speeds and dewpoint temperatures are not quite as good. A general tendency in high-resolution simulations of this type has been noted for peak 10-metre wind speeds to be underestimated in the model, although in Figure 4, the opposite is the case. There is a capability in the high-resolution modelling to catch quite subtle features in the atmospheric flow. For example, there is a drift in the observed wind direction in the evening of the 4th in Figure 4 from northerly around to westerly (and back again), which although not particularly well caught in the 0300 UTC initialisation shown in Figure 4 is well caught in the two later initialisations of 0900 UTC and 1500 UTC (not shown). An additional example is shown in Figure 5 for Maria Island north of the TP. [The coastline of Maria Island is shown on the right-hand-side of Figure 8 below; see also the inset in Figure 6.] Here the predicted timing of the major wind change is almost exact, but somewhat surprisingly the post-change wind direction is *easterly* (rather than southerly or southwesterly) and this is captured in the modelling (see also Figure 6, which indicates just how small was the region of easterly winds). Here though, the wind speed is generally underestimated.

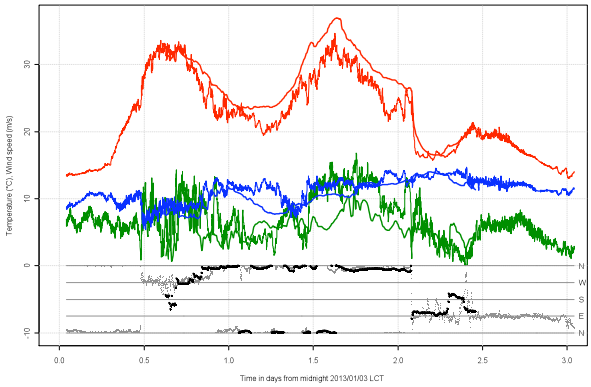

Figure 5 As for Figure 4, but for Maria Island (092124).

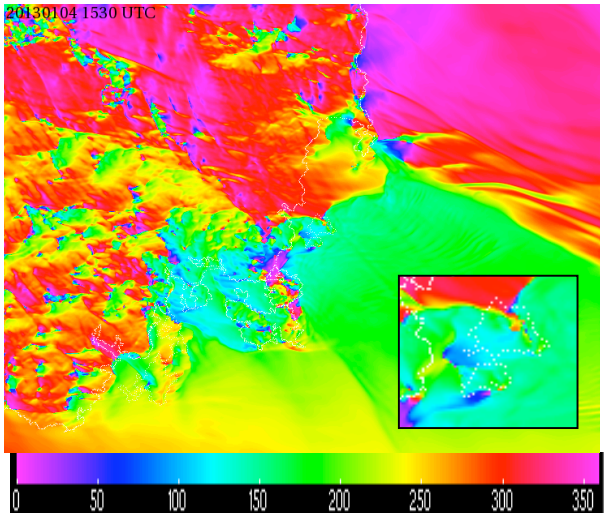

Figure 6 Direction of the 10-metre wind at 1530 UTC on 4 January (0230 EDT on 5 January) in the 0.004°-grid-spacing simulation, around the time the wind change is passing over the northern end of Maria Island. The wind has swung easterly (blue shades) over a small patch in the vicinity of the AWS at Point Lesueur on Maria Island (see also the inset which expands the region surrounding Maria Island), which sits within a larger region of more southerly flow (green shades).

Figure 7 shows a validation of the model's representation of the vertical structure of the atmosphere, using the 2300 UTC 3 January 2013 radiosonde balloon flight from Hobart Airport. This shows the vertical structure of the atmosphere on the morning of the fires. The model's representation of the air temperature, dewpoint temperature, wind speed (all shown in Figure 7) and direction (not shown) is in good agreement with the observations, taking into consideration that the comparison is not precisely "like with like", for a range of reasons.

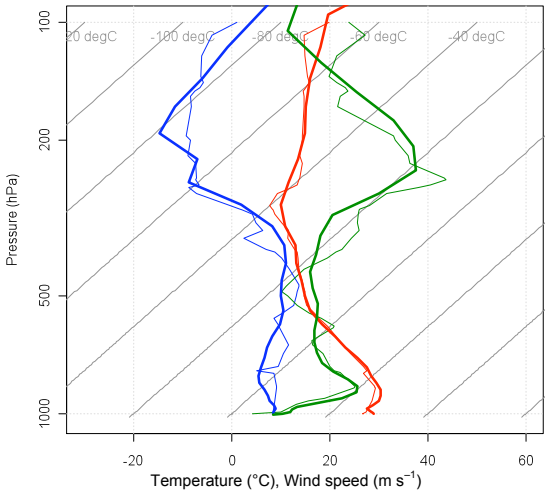

Figure 7 Comparison between the 0.036°-grid-spacing simulation initialised at 0300 UTC on 3 January 2012 (thick lines) and radiosonde observational data (thin lines) for Hobart Airport at 2300 UTC on 3 January 2013 (1000 EDT on 4 January). Air temperature (in °C, red lines), dewpoint temperature (in °C, blue lines), both skewed, and horizontal wind speed (in m s^{-1}, green lines) are shown. The model grid point nearest to the nominal release point of the balloon has been chosen for comparison.

Modelled FFDI

Figure 8 shows the modelled notional instantaneous FFDI Mark 5 (Noble et al. 1980), calculated assuming a maximal drought factor of 10, for two time steps in the 0.004°-grid-spacing simulation initialised at 0300 UTC on 3 January 2013. The modelled FFDI exceeds 150 on some of the more elevated parts of the plotted region and is widely in the "extreme" (FFDI: 75 to 100) to "catastrophic" (FFDI: > 100) ranges. Peak values near Dunalley exceed 100. Peak values on the TP likewise exceed 100 in small areas in this very-high-resolution simulation. It is noted that values over the TP in the 0.012°-grid-spacing simulation are not as high, as reported in the Introduction.

The FFDI shows a strongly banded pattern, with wider regions of elevated FFDI interspersed with narrower regions of lower FFDI. Analogous bands are present in the 10-metre wind field, a component in the FFDI calculation, and appear to be tied to the orography rather than being free atmospheric oscillations (such as boundary-layer rolls). The orientation of these bands changes with the orientation of the broader-scale flow, resulting in local fluctuations in FFDI value as the bands pass across particular locations. These bands appear to be similar to the orographic wakes reviewed by Belcher and Hunt (1998, section 6).

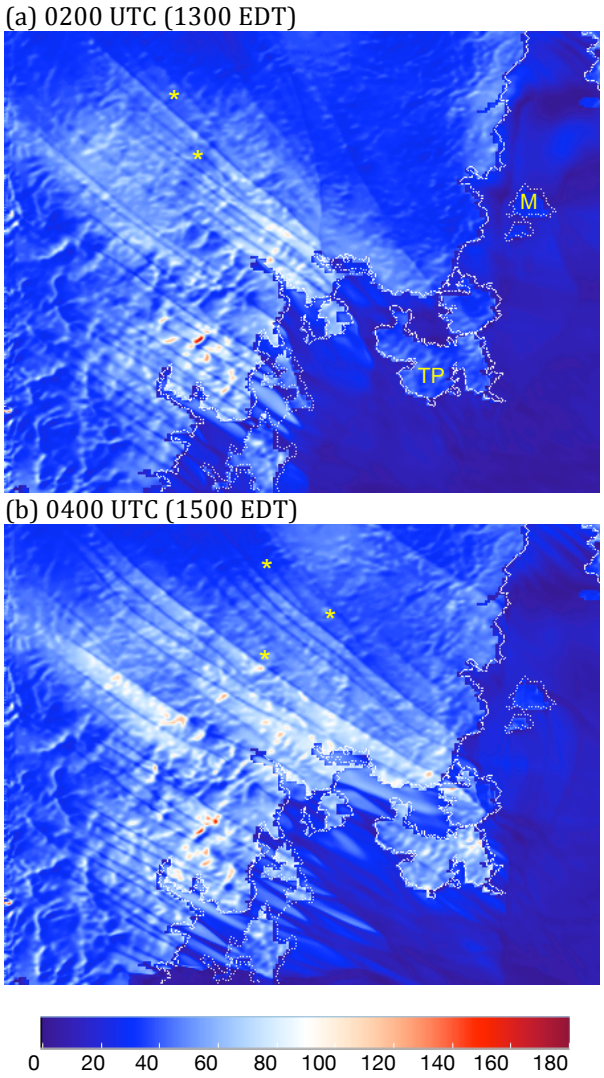

Figure 8 Notional instantaneous FFDI in the vicinity of the TP at (a) 0200 UTC and (b) 0400 UTC on 4 January 2013. Figures calculated from the 0.004°-grid-spacing simulation, initialised at 0300 UTC on 3 January 2013. A drought factor of +10 is assumed in the calculation. The asterisks denote areas where bands of low FFDI converge. Maria Island is marked by an "M". The Tasman Peninsula (TP) is also indicated.

Discussion and Conclusions

The atmospheric flow modelled in the higher-resolution simulations around the southeast of Tasmania is quite complicated. This appears to be due to both the orography (e.g., the inland mountains) and the complicated nature of the coastline, which itself complicates the modelling process because a certain amount of "simplification" of the orography and coastline is required to enable the NWP to function. Figure 8 (both panels) for example shows converging bands of low FFDI where the downstream flow from two different parts of the orography merge (indicated by asterisks in the Figure). Arguably of more importance is the very detailed way in which the synoptic wind change wraps around the southeast coast of the State. This is illustrated in Figure 9, which shows isochrones of the 240° (approximately southwesterly) wind direction at four times in the evening on 4 January 2013. Out over the ocean, the isochrones can be traced with some degree of clarity, although there is much in the way of interesting fine-scale structure to the wind change, but around the coastline, there is considerable complexity. Such complexity represents a significant forecasting challenge, both in the assimilation of the meteorological detail (and its implications for any active fires) by the professional weather forecaster in a Regional Forecasting Centre, and the communication of the salient features of the meteorology to firefighters trying to fight such fires.

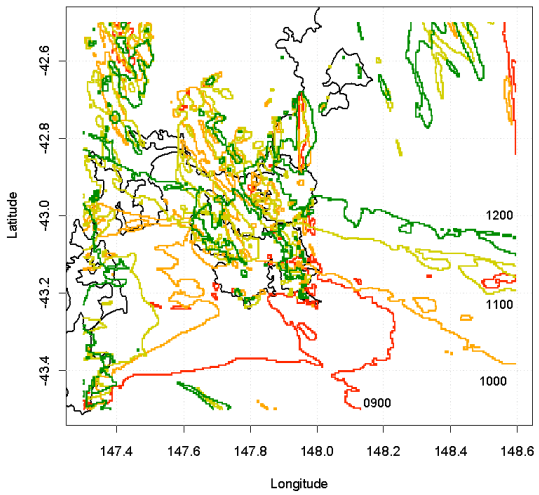

Figure 9 Isochrones of the 240° wind direction isogon at four times (0900 UTC, red lines; 1000 UTC, orange lines; 1100 UTC, light green lines; and 1200 UTC, dark green lines) on 4 January 2013, from the 0.004°-grid-spacing simulation initialised 0300 UTC on 3 January 2013.

References

Belcher S E and Hunt J C R 1998. *Turbulent flow over hills and waves*. Annual Review of Fluid Mechanics 30 507-538.

Bureau of Meteorology 2013a. Special Climate Statement 43 – extreme heat in January 2013. Bureau of Meteorology, 19pp.

Bureau of Meteorology 2013b. *Tasmanian Bushfires Inquiry 2013*. Bureau of Meteorology, 137pp.

Jones D A, Wang W and Fawcett R 2009. *High-quality spatial climate data-sets for Australia.* Australian Meteorological and Oceanographic Journal 58 233-248.

Noble I R, Bary G A V and Gill A M 1980. *McArthur's fire-danger meters expressed as equations.* Australian Journal of Ecology 5 201-203.

The Sydney Easter Sunday Tornado of 2012: a Study of Forecasting Challenges

Andrew Haigh
New South Wales Severe Weather Section,
Australian Bureau of Meteorology
L16, 300 Elizabeth Street, Sydney 2000
a.haigh@bom.gov.au

Introduction

Severe thunderstorms developed to the west of Sydney in the late afternoon of 8 April 2012 and moved over the city in the evening. Damage in the northern suburbs and adjacent forest and expert interpretation of Doppler radar data are strong evidence for the occurrence of a tornado. The tornado occurred in an environment with a low cloud base and large values of low-level vertical wind shear, consistent with recent previous studies, which show this to be a favourable environment for tornadogenesis. The case presented a difficult forecasting scenario in two main aspects. The first related to an early morning environment, which included a strong 750 hPa temperature inversion and appeared unfavourable for thunderstorms. Persistent cloud cover for most of the day, which inhibited surface heating was another perceived factor against convective initiation. What followed was a particularly striking evolution in the local low to mid-level conditions, removing the temperature inversion and transforming the profile into a highly unstable one with little convective inhibition. The afternoon radiosonde data showed an environment favourable for severe thunderstorms and tornadoes. However by the time it became available to forecasters, thunderstorms were already beginning to affect the Metropolitan area. The second difficult aspect was radar signatures from the tornadic cell, which were unusual compared with the common experience of severe weather forecasters in Australia. On the one hand, the Doppler data together with high-resolution low-level reflectivity images indicated the presence of a strong mesocyclone. On the other hand, by reflectivity-based criteria such as height and intensity of the storm cell, it appeared unremarkable at the time of the tornadic activity and fell below a number of criteria, which are often used to classify cells as severe. The scenario was exacerbated by the storm passing through the cone of silence of the closest radar for the duration of the tornadic phase during which a lot of detail, though only at low levels, was visible from this radar. This necessitated reliance on more distant radars for complete sampling of the cell at the time. The event serves as an interesting example for forecasters to study and highlights a number of possible pitfalls and lessons to keep in mind when forecasting severe weather.

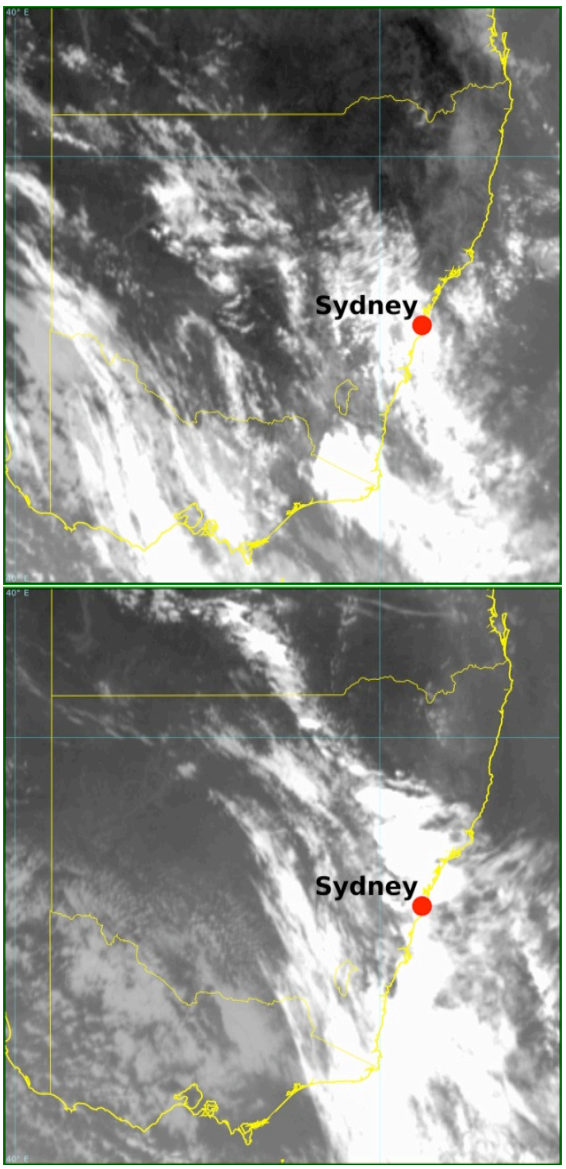

Figure 1 MTSAT-1 infrared Satellite images of cloud over New South Wales (thin yellow lines represent state borders) at 00:32 UTC (left) and 06:32 UTC (right) on 8 April 2012.

Situation and Convective Initiation

On the morning of 8 April 2012, a weak inland trough was over the state of New South Wales (NSW), of which Sydney is the provincial capital, with an upper trough feature well to the west over the state of South Australia. Cool and overcast conditions prevailed over Sydney and the coastal areas to the north and south and also over the Blue Mountains to the city's west, however, most of western NSW was clear of cloud as seen in Figure 1.

Numerical Weather Prediction (NWP) guidance from the high-resolution ACCESS-A version of the Australian Community Climate and Earth System Simulator (ACCESS) model (Puri et al. 2010) indicated favourable conditions for convective initiation in the afternoon, with moist low-level inflow overlaid by a destabilising upper atmosphere ahead of the upper trough. Figure 2 shows an intrusion of warm air at 850 hPa advecting from the northwest into northern and central NSW including the Sydney area ahead of a trough and strong temperature gradient through central NSW lying just to the west of Sydney, overlaid by cooling at 500 hPa due to the approach of the upper trough a considerable distance to the west. Examination of water vapour satellite imagery (not shown) revealed a double upper-level moisture band ahead of the broad upper trough which may hint at the presence of a weak leading short wave trough roughly coincident with the wind direction discontinuity at 850 hPa, though this is difficult to pick up in the model output at 500 hPa which might provide an explanation for the model's insufficient cooling rates in Table 1.

Table 1 Morning-to-afternoon (local time) changes in upper air temperature at Sydney airport on 8 April 2012 as modeled by ACCESS-A compared to actual changes.

Level (hPa)	ACCESS 06 – ACCESS 21 (°C)	Sonde 05 – Sonde 20 (°C)
850	+3.3	+5.3
700	-1.1	-3.2
500	-0.8	-1.1
300	-0.2	0

Figure 2 also shows the near-surface (1000 hPa) moisture distribution with moist air to the northeast of the surface trough and drier air to the southwest. The model prognoses showed upper-level west to northwesterly winds over Sydney increasing with height, in general agreement with the observed soundings at Sydney airport (discussed later). At 850 hPa the north to northwesterly winds maintained low-level moisture over Sydney (850 hPa moisture field not shown) while at the surface, northeasterly winds increased the surface moisture during the day. As it moved eastwards, the surface trough served to initiate convection in the central inland parts of the state, extending in a line to the northwest.

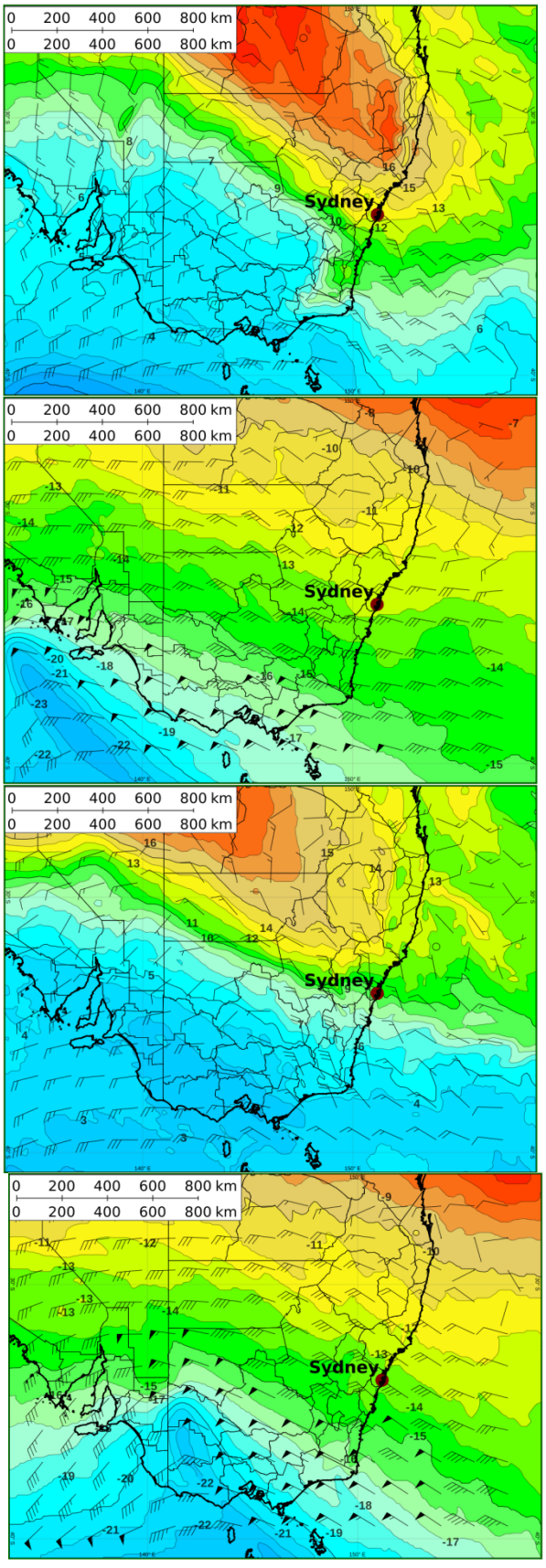

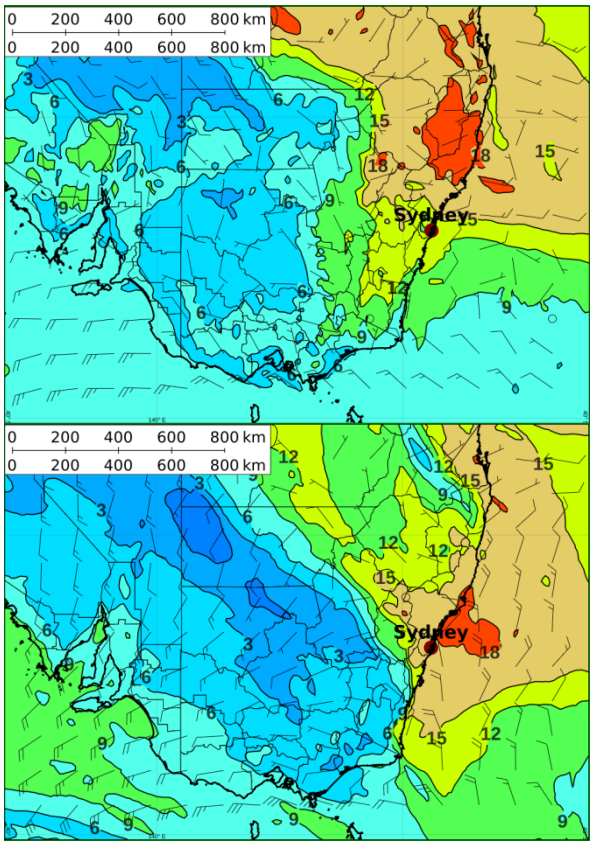

Figure 2 NWP fields from the 1800 UTC 7 April 2012 ACCESS-A model: Temperature (° C – colour scale and labelled contours) and wind in knots (barbs) from the at 850 hPa (top) and 500 hPa (middle) for the 2100 UTC (left) and 0600 UTC (right) time steps, and 1000 hPa wind and dew point (bottom) for the same times, in the same units. The location of Sydney on the east coast of the eastern state of New South Wales is indicated. The vertical line to the left of centre in the images is the border between the eastern states and South Australia to the west.

The thunderstorm activity moved towards the east to southeast during the afternoon and evening. Higher resolution visible satellite images (not shown) reveal more clearly the line of convective activity which developed during the afternoon, the southernmost part of which was a short distance to the west of the Sydney basin at 0632 UTC. Images at other times (not shown) record the fact that the Sydney basin remained cloudy for most of the day. Extensive low cloud prevailed over Sydney in the morning, which cleared during the afternoon, however high cloud (above 12500 ft as indicated by ground-based observations) mostly persisted into the afternoon with only small gaps, this cloud probably arising from sheared off anvil tops from previously developing thunderstorms to the west.

Environmental Factors and Model Performance - *Profile Evolution*

The Bureau's automated National Thunderstorm Forecasting Guidance System (NTFGS, Hanstrum 2004), based on the same version of the ACCESS model referred to in the previous section, indicated favourable conditions for thunderstorms and severe thunderstorms in the vicinity of Sydney during the afternoon and evening. However the morning radiosonde flight showed a strong temperature inversion at 750 hPa, which along with the cloudy conditions in the morning, were considered strong factors against the occurrence of thunderstorms in the Sydney area, though with the surface heating expected further west, convective initiation faced fewer hurdles. Figure 3 shows the morning and afternoon radiosondes side by side, showing the dramatic change between the morning and afternoon conditions. The afternoon profile was fully conducive to development of thunderstorms at the surface late in the day given the surface conditions reflected in AWS data. The moisture profile indicates a greater depth of moist air in the afternoon and viewed together with the temperature profile indicates synoptic upward vertical movement during the day, and given the magnitude of the change, possibly also mesoscale upward vertical velocity, which destabilised the environment. Significant boundary layer moistening is also evident, leading to further destabilisation. At 0500 UTC there is a faint remnant of the previously strong inversion. This scenario is consistent with the conceptual model of poleward flow at low levels resulting in upward vertical motion and destabilisation.

Temperatures measured at a number of pressure levels by the radiosondes were compared with the 1800 UTC 7 April 2012 ACCESS-A model output obtained from de-archived model grids for the closest 3-hourly model time steps (2100 and 0600 UTC respectively) to the radiosonde release times at Sydney Airport. Table 1 shows the evolution of these temperatures and hence the profile from morning to afternoon. These results, together with Figure 2 show that the NWP output successfully modeled the destabilising trend (simultaneous warming at 850 hPa and cooling at higher levels), but that it underestimated the magnitude of the profile evolution.

Thermodynamic and Wind Profile Diagnostics

Table 2 shows diagnostics for Automatic Weather Station (AWS) observations at Terrey Hills, a location which had a tornado pass very close at about 0940 UTC on the evening in question. Terrey Hills is a suburb of Sydney located about 20 km to the north of the city centre and about 28 km to the north of Sydney Airport, only a short geographical distance from the sounding data. Thus the Sydney Airport 0500 UTC sounding is considered representative of the pre-storm environment. Terrey Hills is also the location of the radar which

the tornado passed by in extremely close proximity. At 0700 UTC the results are compared using the morning and afternoon radiosonde traces. Though there was enough CAPE to support strong convection based on the morning trace, the stable layer around 700 hPa, as indicated by SLI (700 hPa), suggested initiation would be unlikely in that environment. The destabilisation during the day together with moistening of the boundary layer provided the requisite favourable convective environment. In addition to this, strengthening upper winds increased the shears between the surface (where winds remained light) and all levels. A leading short wave trough, evident in the model primarily at the low levels and less so at higher levels,may have contributed to the strengthening deep layer vertical shear values. Note also that the weak helicity values for the cases of steering flow storm motion indicate straight line shear, implying deviant motion was required to initiate supercells and tornadoes. The measured cell motion was only a modest deviation yet dramatically increased the magnitude of the helicity.

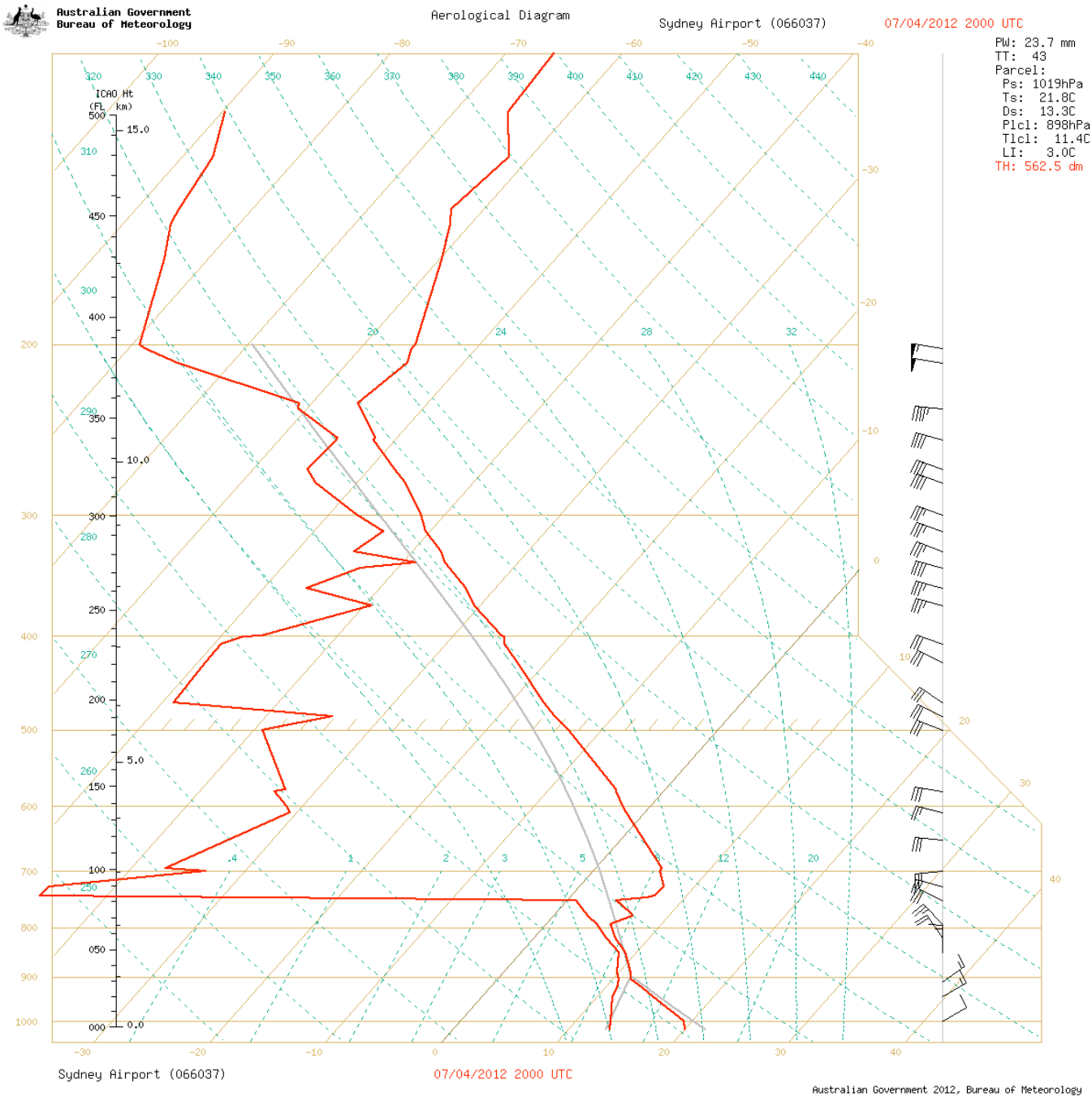

Figure 3a Radiosonde profiles from Sydney airport at 20:00 UTC on 7th April 2012.

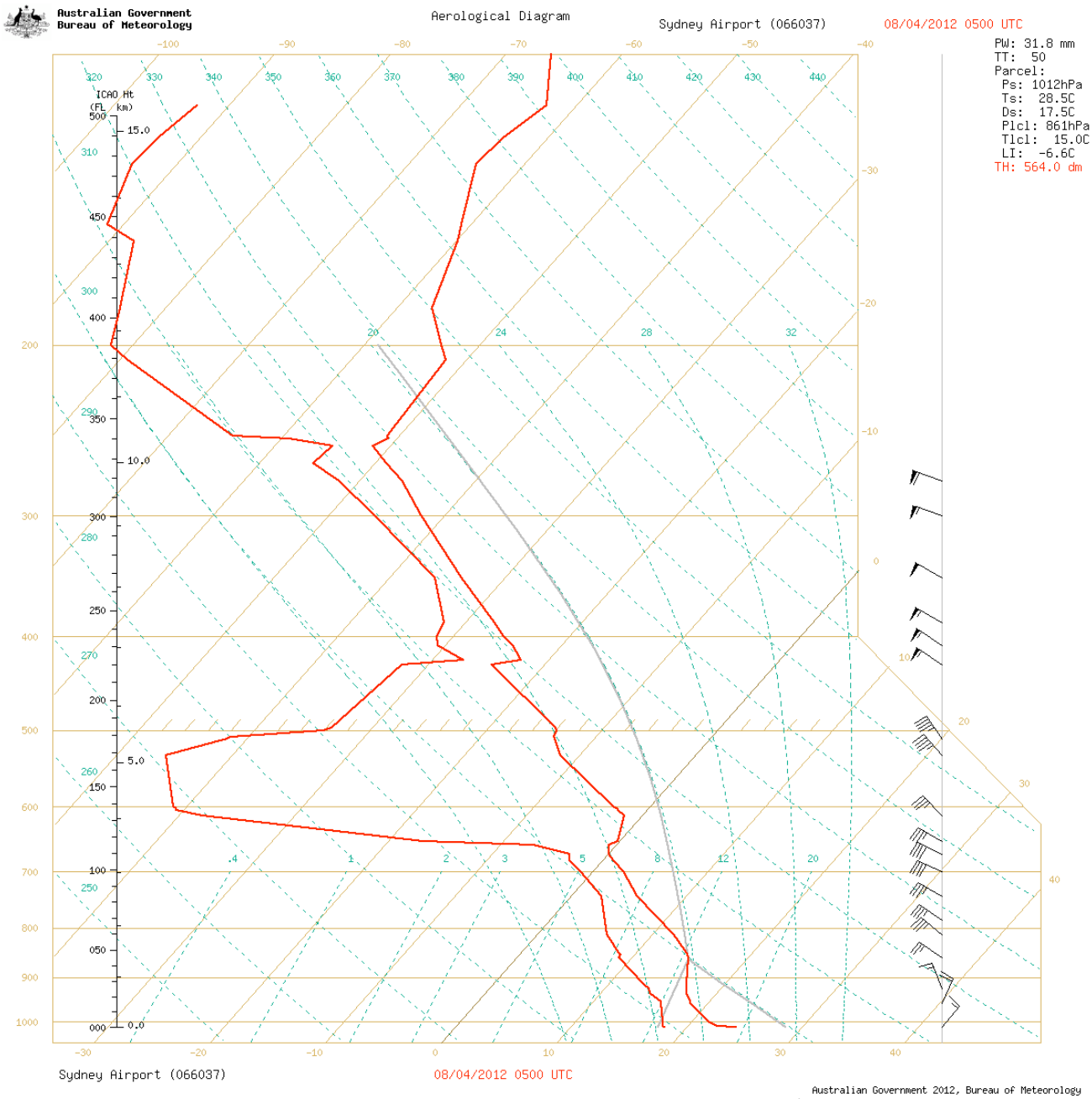

Figure 3b Radiosonde profiles from Sydney airport at 05:00 UTC on 8th April 2012.

The crucial ingredients of a tornadic environment (Thompson et al. 2003, 2004, Markowski et al 2003, Craven et al. 2002, Hanstrum et al. 2002, Rasmussen 2003, Markowski and Richardson 2009) – significant instability, strong low-level shear, a low cloud base and, given the deviant storm motion, significant storm-relative helicity – were all present.

There was little evidence of strong forcing from surface boundaries immediately prior to the event. At 0900 UTC most winds in the Sydney Metropolitan region were light northerly. The wind at Terrey Hills briefly became very light east-northeasterly immediately before passage of the thunderstorm cell, while at Homebush to the southwest a light northwesterly prevailed at the same time. These winds could indicate a convergence zone or a surface boundary, however this feature had no spatial or temporal continuity according to the AWS observations. The brief easterly wind may just as easily have resulted from the influence of a low level pressure perturbation from the storm's updraft resulting in enhanced inflow. The radar data were also carefully examined for pre-existing low level boundaries that the cell may have interacted with, however no such boundaries were obviously evident from the radar data. The reflectivity data does appear to show a weak mesoscale frontal feature moving with the storm cell. This could have been either the inland

trough moving east after triggering the initiation of the storm cell, or the remnants of a squall line, generated by earlier storm activity further to the west, which was in turn initiated by the inland trough. The velocity data indicated a perturbation in the flow to the east of the cell as it approached Terrey Hills consistent with the AWS observation, but again this appeared to be a transient feature caused by the storm itself rather than a pre-existing one that assisted in the formation of the tornado. The apparent lack of low-level boundary observations highlight a mesoscale analysis challenge for this particular event, given that super-cellular tornadoes are normally associated with surface boundaries which can often be identified in post-analysis.

Table 2 Diagnostics for Terrey Hills AWS late on 8 April 2012, all based on surface ascent parcel (no low-level averaging). LCL = lifting condensation level. SLI = surface lifted index. S.R. inflow = storm-relative inflow. CAPE = Convective Available Potential Energy and DMAPE = Downdraft Maximum Available Potential Energy, with updraft/downdraft parcels including virtual temperature correction. Shears are the maximum value of all shear measurements between the surface and the range of levels specified. SREH = storm-relative environmental helicity, calculated using the storm motion vector in the same column. Thunderstorm, supercell and tornado environments classified as meeting or not meeting the NTFGS criteria: NF = not favourable; M = marginal; F = favourable; VF = very favourable. *Storm vectors for the tornadic cell measured from radar – all other storm vectors calculated as the deep layer mean from 800 hPa to 600 hPa. The blank cells indicate identical values to the previous columns (i.e. those that do not depend on the storm vector).

Obs time (UTC)	0700	0700	0800	0830	0900	0900	0930	0930
Radiosonde (YSSY)	2000	0500	0500	0500	0500	0500	0500	0500
Surface T (C)	20.9	20.9	20.8	20.8	19.6		20.0	
Surface Td (C)	18.8	18.8	19.1	19.1	17.6		18.8	
Surface wind (kts)	040/04	040/04	020/04	020/05	360/06		070/04	
Storm vector (kts)	292/27	305/36	305/36	305/36	305/36	286/22*	305/36	286/22*
LCL (ft)	642	654	476	502	604		276	
SLI (700 hPa)	+0.4	-2.8	-3.0	-3.0	-1.3		-2.4	
SLI (500 hPa)	-2.8	-3.9	-4.2	-4.1	-1.8		-3.3	
CAPE (J/kg)	1290	1206	1318	1292	466		992	
S.R. inflow (kts)	15	18	18	18	18	13	18	13
DMAPE (J/kg)	53	277	265	268	368		302	
Conv. gust (kts)	34	58	58	58	64	57	60	53
Shear 0-1.5km (kts)	12	29	28	28	26		31	
Shear 1.5-3km (kts)	33	40	38	38	36		42	
Shear 2.5-4km (kts)	31	41	40	40	38		43	
SREH (surf-3km)	-165	-13	-10	-5	0	-129	-21	-152
Freezing level (ft)	12480	10820	10810	10840	10820		10820	
TS env. (NTFGS)	NF	F	F	F	NF		M	
S-cell env. (NTFGS)	NF	M	F	F	NF		NF	
Torn. env. (NTFGS)	NF	F	F	F	F		VF	

The apparent reduction in instability and lifting condensation levels (LCL) after 0830 UTC as the storm approached Terrey Hills is due to the sensitivity of the updraft parcel to cooling surface temperatures in the evening in light surface winds. Mean layer parcels would be subject to less variation but suffer from assumptions about evolution (or lack thereof) of the boundary layer since the radiosonde release time. Observations from other stations in the Sydney basin at 0700 UTC with temperatures around 23-24^{o}C and dew points around 18-19^{o}C result in LCL values of around 1500-2200ft, likely to better represent the actual cloud base of the cell. These are still quite low and consistent with a tornadic environment from the previous studies mentioned above.

Evolution of a Tornadic Cell

The tornadic cell began as a distinct cell north of Penrith (at the western edge of the Sydney Metropolitan area) at roughly 0825 UTC. It evolved into a complex multi-cell cluster over the next few radar scans before the northern end of the cluster became more organised and first started exhibiting visible rotation at elevated levels at 0910 UTC. The cell then passed over the northern suburbs of Sydney with the slightly left-deviant motion indicated in Table 2, with the size of the mesocyclone circulation shrinking as it approached the radar located at Terrey Hills. The very close proximity to the radar of the event led to some remarkably high resolution, high quality images being captured. Figure 4 shows velocity data from the six scans leading up to the time of closest approach of the cell to the radar, estimated at no more than 1 km. The velocity data are earth-relative and not storm-relative, hence the asymmetry of the feature and aliasing of inbound velocities arising from the storm motion. The distance scale is the same for all six images in the upper part of the figure. A high resolution reflectivity image of the fifth scan (not shown) shows evidence of

precipitation wrapping around the circulation or possibly even debris from the tornado. The elevation angles of the scans in the velocity images were chosen to show the level of the highest (or approximately so) rotational velocity for each scan. Table 3 lists the details of the first five of these scans and measurements of the rotational signature. These measurements were difficult to make for the sixth scan due to the proximity to the radar. Classification was made following the criteria of Andra 1997. The data clearly show the most intense part of the circulation becoming more intense and smaller with time, and also descending in height (with the caveat that the closer to the radar, the lower the height limit of the data sample). After the tornado passed by the radar and dissipated, the intensity of the circulation abated as the cell weakened while moving further east-southeast. Damage reports and photographs by amateur weather chasing enthusiasts indicated a narrow path of severe damage through forest in the Ku-ring-gai National Park including the suburbs of Asquith and Turramurra west of Terrey Hills, with many trees uprooted and others snapped at the trunks or with large branches broken off. A discussion is available on the internet*.

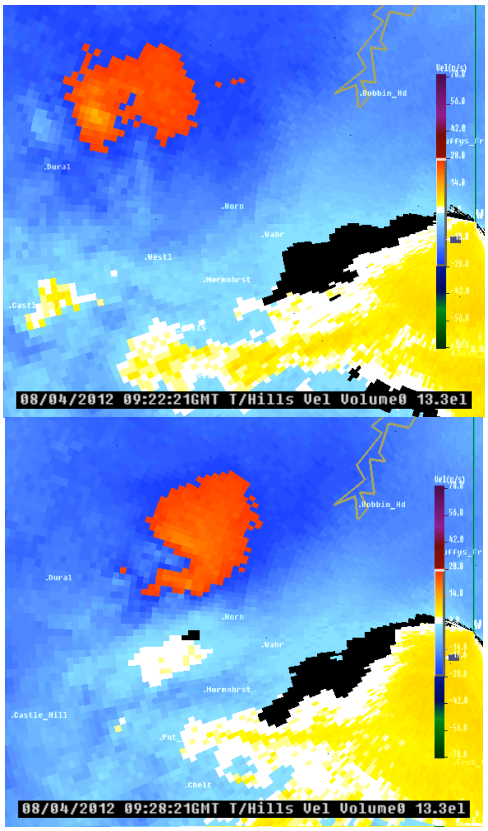

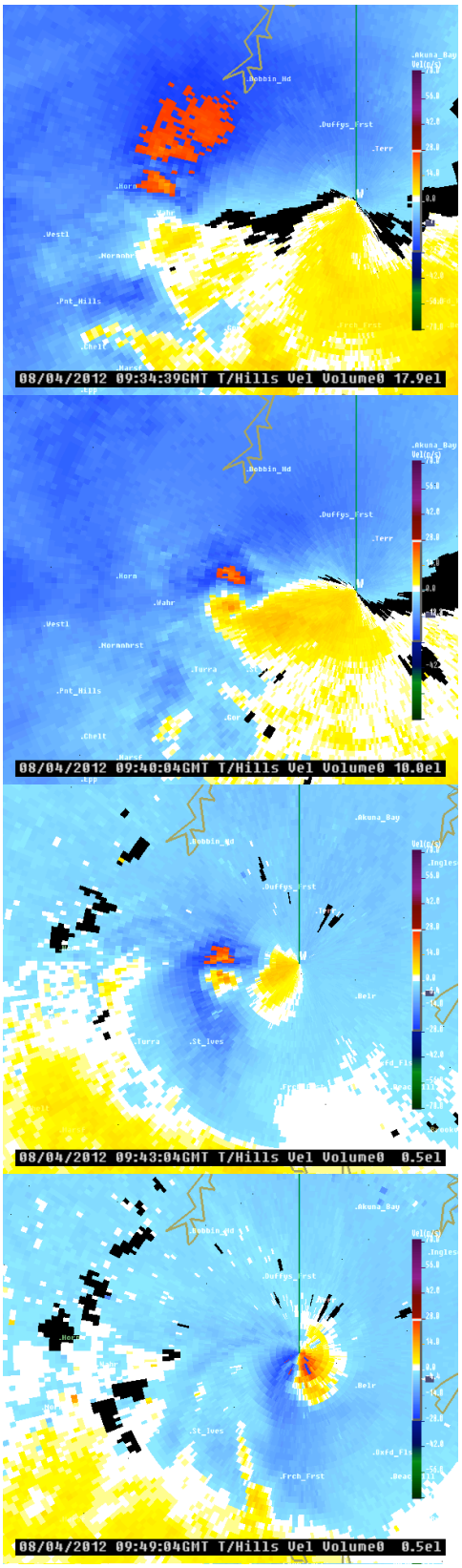

Figure 4 Velocity scans from Terrey Hills radar on 8 April 2012, with details of the first five as listed in Table 4. The sixth scan was at 0949 UTC at the lowest possible elevation angle of 0.5°.

*http://www.extremestorms.com.au/singleton-supercell-asquith-tornado-8th-april-2012/#comments

Table 3 Scan details and mesocyclone velocity measurements of the first 5 radar scans in Figure 4. Aliased velocities have been corrected using the radar's Nyquist velocity of approximately 26 m/s. AMSL = Above Mean Sea Level.

Base scan time (UTC)	Actual scan time (UTC)	Elev angle (°)	Approx. Height AMSL (m)	Inbound v (m/s)	Outbound v (m/s)	Average v (m/s)	Diameter (km)	Classification (Andra 1997)
0919	0922	13.3	3830	-37	4	20.5	7.7	Moderate
0925	0928	13.3	2880	-34	2	18	4.8	Moderate
0931	0934	17.9	2680	-36	8	22	2.2	Moderate
0937	0940	10.0	1110	-33	15	24	1.2	Strong
0943	0943	0.5	220	-35	14	24.5	0.9	Strong

Discussion of Forecasting Challenges

Essentially there were two forecasting challenges on the day. The first of these was forecasting the occurrence of thunderstorms in the Sydney Metropolitan area, the key ingredient being the large amount of destabilisation which occurred. The morning conditions (particularly the comparatively low dew points compared to the afternoon), together with the very strong mid-level inversion and the cloud which was expected to remain throughout the day, weighed strongly against the likelihood of thunderstorms in the Metropolitan area, although conditions were more favourable further west where sufficient heating was forecast. Some upper destabilisation was forecast during the day by the ACCESS-A model, but what actually occurred exceeded this forecast.

The second challenge was interpreting the rapidly evolving radar signatures and anticipating the tornadic activity. In Australia, criteria for assessing individual storm cells as severe use a combination of reflectivity-based and velocity-based methods. Examples of the reflectivity-based ingredients are peak reflectivity, height of the 50 dBZ reflectivity level, Vertically Integrated Liquid (VIL), displacement of an echo top from the cell's low-level reflectivity gradient and the presence of overhangs and bounded weak echo regions. Forecasters are naturally more likely to actively look for rotational signatures when these features become apparent. Under greater time pressure, there is a natural tendency to filter the information to focus on the most obviously noteworthy features. At the time the tornado occurred, the tornadic cell appeared to be of relatively low intensity. It fell below the usual reflectivity-based criteria used for assessing a cell as severe. The cell's intensity also fell below the intensity of other cells in the region. From the time that obvious rotation is first evident in the data at 0920 UTC, the storm cell was at least partially in the cone of silence of the Terrey Hills radar. At the time of the tornado only the lowest regions of the storm were sampled from Terrey Hills, hence the need for data from other radars to make a complete assessment of the intensity and height of the cell. There were two other such radars sampling the event – at Wollongong to the south and Newcastle to the north. In the leadup to the tornado the tornadic cell was visually unimpressive by criteria of intensity and vertical extent as seen by these radars, as well as other morphological criteria mentioned above. Regarding maximum reflectivity, the tornadic cell in the northeast of the Metropolitan area (labelled as storm A in Table 4) was less intense than the cell to the southwest (labelled as storm B) on all scans from 0920 to 0950 UTC from the Wollongong radar, as was the case for the Newcastle radar at 0920 and 0930 UTC (the subsequent two scans are missing from the data archive). Regarding VIL, the intensity of the second cell exceeded that of the tornadic cell for the same four consecutive scans of the Wollongong radar. These data are summarised in Table 4. All these features tend to draw the forecaster's attention to the more intense cell as the one more likely to be severe. In such situations, heavy reliance is placed on recognition of Doppler rotational signatures for alerting to the presence of supercells and potential tornadogenesis.

Table 4 Comparison of intensity of storm A (tornadic cell) with storm B (in Sydney's south) by peak reflectivity and Vertically Integrated Liquid (finding the pixel of highest value in each cell for each scan). VIL was only available in the data for Wollongong radar.

Radar / Scan time (UTC)	Peak reflectivity (dBZ)	Peak VIL (kg/m2)
Wollongong / 0920	A 56	A 12
	B 66	B 39
Wollongong / 0930	A 54	A 11
	B 69	B 70
Wollongong / 0940	A 55	A 12
	B 65	B 31
Wollongong / 0950	A 53	A 9
	B 63	B 30
Newcastle / 0920	A 48	N/A
	B 57	
Newcastle / 0930	A 48	N/A
	B 56	

The velocity data indicated strong rotation on a small scale, strong evidence of supercellular activity despite the relatively low reflectivity level of the cell. Warning guidelines in Australia have

traditionally only called for issuing of a tornado warning if either a credible report is received of a tornado occurring in an environment where further such activity is possible, or if a very convincing radar signature such as a high gate-to-gate Tornado Velocity Signature velocity couplet is observed. Although the mesocyclone circulation became very small as the storm approached the radar (as small as 0.9 km), this was still too large to conclude in real time that the radar velocity data directly represented a tornadic circulation. On the evening in question a Severe Thunderstorm Warning was issued but it did not include a Tornado Warning.

Conclusions

The Sydney tornado of 8 April 2012 occurred at the end of a day, which featured unusually rapid evolution of the vertical profile resulting in a favourable environment for thunderstorms and tornadogenesis. Once thunderstorm activity began the radar signatures indicating a strong mesocyclone were (unusually) not accompanied by strong reflectivity-based signatures, which forecasters also look for when assessing the severity of thunderstorms. In light of this scenario, the following suggestions are made regarding severe weather forecasting practices in Australian forecasting offices, many of which are simply to re-emphasise existing ideals:

- Be alert to a wide range of possible scenarios including underestimation by models of the amount of change of the temperature, moisture and wind profile with time, especially in situations where strong upper winds can lead to rapid advection of airmasses and vertical motion.
- Visually inspect model output in a variety of ways including in vertical profile. This has since become possible with the introduction of the Visual Weather software package into the Bureau.
- Analyse different scenarios for profile evolution including modifying model profiles to include larger changes than the model trend suggests. This should be possible to set up with the Visual Weather package.
- Be aware that only a small deviation in storm motion from the steering flow is necessary to dramatically increase the SREH from a low value on a “straight line” hodograph to a value large enough to support tornadoes.
- Inspect Doppler velocity images routinely with equal priority to reflectivity images.
- Assess to the use of the WDSS Mesocyclone Detection Algorithm in Australian forecasting offices, where the quality of the data from the newer Doppler radars permits.
- Emphasise the morphological criteria for recognising storm cells as severe, with equal importance to the intensity and height criteria which are also used. Finally, this case serves to illustrate the fact that a storm cell need not stand out as particularly intense at first glance on a radar scan to support tornadogenesis. The parent cell was unremarkable in terms of reflectivity values, VIL and vertical extent, making morphological identification particularly important.

Acknowledgements

The author wishes to thank Harald Richter and Ewan Mitchell for technical assistance in retrieving and analysing archived NWP grids, which helped add valuable data to this study, and also Michael Logan for helpful discussions on the manuscript. The author also thanks the two anonymous reviewers for their helpful comments which enabled significant improvements to the original manuscript.

References

Andra, Jr., D. L., 1997: The origin and evolution of the WSR-88D mesocyclone recognition nomogram. Preprints, *28th Conference on Radar Meteorology,* Austin, TX, Amer. Meteor. Soc., 364-365.

Craven, J. P., H. E. Brooks, and J. A. Hart, 2002: Baseline climatology of sounding derived parameters associated with deep, moist convection. Preprints, 21st Conference on Severe Local Storms, San Antonio, Texas, Amer. Meteor. Soc, 643-646.

Hanstrum, B.N., Mills, G.A., Watson, A., Monteverdi, J.P., Doswell, C.A. 2002: The cool-season tornadoes of California and Southern Australia. *Wea. and Forcasting,* **17,** 705-722,

Hanstrum, B.N., 2003: A National NWP-based thunderstorm and severe thunderstorm forecasting guidance system. 15th Annual Workshop of Meteorology Research Centre (BMRC) Modelling Workshop: ‘Current issues in the paramerization of convection’ October 13th to October 16th, 2003. Extended abstracts, Bureau of Meteorology Research Centre, Melbourne.

Markowski, P. M., C. Hannon, J. Frame, E. Lancaster, A. Pietrycha, R. Edwards,and R. Thompson, 2003: Characteristics of vertical wind profiles near supercells obtained from the Rapid Update Cycle. *Wea. Forecasting,* **18,** 1262–1272.

Markowski, P. M., and Y. P. Richardson, 2009: Tornadogenesis: Our current understanding, forecasting considerations, and questions to guide future research. *Atmos. Res.*, **93**, 3–10.

Puri, K. et al. 2010: Preliminary results from Numerical Weather Prediction implementation of ACCESS. *CAWCR Research Letters,* **5,** 15-22.

Rasmussen, Erik N., 2003: Refined Supercell and Tornado Forecast Parameters. *Wea. Forecasting*, **18,** 530–535.

Thompson, R. L., R. Edwards, J. A. Hart, K. L. Elmore, and P. M. Markowski, 2003: Close proximity soundings within supercell environments obtained from the Rapid Update Cycle. *Wea. Forecasting,* **18,** 1243–1261.

Thompson, R. L., R. Edwards, and C. M. Mead, 2004: An update to the supercell composite and significant tornado parameters. Preprints, *22nd Conf. on Severe Local Storms,* Hyannis, MA, Amer. Meteor. Soc., P8.1.

Radar-derived statistics of storm cells in South East Queensland

Justin R. Peter[A], Michael Manton[B], Rod Potts[A] and Peter May[A]
[A]The Centre for Australian Weather and Climate Research, Bureau of Meteorology
[B] School of Mathematical Sciences, Monash University, Clayton, Victoria

Introduction

The city of Brisbane and surrounding area is in the sub-tropics and, owing to the geographical location and surrounding topography (see Figure 1) is subject to occasional severe thunderstorms. A significant fraction of these storms can result in widespread damage. As such, there is considerable benefit in gaining a better understanding of the structure, spatial distribution and statistics of convective precipitation in Brisbane and the surrounding South East Queensland (SE QLD) region. This study presents climatological statistics of precipitating cloud systems (storms) observed by radar. We report on similar statistics as Potts et al. (2000) who presented statistics of storms in the Sydney region based on a 12-week period during summer. However, we examine all storms during all seasons of the period 2000–2006. Furthermore, we build on the analysis of Potts et al. (2000) as we examine how the storm properties vary with synoptic forcing and season. This is achieved by conducting a cluster analysis of variables derived from radiosonde data obtained at Brisbane airport prior to analysing the radar-derived precipitation data.

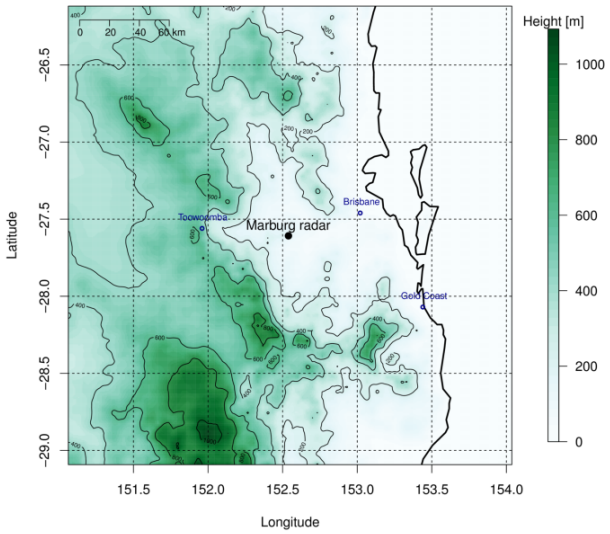

Figure 1 Topographic map of South East Queensland. The capital city and major population center of Brisbane is located at sea level near the coast. Marburg radar is located west of Brisbane city, at an altitude of 300 m near the foot of the Great Dividing Range, which rise to about 1100 m above sea level within the displayed domain.

Data Sets

a. Radiosonde data

The radiosonde data comprises the historical record of radiosonde measurements at Brisbane airport over the period January 2001 to the end of March 2008. The Bureau of Meteorology (Bureau) obtains soundings twice daily (at 0000 and 1200 UTC; local time is UTC plus 10 hours) from balloon releases. The environment for a day was generally computed from the 0000 UTC sonde if it was available or from the 1200 UTC sounding if not. The analysis was performed on observations interpolated to the "standard levels" from 1000 hPa to 20 hPa. The standard levels are 1000, 925, 850, 700, 500, 400, 300, 250, 150, 100, 70, 50, 30 and 20 hPa.

b. Radar data

The radar data set was obtained from the Bureau's Marburg radar (27.61°S, 152.54°E) (see Figure 1). It is a WSR74S/14 radar which transmits 10 cm (S-band) wavelength electromagnetic radiation. It was installed in 1993 and has been taking near continuous measurements of rainfall west of Brisbane since. Over six years of archived data were analyzed, extending from April 2000 to the end of December 2006. The Marburg radar collected a three-dimensional volume of data every 10 minutes. Each volume consists of fifteen tilts ranging in elevation angles from 0.5 to 32 degrees. The radar is located at an altitude 370 m above sea level (asl) and has a good overall view of precipitation in most directions except for some beam blockage by topography in a narrow sector to the south-southwest, where the topography reaches an altitude of nearly 900 m (see Figure 1). However, the radar beam at 0.5° elevation tilt is at an altitude of about 670 m at 55 km (under standard refractive conditions) range while that of the 1.0° beam about 1160 m. Any bias in the radar measurements due to beam blockage is therefore considered minimal. The Marburg radar collects data in polar format, which was subsequently transformed to a three-dimensional Cartesian grid using a "nearest neighbour'' approach; the resulting Cartesian radar data has a horizontal grid of 520×520 km and a grid spacing of 1 km. The radar data has also had quality control algorithms applied to it. Permanent echoes were removed with a Doppler filter which removes signals with a

near-zero velocity. Anomalous propagation echoes are removed using the fuzzy logic approach of Hubbert et al. (2009).

Table 1 Variables derived from the Brisbane soundings. These were used as input to the K-means clustering algorithm to partition the sounding data into synoptic regimes with similar characteristics.

Variable	Description
U	Westerly wind at 850 hPa
V	Southerly wind at 850 hPa
Shear	RMS wind shear between 500 and 850 hPa
Total-totals	$T(850)-2\times T(500)-T_d(850)$ where T and T_d are the temperature and dew point temperature, respectively.
QU	Westerly water flux up to 250 hPa
QV	Southerly water flux up to 250 hPa
TW	Total water up to 250 hPa

The storm cell data set was obtained using the objective classification method of Dixon and Weiner (1993) (TITAN) processed on the Cartesian data. TITAN is used operationally by Bureau forecasters to enable identification of storms and allow short-term forecasting of storm tracks (Potts, 2005). The TITAN software identifies precipitation cells as contiguous volumes of pixels that exceed a prescribed reflectivity and size threshold, which for this analysis were 35 dBZ and 30 km^3, respectively. TITAN outputs various fields including, the time and geographical location of a storm, size parameters such as area, volume and top and speed and direction information. Specifying a minimum reflectivity threshold of 35 dBZ limits the analysis to (mostly) convective precipitation. As such, we refer to these features as storms or cells.

Synoptic Regimes

To objectively classify the synoptic regimes we take a similar approach to Connor and Bonnel (1998) and conduct a K-means clustering analysis (Hartigan and Wong, 1979) on variables derived from soundings obtained at Brisbane Airport. The variables chosen to represent the synoptic environment are listed in Table 1 and are calculated from the standard level sounding data. They encompass measures of the prevailing winds and moisture fluxes (U, V, QU, and QV), instability (shear and total totals) and total precipitable water (TW) and combined provide a description of the propensity for rainfall.

The seasonal cycle of the clustering variables is shown in Figure 2. The variable with the most pronounced seasonal cycle is total atmospheric water (TW), followed closely by atmospheric stability (TT). In particular, both TW and TT are lower in the winter months; that is the atmosphere is generally drier and more stable. The largest values of atmospheric moisture occur during the summer months (December–February. The variables used in the cluster analysis clearly distinguish the sub-tropical climate characterised by a "wet" (summer) and "dry" (winter) season.

Three synoptic regimes were quantitatively identified and the resultant median soundings are plotted in Figure 3(a): (1) a regime with low TW and TT, and mainly westerly to southwesterly winds (black) which predominates during winter; (2) a trade wind regime with mainly southeasterly winds and moderate instability (green) and, (3) a regime characterized by an unstable atmosphere and surface flows with large equivalent potential temperature. We shall refer to these regimes as westerly, trade wind and northerly, respectively.

Cell Statistics

a. Cell location frequency

Figure 4 shows the spatial frequency of each synoptic cluster. The total number of cells assigned to each cluster is indicated and shows that storms during the northerly and trade regimes are the most numerous. All regimes show an increased propensity for storms to form north and south of the radar, parallel with the Great Dividing Range indicating the importance of topography in generating and sustaining storms regardless of the prevailing wind direction and steering flow. Additionally, the range of enhanced storm location frequency during the westerly and northerly regimes does not extend as far east as during the trade regime, which is due to two factors: (1) trade wind storms form readily over the ocean and their frequency is enhanced due to topographic effects in the prevailing southeasterly flow and, (2) cells in the northerly and westerly regimes are less likely to form over the ocean, but rather, have their genesis over land.

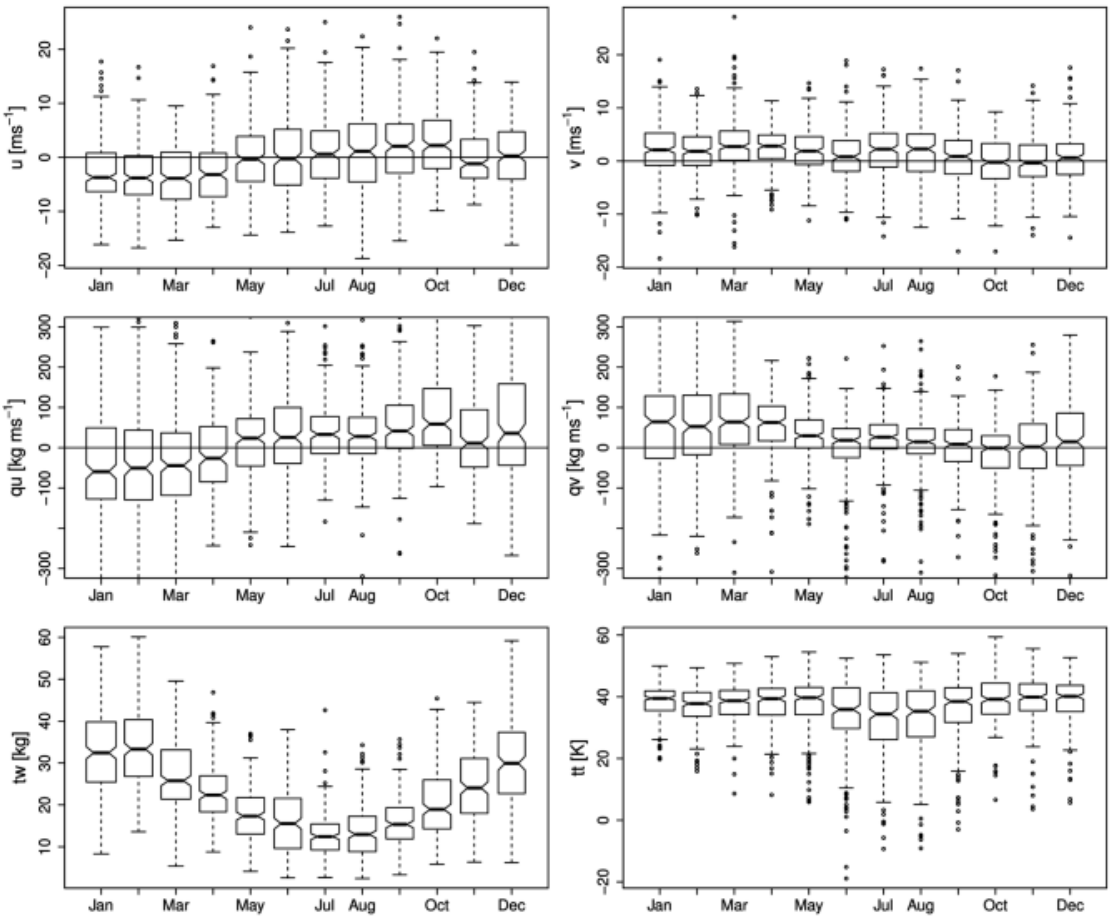

Figure 2 Box and whisker plots of the monthly-averaged seasonal variation of sounding-derived variables for the period January 2001 to March 2008. The wind direction and moisture flux exhibit a seasonal cycle, whereby they are mainly from the southeast during January–March. This is representative of the southeasterly trades present during summer. The profiles of total water and atmospheric stability indicate a distinctly drier and more stable atmosphere during winter.

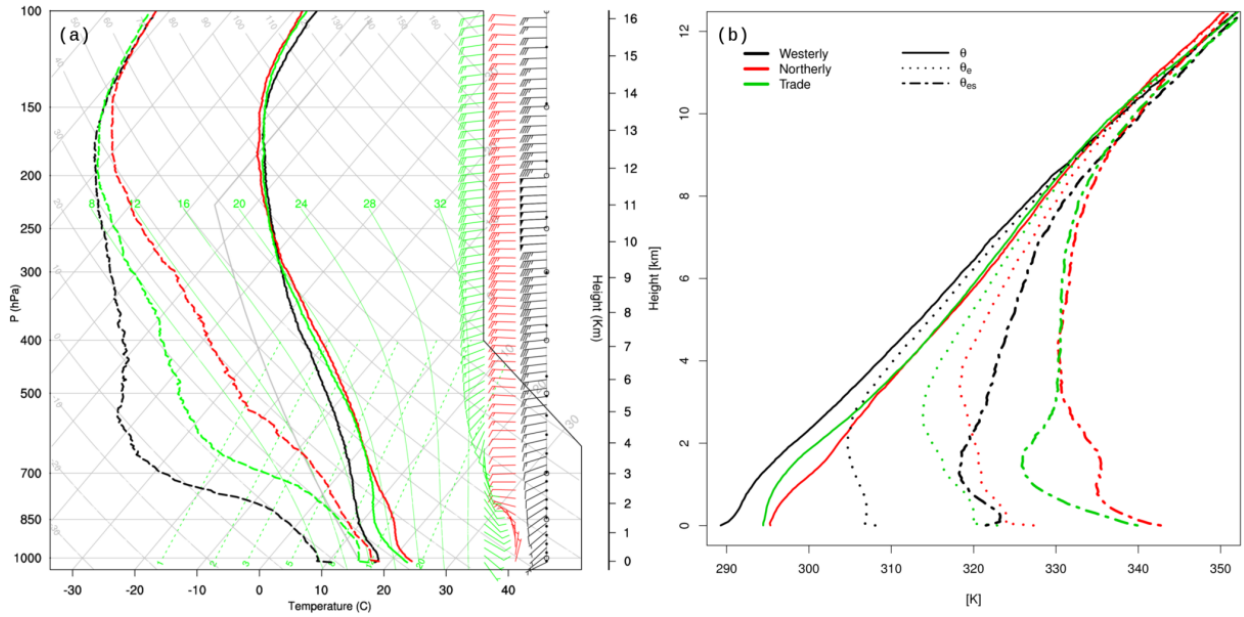

Figure 3 (a) Skew-T log p diagrams of the median temperature and dew point for each of the synoptic regimes identified by the K-means clustering algorithm. (b) Profiles of the median values of potential temperature (θ), equivalent potential temperature (θ) and saturation equivalent potential temperature (θ).

b. Statistics of cells

Previous studies have shown that the frequency distribution of cell area (or an equivalent horizontal dimension) can be represented by a truncated lognormal distribution (e.g. Lopez, 1977; Potts et al. 2000; Cifelli et al., 2007). The probability distribution function (pdf) of cell area is plotted in Figure 5(a), where the horizontal axis has been scaled logarithmically. The resulting histogram is nearly symmetrical, however skewed to smaller areas (if cell area was distributed lognormally then its logarithm will be distributed normally). A visual degree of departure from normality can be determined from Figure 5(b). The horizontal axis is the cell area (on a logarithmic scale) and the vertical axis is the cumulative probability expected from a lognormal distribution with the same mean and standard deviation as the original data; the oblique line represents a perfect fit. The observed and the theoretical distributions coincide over several orders of magnitude of cell area through the range 15–200 km^2 which corresponds to a cumulative probability in the range 10–95%. At extreme values the observed distribution does not contain as many samples as predicted by a lognormal distribution. The departures from non-normality can be explained; at smaller values of cell area the distribution has been truncated due to the condition of imposing a minimum volume of 30 km^3 for cell identification, while at larger values the maximum range of the radar underestimates the size of storms which are not fully contained within the radar viewing domain. This is typical of a truncated lognormal distribution and a similar relationship has been observed in trade wind clouds (e.g. Lopez. 1977). Since the curves for all three regimes coincide, these observations indicate that the truncated lognormal size distribution of precipitation area appears to be insensitive to the synoptic scale forcing.

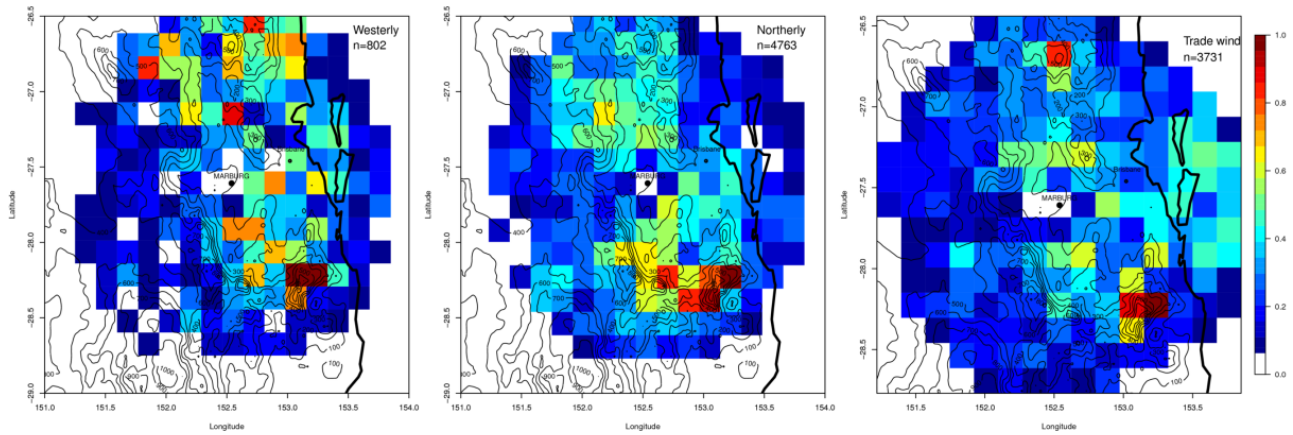

Figure 4 Spatial frequency of occurrence of storms in each of the synoptic regimes. The clusters correspond to: (1) westerly, (2) northerly and, (3) trade wind regimes. The number of samples in each cluster is shown.

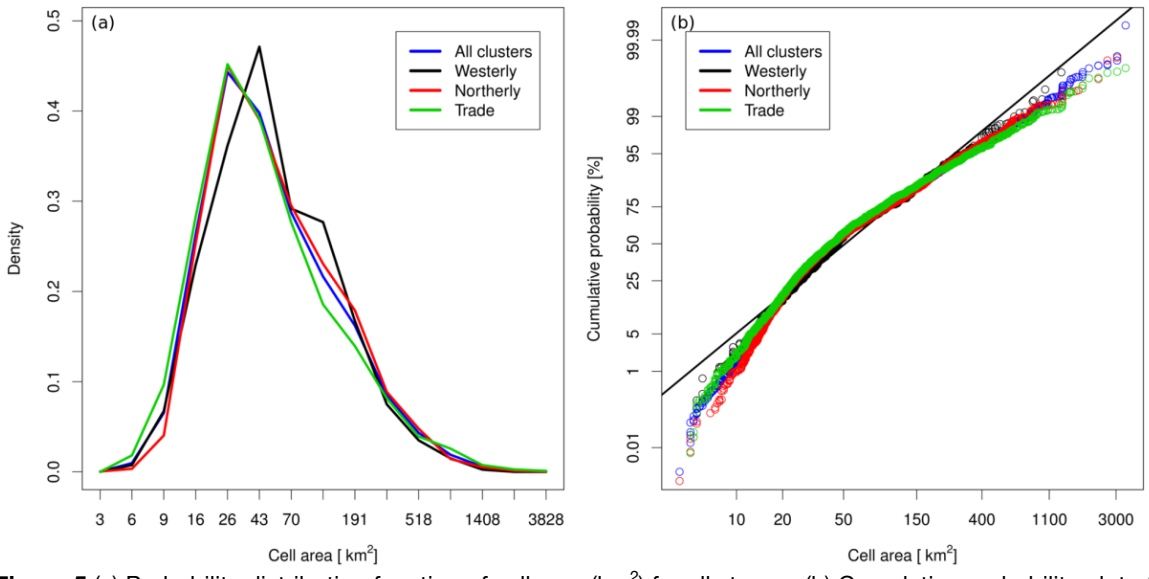

Figure 5 (a) Probability distribution function of cell area (km^2) for all storms. (b) Cumulative probability plot of observations of cell area plotted against theoretical probabilities obtained from a lognormal distribution. The oblique black line represents a perfect fit.

The areal coverage of storms of the westerly regime is skewed to larger values than the other two regimes especially the trade regime. To quantify whether this difference is statistically significant, the geometric mean and standard deviation were calculated and t-tests performed comparing the pdfs between each regime. The mean and standard deviation values are tabulated in Table 2 and values, which are significantly different (at the 95% level), are denoted with an asterisk. The t-test confirmed that the mean areal coverage of storms during the trade regime is statistically smaller than the westerly and northerly regimes, however the difference between the northerly and westerly regimes was not significant. Therefore, despite cells in the westerly regime being skewed to larger sizes, on a climatological basis only the trade regime cells distinguish themselves by having a smaller mean areal coverage. Similar conclusions were reached for cell volume.

Table 2 Cell property summary statistics for the three synoptic regimes. The geometric mean and standard deviation are shown for variables. Values with significantly different (at the 95% level) are marked with an asterisk.

Cell property	Synoptic cluster			
	All	Westerly	Northerly	Trade
Area [km^{2}]	51.1 ±2.7	52.9±2.6	53.8±2.6	47.6 ±2.8 *
Volume [km^{3}]	119.6 ±3.1	127.1 ±3.0	126.2±3.0	110.2 ±3.0 *
Top height [km]	5.8 ±1.5	5.9±1.6	5.9±1.4	5.6 ±1.5
Rain rate [mm/hr]	11.0 ±1.7	13.1±1.8*	10.8±1.7	10.7 ±1.8

The pdf of cell height is shown in Figure 6(a) and the cumulative frequency in Figure 6(b). Here, cell height is defined as the maximum height of the 35 dBZ echo achieved by a storm during each 10-minute sample. For each regime the cell height is distributed lognormally throughout most of the troposphere, with significant departures occurring at the extremes. More storms exist with heights below 3 km and above about 13 km than predicted by a lognormal distribution. The enhanced number of storms with tops above 13 km is associated with the presence of the thermal tropopause, which is evident in the soundings shown in Figure 3(a). The capping of storms at the tropopause is noticeable in the cumulative probability plot (Figure 6(b)), however, the presence of a mode at this height is less obvious in the pdf (Figure 6(a)). Below 4 km, two modes exist in the pdf of cell height, one centered near 3–3.7 km and another near 1.6 km. It is these modes, which contribute to the increased number of storms in the cumulative distribution relative to a lognormal distribution. These modes correspond to the height of the freezing level and the height of the trade wind inversion respectively. The mode near the freezing level is most pronounced for the trade and westerly regime cells. The profile of θ_{es} (Figure 3(b)) shows that this height is both the height of the freezing level and the top of the climatological trade inversion, which extends from 1.5–3 km. In contrast, the northerly regime exhibits a neutral layer located near 1 km (below the level of the trade inversion), followed by an unstable thermodynamic profile up to the freezing level. This suggests that the mode located near 3.5 km (in the westerly and trade regimes) forms due to the combined presence of the stable layer at the freezing level and the trade inversion below. It appears that, despite the presence of an inversion near the freezing level in the northerly regime storms, the atmosphere is sufficiently unstable for convection not to be capped there. The mean height of storms in the trade regime is statistically lower than the other two (at the 95% confidence level), however there is no statistically significant difference in the mean of the westerly and northerly regime storms. Furthermore, there is an increased number of cells which penetrate above 8 km in the westerly regime compared to the trade and northerly. This has resulted in an indication of a bimodal distribution of cell heights (between the freezing level and tropopause) in the westerly regime. Despite the presence of modes in the pdf of cell height near the trade and freezing levels inversions, the majority of storms in all regimes make it through these and into the mid-troposphere. Between the freezing level and the tropopause the cell height is well-described by a continuous, unimodal lognormal distribution. The number of storms in this height range encompasses between 5–99% of the cumulative probability. These observations hint as to the reason why some observations have indicated trimodal cloud-top height distributions (e.g. Johnson et al., 1996), while others (e.g. May and Ballinger, 2007) have observed a continuous distribution; it may be due to the stability profile of the atmosphere when the observations were obtained.

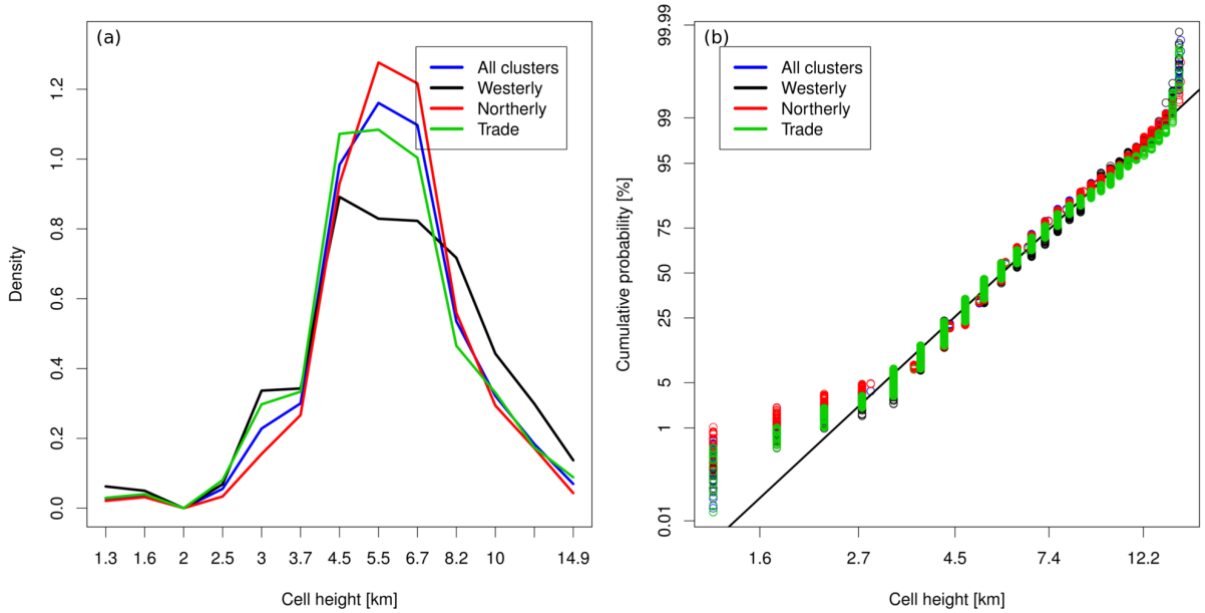

Figure 6 Same as Figure 5 but for cell height.

In summary, the pdfs of cell area, volume and height were distributed according to truncated lognormal distributions. Statistical tests (t-tests) conducted on the pdfs found that the cells in the trade wind regime were significantly smaller (by all measures) than those in the westerly and northerly regimes. Furthermore, cells in the westerly regime were found to be skewed to larger area and taller heights than the northerly regime while having corresponding pdfs for cell volume. This suggests cells in the westerly regime are comprised of more very deep, widespread stratiform precipitation while those in the northerly regime tend to be more convective in nature. Finally, some evidence of trimodal cell-top heights was found, however, only during the westerly and trade regimes. This suggests that a cloud-top height mode near the freezing level is more likely to occur if a low-level trade inversion also exists.

Precipitation Rate

The pdf and accumulated frequency of precipitation rate for storm cells are shown in Figure 7. As for measures of cell size, the rain rate is distributed lognormally in the approximate range 5–30 mm/hr, comprising about 85% of the cumulative total, with departures (indicative of a truncated lognormal distribution) only evident for light and extremely heavy rainfall events. The geometric mean rain rate for the westerly regime is the largest at 13 mm/hr, about 2 mm/hr larger than the other regimes. It can be seen from the pdf that theincreased mean rain rate is due to a significant number of heavy rain events exceeding 20 mm/hr and fewer moderate and light rain events (< 10 mm/hr). The heavier rain rate of westerly cells is associated with a larger fraction of the cells comprised of larger reflectivities (not shown).

Interestingly, the westerly regime exhibits larger precipitation rates. This is despite the westerly regime being more stable and having a lower total column water amount. This suggests that the skew to larger rain rates in the westerly regime is a consequence of precipitation during this regime being dominated by a smaller number of heavy rainfall events. The relative proportion of storms occurring during the westerly regime was 18%, making the statistics of this regime more susceptible to the presence of extreme events, for instance, east coast lows.

Exceedance Rate

Figure 8 shows exceedance rate plots for each of the aforementioned TITAN-derived variables. The exceedance rate has been calculated as the ratio of total time cells greater than a certain value are present, to the total time. The total time represents the number of days during which any cells were registered. It therefore represents the fraction of time cells exceed a threshold value for any day on which precipitation was registered. Accordingly, curves represent the relative exceedance rate of a variable, rather than the absolute exceedance rate. Also note that the exceedance rate is on a logarithmic scale.

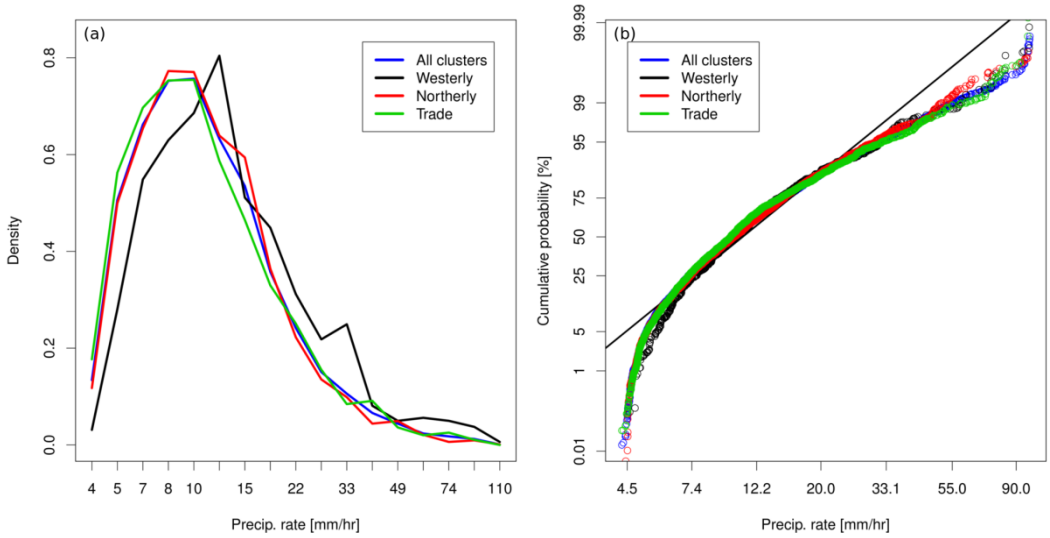

Figure 7 Same as Figure 5 but for precipitation rate.

It is worthwhile to consider the exceedance rate plots in relation to the pdfs presented previously. The pdfs of storm size characteristics (cell area, volume, height and rain rate) indicated significantly smaller values for the trade wind regime. Referring to Figure 8 it can be seen that storms in the trade regime, despite being smaller (in the mean sense), the largest storms (e.g. cell area ≥ 1000 km^2) have exceedance rates comparable to those in the northerly or westerly regimes. Similarly, cell height exceedance rates for westerly regime storms with tops above about 8 km have rates comparable to those of the trade regime and even those of the northerly regime for the very tallest storms with tops over about 12 km. Furthermore, the westerly and northerly regime storms have (statistically) similar physical dimensions, however, the exceedance rates of northerly storms is much larger than those in the westerly regime.

The larger precipitation rates of winter regime storms (see Figure 7(a)) is evident in the exceedance rates of precipitation rate where it can be seen that westerly storms with exceptionally large precipitation rates have exceedance rates comparable to those of storms in the northerly regime.

These results create a rather complex picture of the nature of storms in SE QLD, however, the main results can be stated as: trade wind regime storms are generally the smallest and their precipitation rates the smallest; northerly regime storms tend to be large, and persist with large precipitation rates; westerly regime storms have, on average, the largest precipitation rates, however, they have shorter lifetimes than storms of the other regimes.

When interpreted in light of the stability profiles presented in Figure 3, it is seen that the northerly regime, being the most unstable with the largest heat and moisture fluxes, has the most intense and largest storms. The westerly regime, which is the driest and most stable, has relatively short-lived storms, which is most likely explained by the entrainment of cool dry air aloft which restricts their growth. However, it is perplexing that precipitation rates should be (on average) larger than the other, more unstable regimes. However, similar contrasts have been found in Darwin in tropical Australia where average precipitation rates during the "active" phase of the monsoon are generally higher than during the "break'' period; storms during the break are generally larger and more electrically active than those of the active phase. This was attributed to storms forming during the active monsoon being the result of synoptic scale forcing, while those during the break period were more influenced by the underlying surface and sea-breeze processes (Kumar et al., 2013). A similar case is most likely present here, where the storms which form in the stable westerly flow (predominant during winter) are the result of large scale forcing, such as east coast lows, while those which form in the more unstable trade and northerly regimes are more susceptible to local heating (such as over the ranges) and the afternoon sea breeze.

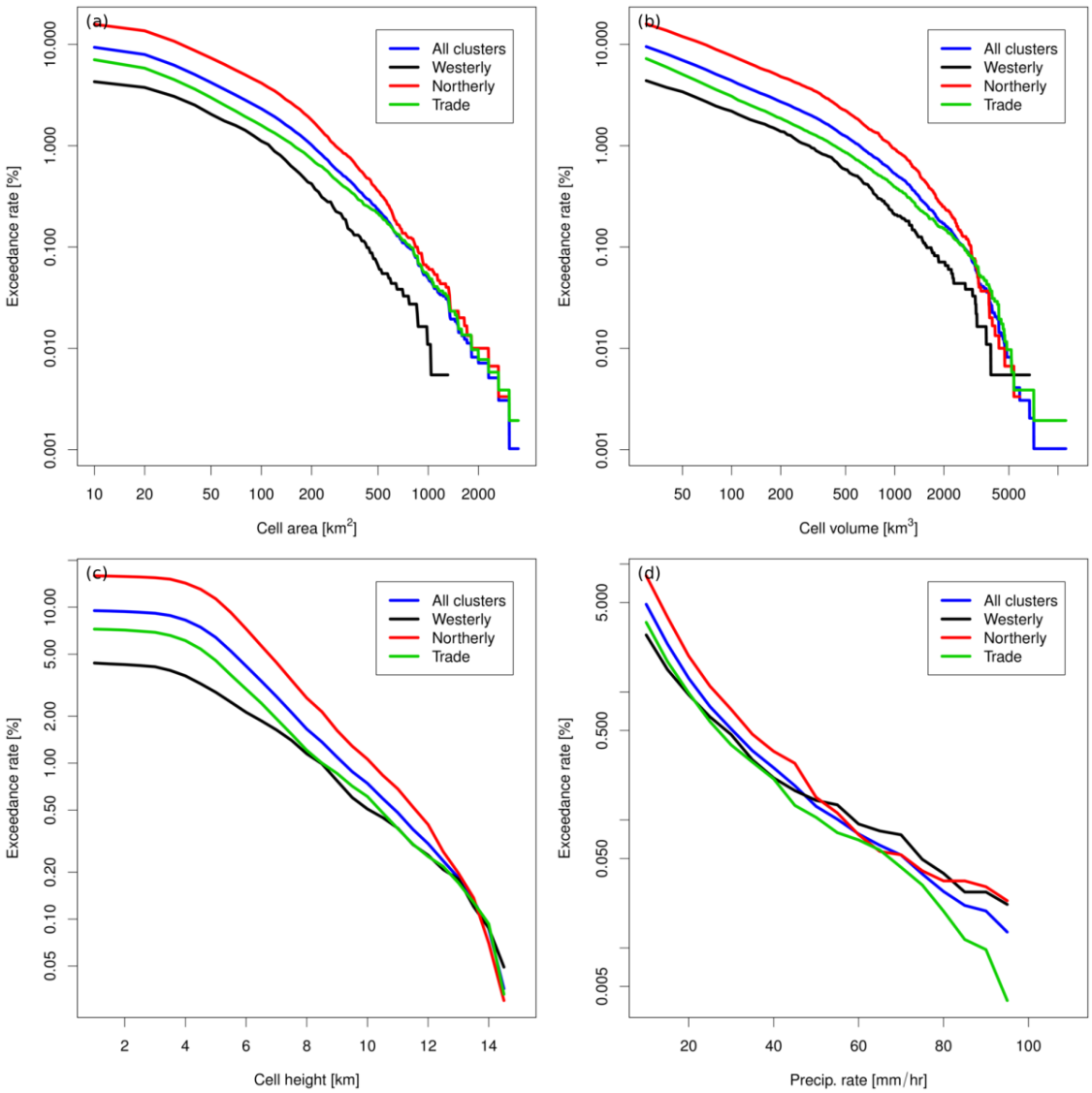

Figure 8 Exceedance rate plots of (a) cell area, (b) cell volume, (c) cell height and (d) precipitation rate. The exceedance rates have been expressed as a fraction of the total time cells were registered during a particular synoptic regime, rather than the absolute exceedance rate.

Conclusions

We have analyzed the statistical properties of precipitating storm cells in SE QLD. This was achieved via a two-stage process; first the synoptic regimes responsible for rainfall were identified, then the statistics of cells were examined considering each regime separately and combined. For the synoptic regime identification, the data were obtained from radiosonde observations of the vertical structure of the atmosphere, while cell statistics were derived from measurements of reflectivity from a ground-based S-band (10 cm wavelength) radar.

Daily upper air soundings at Brisbane airport for the period spanning January 2001 to the end of March 2008 were analysed. The soundings provided observations of wind direction, wind shear, static stability, moisture flux and total integrated water. These variables were used as input to a K-means clustering algorithm to determine three predominant synoptic regimes for the SE QLD region. The main result of the clustering analysis was:

- Three distinct synoptic regimes were identified, distinguished primarily by moisture and stability fields. The synoptic regimes were classified as: (1) a dry, stable regime with mainly westerly winds, (2) a moist, unstable regime with northerly winds and (3) a moist, unstable regime with south easterly winds. These were labeled as westerly, northerly and trade regimes, respectively. The northerly and trade regimes occurred primarily during the summer months (November–March), while the westerly regime mainly occurred during winter (April–October).

- When storms were present, the relative frequency of

occurrence, expressed as a percentage for each regime was westerly, 18%; northerly, 30% and trade, 52%.

Radar measurements from the Bureau of Meteorology's Marburg radar, situated approximately 55 km southwest of Brisbane airport, were used to provide the cell statistics. An objective method of cell identification and classification (Thunderstorm Identification, Tracking and Nowcasting —TITAN) was applied to the radar observations and various statistics of the cells analysed for the period January 2000–July 2006. The minimum volume and reflectivity threshold specified to identify a precipitating cell were 30 km^3 and 35 dBZ, respectively. The statistics examined included cell initiation location, cell area, volume, height and precipitation rate. Furthermore, the statistics were evaluated for cells in the entire period and for the separate synoptic regimes determined from the cluster analysis. The main results obtained from analysis of the radar data were:

- An enhancement in the presence and initiation location of cells was found along the mountain ranges which lie inland from Brisbane.
- Cell area, volume, height and rain rate were all well-described by truncated lognormal distributions. The same result was found when each of the synoptic regimes were considered individually, suggesting the truncated lognormal fit is insensitive to the synoptic forcing. However, the mean and standard deviation of the distributions varied among the synoptic regimes.
- Student's t-test were applied to examine if the differences in the mean and standard deviation of the cell properties among the regimes were statistically significant. The main conclusions were:
  - Trade wind regime storms are smallest by all measures of size (area, volume and height).
  - Westerly regime storms had the largest precipitation rate.
  - Westerly regime storms have generally a shorter lifetime, which was attributed to the dry upper-level moisture profile.

The results presented here have utilized single polarimetric data. The dual-polarised, dual-wavelength CP2 radar is located near Marburg radar and, despite it having been in operation for only limited periods since 2007, will enable the extension of this climatology to examine variations in the microphysics of storms among the synoptic regimes.

References

Cifelli, R., S. W. Nesbitt, S. A. Rutledge, W. A. Petersen, and S. Yuter, 2007: Radar characteristics of precipitation features in the EPIC and TEPPS regions of the east Pacific. *Mon. Wea. Rev.*, **135**, 1576–1595.

Connor, G. and M. Bonnel, 1998: Air mass and dynamic parameters affecting trade wind precipitation on the northeast Queensland tropical coast. *Inter. J. Climatol.*, **18**, 1357–1372.

Dixon, M. and G. Weiner, 1993: TITAN: Thunderstorm identification, tracking, analysis, and nowcasting — a radar based methodology. *J. Atmos. Sci. Technol.*, **10**, 785–797.

Hartigan, J. and M. Wong, 1979: A K-means clustering algorithm. *Applied Stats.*, **28**, 100–108.

Hubbert, J. C., M. Dixon, and S. M. Ellis, 2009: Weather radar ground clutter. Part II: Real-time identification and filtering. *J. Atmos. Oceanic. Technol.,* **26**, 1181–1197.

Johnson, R., T. M. Rickenbach, S. A. Rutledge, P. E. Ciesielski and W. H. Schubert, 1999: Trimodal characteristics of tropical convection. *J. Climate.*, **12**, 2397–2418.

Kumar. V. V., A. Protat, P. T. May, C. Jakob, G. Penide, S. Kumar, and L. Davies, 2013: On the effects of the large-scale environment and surface types on convective cloud characteristics over Darwin, Australia. *Mon. Wea. Rev.*, **141**, 1358–1374.

Lopez, R., 1977: The lognormal distribution and cumulus cloud populations. *Mon. Wea. Rev.*, **105**, 865–872.

May, P. T. and A. Ballinger, 2007: The statistical characteristics of convective cells in a monsoon regime (Darwin, Northern Australia). *Mon. Wea. Rev*., **135**, 82–92.

Potts, R, T. Keenan, and P. May, 2000: Radar characteristics of storms in the Sydney area. *Mon. Wea. Rev.* **128**, 3308–3319.

Potts, R., 2005: The application of TITAN for thunderstorm nowcast operations. Hydrological applications of weather and climate modeling: Extended abstracts of presentations at the seventeenth BMRC modeling workshop, 3–6 October 2005, BMRC Research Report No. 111, Bureau of Meteorology.

Conceptual Models of Severe Flash Flood Producing Rain in Two Distinct NSW Locations

Milton Speer
Climate Change Research Centre, Faculty of Science
The University of New South Wales, Sydney
milton.speer@unsw.edu.au

Introduction

The main aim of this work is to highlight the physical processes involved in conceptual models of extreme flash flood producing rain in two distinct areas of NSW, namely, the Coffs Harbour (CH) creek catchment and the Sydney metropolitan area. A conceptual model of extreme flash flood producing rain in the CH creek catchment is shown in Figure 1. Typically, there is strong southeast to northeast, moist, convergent airflow below 850 hPa in a trough/low pressure area off the coast which is enhanced by topographic lift immediately west of CH. Upper tropospheric divergence in the right exit region of a jet or ahead of an upper trough may provide enhanced lift through the mid-troposphere and reduce static stability.

For the Sydney metropolitan area, severe flash flooding from rainfall results from easterly troughs where conceptually, at the surface and in the low levels, air is close to saturation and a surface/low level trough in the easterlies provides low level convergence. The larger or synoptic scale consists of a cut-off low or trough in the mid- to upper levels which delineates northeast winds (very moist air) from northwest winds (drier, cooler subsiding air). These processes are shown schematically in Figures 2(a,b). While most of the ingredients are the same for both areas, one important difference is the strong role played by topography in anchoring rainfall over the CH creek catchment. A second difference is that for extreme Sydney metropolitan area flash flood rainfall, there is no upper tropospheric jet maximum associated with the upper trough/cut-off low.

Examples of conceptual model for Coffs Harbour creek catchment

The two most extreme short duration flash flood producing rain events in the CH creek catchment occurred on 23 November 1996 (Speer and Leslie 2000) and 31 March 2009 (Speer et al. 2011). Figure 3(a) shows the 24 h rainfall to 9 am 24 November 1996 and highlights the maximum recorded rainfall (~400 mm), concentrated over about 4 h at Sandra Close in the hills, a few kilometres to the west of the CH CBD. Figure 3(b) shows the total amount through 31 March 2009 (~350 mm in total) also concentrated over about 4h at Red Hill, a similar distance to the west of CH CBD. Figure 3(b) also highlights deflection by the nearby topography of strong southeast winds to southwest winds as a surface/low level trough reaches the coast from the east close to the same time that the heaviest rain starts. These two events had key ingredients consisting of strong, convergent and moist onshore airflow in low levels combined with a mid-tropospheric trough to the west.

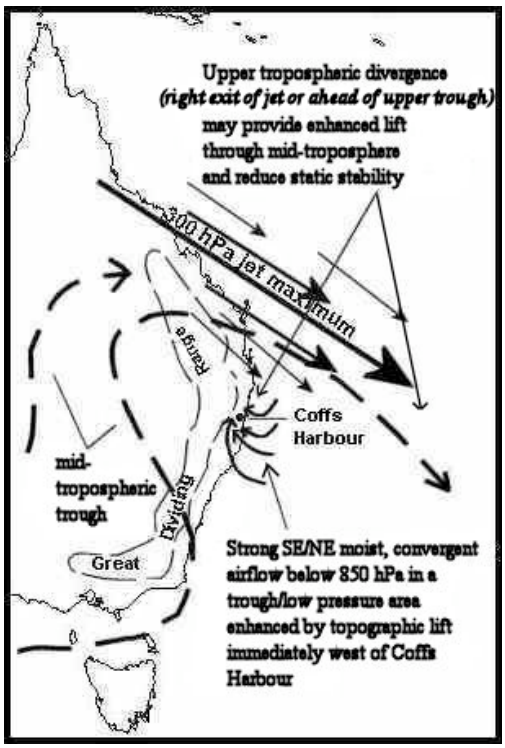

Figure 1 (adapted from Speer et al. 2011) Conceptual model of meteorological ingredients and processes involved with extreme, flash flood producing rain in the CH creek catchment of the two events of 31 March 2009 and 23 November 1996. Surface and low level airflow to about 850 hPa indicated by solid, curved arrows onto coast; mid-to upper tropospheric airflow indicated by dashed, curved arrows. Note that there is a role played by topography close to the coast near CH. Strong southeast winds are deflected to the southwest when a trough or low is close to the coast thereby enhancing confluence and convergence immediately west of CH.

The topography close to the coast provided enhanced low-level lift to the moist, convergent airflow. The low-level airflow is typically strong south easterly (60-80 km/h in the low levels)

turning lighter south westerly close to the surface and backing through the north in the mid- to upper levels. These sources of low-level lift (topography, convergence and a backing wind profile implying ascent through warm air advection), can be further enhanced by mid-tropospheric lift as a result of the divergence created by the right, exit region of an upper level jet or ahead of an upper trough. The mid-tropospheric trough provides low static stability with the potential for deep, moist convection or thunderstorms.

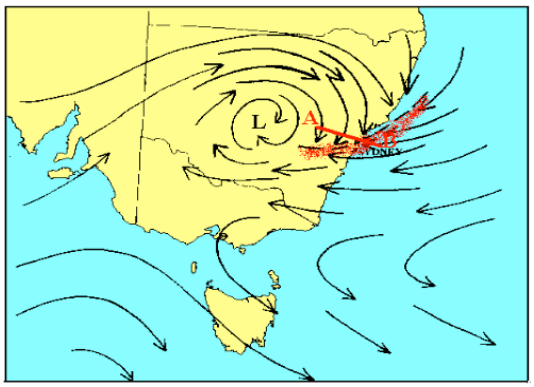

Figure 2a Plan view of mid-upper tropospheric levels showing delineation between moist NE and drier subsiding N/NW winds. Area of strongest large scale, mid-tropospheric upmotion indicated by red shading.

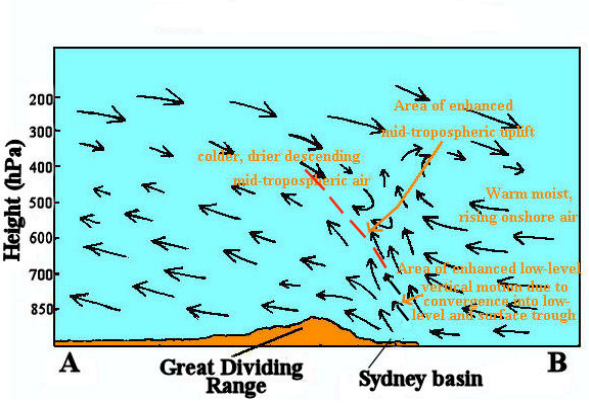

Figure 2b Cross-section along A-B in Fig.2(a). Area of enhanced mid-tropospheric uplift sloping west with height indicated by dashed red line.

For both the 31 March 2009 and 23 Nov 1996 events the key feature was the quasi-stationary nature of the rainfall over three to four hours, as convective cells successfully regenerated over the topography just to the west of CH. For example, in the 31 March 2009 event, intense rainfall is shown over the topography about 30 minutes after it started (Figure 4a) and in Figure 4(b) nearly 4 h later, the convective cells have just started to dissipate. There was another less intense event affecting the CH creek catchment on 8 November 2009 but without the added influence of a mid-tropospheric trough (not shown). In this case convective cells over the topography moved with the low to mid-tropospheric airflow without remaining quasi-stationary as occurred in the two more severe events mentioned above.

A detailed comparison of all three events is described in Speer et al. (2011). Thus it appears that anchoring of convection over topography is a critical ingredient of the most severe CH flash flood events. For this quasi-stationary process to occur, some authors have concluded that certain stability criteria need to be met. This is explained further in the Discussion section. While the conceptual model is based only on the above two events of November 1996 and March 2009, they have produced the most severe flash flooding recorded in Coffs Harbour. Other less intense rainfall events that have caused less severe flooding in CH, have occurred as a result of rainfall from larger scale synoptic systems over longer durations (see Speer and Leslie 2000).

Example of conceptual model for Sydney metropolitan area

In contrast to Coffs Harbour, there is no surface, synoptic-scale low pressure system characterizing short duration heavy rain that could be associated with severe flash flooding in the Sydney metropolitan area. The focus at the surface is a trough in the easterlies. The most severe Sydney metropolitan flash flooding occurs when the very heavy rainfall extends out to one hour and beyond. These events typically occur in a deep, moist easterly airflow focused by convergence in a surface/low level easterly trough with the maximum heavy rainfall duration extending typically from about one to six hours (Speer and Geerts 1994). Flash flooding from other synoptic types in the Sydney metropolitan area are not as severe as those of easterly troughs since rainfall rates for them, while similar, are of much shorter duration and their impacts are rarely recorded as severe (see Speer and Geerts 1994).

For flash flood rainfall resulting from easterly troughs the ingredients on the large scale consist of a trough in the mid-upper levels delineating northeast winds (very moist air) and northwest winds (drier, cooler subsiding air). The depth of atmosphere showing this demarcation varies. It might be evident on only one or two pressure levels and at other times all the way up to 300 hPa. However, the availability now of frequently updated water vapour imagery should help in showing this demarcation. Cool, subsiding northwesterly air and warm, moist rising northeasterly airflow results in large scale vertical motion based on all the 34 easterly trough events from 1957 to 1990 (Speer and Geerts 1994). At the surface and in the low levels air is close to saturation over the Sydney metropolitan area where a surface/low level trough

provides low level convergence to enhance the large scale upmotion and rainfall locally. In contrast to CH events, there is no upper level jet maximum around the upper level cut-off low/upper trough. Again, this is based all the 34 easterly trough events from 1957 to 1990 referred to above.

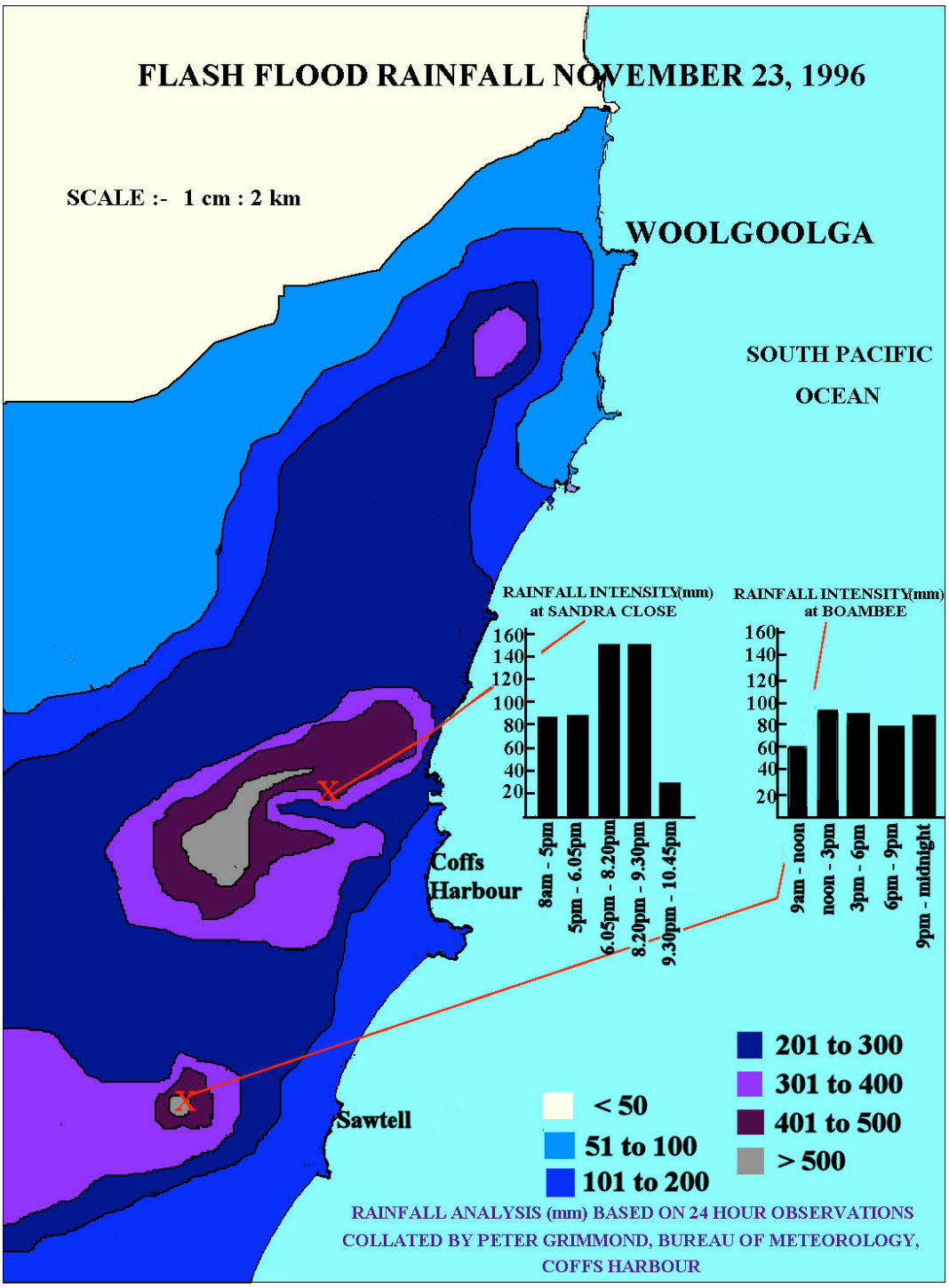

Figure 3a *(adapted from Speer & Leslie 2000) Observed 24-h rainfall (mm) to 0900 h on November 24 November 1996 based on both BoM and other sources. Also shown are the observed temporal rainfall distributions at Boambee (to the southwest of Coffs Harbour) and Sandra Close (on the west–northwest outskirts).*

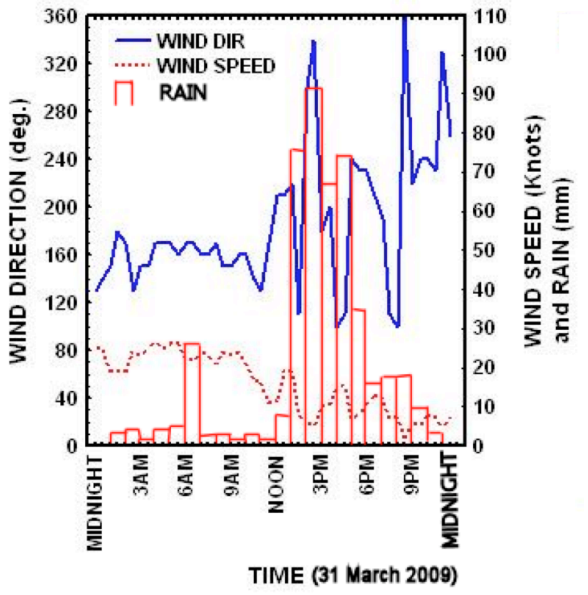

Figure 3b (from Speer et al. 2011) Red Hill hourly rainfall (mm - histogram chart), and Coffs Harbour wind speed (red, dashed line) and direction (blue, solid line) for 31 March 2009.

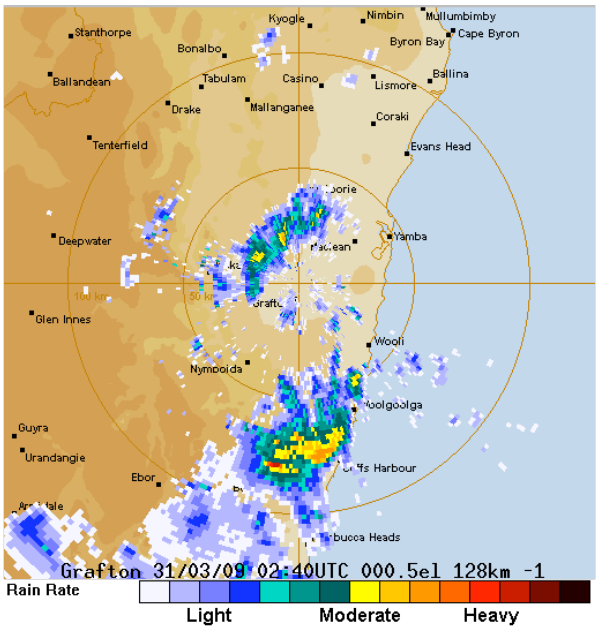

Figure 4a (from Speer et al. 2011) Radar reflectivity showing rainfall intensity at 1340 h (0240 UTC) 31 March 2009.

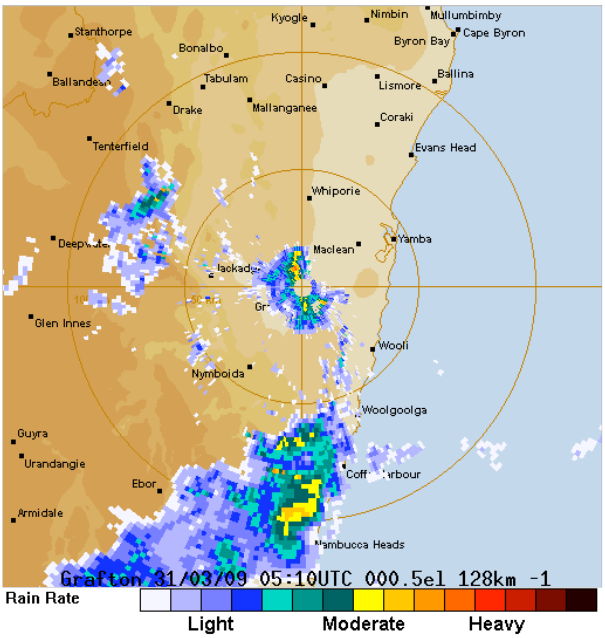

Figure 4b (from Speer et al. 2011) Radar reflectivity showing rainfall intensity at 1610 h (0510 UTC) 31 March 2009.

A typical example by way of an MSLP and upper level charts is shown in the manual analyses of Figures 5(a,b). Severe flash flooding resulted from 66 mm in 50 minutes between 1740 and 1830 h (0640/0730 UTC) at Liverpool (western metro.) on 3 April 1985 when the surface/low level trough reached the western metropolitan area.

Discussion

A key feature of both the 31 March 2009 and 23 November 1996 CH flash flood events was the quasi-stationary nature of the convective cells over the catchment topography. The processes that lead to that feature occur as a result of moist air entering the convective updraft with mass continually being removed at upper levels such that the cells are maintained and appear quasi-stationary. Chu and Lin (2000) found that the occurrence of orographic rainfall may be determined by the moist Froude number, as they termed it, which involves the wind velocity perpendicular to the mountain range, the moist static stability of the incoming airstream and the mountain height. They found that quasi-stationary convective systems over topography correspond to moderate values of the moist Froude number.

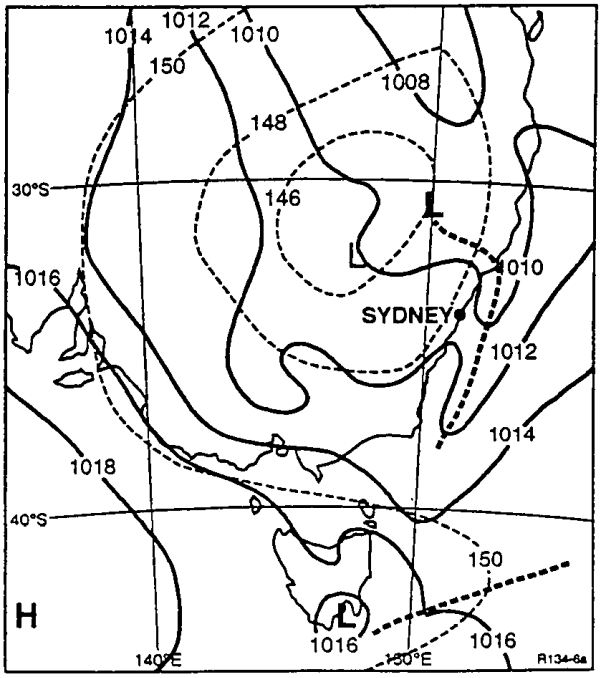

Figure 5a (from Speer & Geerts 1994) MSLP (hPa) chart (solid lines) for 1500 h (0600 UTC), 2.5 h before the flash-flood rainfall and 850 hPa (gpdm, thin dashed lines) for 0900 h (0000 UTC) 3 April 1985. The thick dashed line indicates the trough at MSLP.

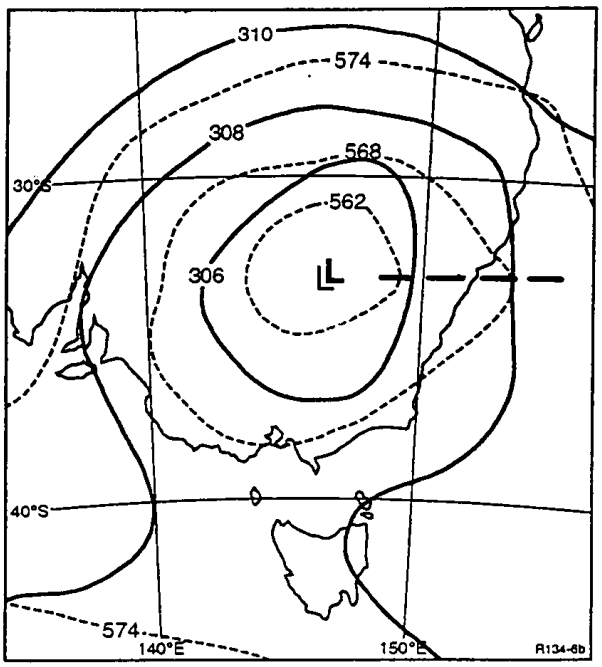

Figure 5b (from Speer & Geerts 1994) 700 hPa (gpdm, solid lines) and 500 hPa (gpdm, dashed lines) charts for 0900 h (0000 UTC) 3 April 1985. The thick dashed line indicates the trough at 500 hPa.

To determine the dynamical/thermodynamical mechanisms for this quasi-stationary convection to occur in the two CH cases, would require investigation through a series of very high resolution modelling studies (see, for example, Kirchbaum and Smith 2008).

Extreme Sydney flash floods, as mentioned in the previous section, only occur with easterly troughs when their associated rainfall duration extends towards 1 h and beyond. Other flash flood producing weather patterns tend to produce rainfall of shorter duration and are reported as severe much less often. This is most likely due to the faster movement of convective cells than those of easterly troughs with upper level steering provided by the winds associated with mobile troughs.

Very heavy short duration rainfall forecasts are a major challenge for national weather services in terms of both location and amount. This is due to the small scale of physical processes that currently are not all taken into account in numerical weather prediction models. As a result there are inadequacies in single model predictions of very heavy, short duration rainfall. There is a need, in my opinion, to move away from this deterministic based model guidance through using ensemble based forecasting, for example, by attaching probabilities and/or ranges to model output as described by Ebert (2001). It is beyond the scope of this paper but that approach was described for the one CH event 31 March 2009 (Speer et al. 2011).

Summary

Conceptual models of the processes and ingredients involved with extreme flash flood producing rainfall in the CH creek catchment and the Sydney metropolitan area have been presented. For the CH creek catchment a key feature is the quasi-stationary nature of the rainfall with the pronounced topographical anchoring of cells. The two examples presented represent the most extreme short duration rainfall that occurs in the CH creek catchment. Strong synoptic forcing is provided by a mid-tropospheric trough to the west, which reduces static stability. For the Sydney metropolitan area, severe flash flooding results from predominantly easterly troughs where, at the surface and in the low levels, air is close to saturation and a surface/low level trough in the easterlies provides low level convergence. The larger or synoptic scale consists of a trough in the mid- to upper levels, which delineates very moist northeast winds from drier, cooler subsiding northwest winds.

In contrast to severe flash flood rainfall for the CH creek catchment, for the Sydney metropolitan area strong surface synoptic forcing is not as apparent since the forced large scale ascent occurs mainly mid-level in a very moist airstream below, that is, without any strong, surface pressure system. A second difference is that there is no upper level jet maximum associated with severe Sydney flash flood events compared to the most severe flash flooding

events affecting CH. The longer duration of heavy rainfall with easterly trough events in the Sydney metropolitan area appears critical to generating extreme flash floods in that region.

Acknowledgements

This work was not supported financially by any institution or organisation. The author is grateful for the helpful reviews of two anonymous reviewers.

References

Chu, C. -M. and Lin, Y. -L. 2000. Effects of orography on the generation and propagation of mesoscale convective systems in a two-dimensional conditionally unstable flow. Journal of Atmospheric Science, 57, 3817-3837.

Ebert, E.E. 2001. Ability of a poor man's ensemble to predict the probability and disribution of precipitation. Monthly Weather Review, 29, 2461-2480.

Kirchbaum, D.J. and Smith, R.B. 2008. Temperature and moist-stability effects on midlatitude orographic precipitation, Quaterly Journal of the Royal Meteorological ociety, 134, 1183–1199.

Speer, M. and Geerts, B. 1994. A synoptic-mesoalpha scale climatology of flash floods in the Sydney metropolitan area. Australian Meteorological Magazine, 43, 87-103.

Speer, M.S. and Leslie, L.M. 2000. Flood Rain Events on the New South Wales North Coast: Comparison of Events Affecting Coffs Harbour and Case Study. International Journal of Climatology, 20, 543-563.

Speer, M.S., Phillips, J., Hanstrum, B.N. 2011. Meteorological aspects of the 31 March 2009 Coffs Harbour Flash Flood. Australian Meteorological and Oceanographic Journal, 61, 201-210.